A Radio and Ultraviolet Study of Dual Nuclei in Galaxies

A thesis

submitted for the degree of

Doctor of Philosophy

in

The Department of Physics,

Pondicherry University,

Puducherry - 605 014, India

by

Rubinur Khatun

Indian Institute of Astrophysics,

Bangalore - 560 034, India

April 2019

A Radio and Ultraviolet Study of Dual Nuclei in Galaxies

Rubinur Khatun
Indian Institute of Astrophysics

Indian Institute of Astrophysics
Bangalore - 560 034, India

Title of the thesis	:	**A Radio and Ultraviolet Study of Dual Nuclei in Galaxies**
Name of the author	:	**Rubinur Khatun**
Address	:	Indian Institute of Astrophysics II Block, Koramangala Bangalore - 560 034, India
Email	:	rubinur@iiap.res.in
Name of the supervisor	:	**Mousumi Das**
Address	:	Indian Institute of Astrophysics II Block, Koramangala Bangalore - 560 034, India
Email	:	mousumi@iiap.res.in

Declaration of Authorship

I hereby declare that the matter contained in this thesis is the result of the investigations carried out by me at the Indian Institute of Astrophysics, Bangalore, under the supervision of Mousumi Das. This work has not been submitted for the award of any other degree, diploma, associateship, fellowship, etc. of any other university or institute.

Signed: _____

Date: _____

Certificate

This is to certify that the thesis titled **'A Radio and Ultraviolet Study of Dual Nuclei in Galaxies'** submitted to the Pondicherry University by Rubinur Khatun for the award of the degree of Doctor of Philosophy, is based on the results of the investigations carried out by her under my supervision and guidance, at the Indian Institute of Astrophysics. This thesis has not been submitted for the award of any other degree, diploma, associateship, fellowship, etc. of any other university or institute.

Signed:

Date:

List of Publications

1. **Rubinur, K.**, Das, M., Kharb, P., Honey, M., 2017, "A candidate dual AGN in a double-peaked emission-line galaxy with precessing radio jets", *Monthly Notices of the Royal Astronomical Society*, 465, 4772-4782

2. **Rubinur, K.**, Das, M., Kharb, P., 2018, "Searching for dual active galactic nuclei", *Journal of Astrophysics and Astronomy*, 39, 8

3. Das, M.,**Rubinur, K.**, Kharb, P., Varghese, A., Navyasree, K., James, A., 2018 "Dual Active Galactic Nuclei in Nearby Galaxies" *Refereed proceedings of the first BINA Workshop held in ARIES, November 2016, Bulletin of Liege Royal Society of Sciences*, 87, 299-306

4. **Rubinur, K.**, Das, M., Kharb, P., 2019, "Searching for dual AGN in galaxies with double-peaked emission line spectra using radio observations", *Monthly Notices of the Royal Astronomical Society*, 448, 4933-4950

5. **Rubinur, K.**, Kharb, P.,Das, M., Rahna, P.T., Honey, M., Vaddi, S., 2019, "A Multi-wavelength Study of the Dual AGN Candidate Mrk 212", **In Preparation**

6. **Rubinur, K.**, Kharb, P.,Das, M., Rahna, P.T., 2019, "A UVIT Study of the Dual Nuclei Galaxies", **In Preparation**

Presentations

1. Poster presentation in the *Extragalactic Relativistic Jets: Cause and Effect* held at International Centre for Theoretical Sciences, Bangalore , India, during 14-17 October, 2015

2. Oral presentation in the *Astronomical Society of India meeting 2016 (ASI:2016)* held at the University of Kashmir, Srinagar, Kashmir, India, during 10-13 May 2016.

3. Oral presentation in the *SKA Pathfinders RAdio Continuum Surveys (SPARCS) meeting* held in Goa, India during 3-5 November 2016.

4. Poster presentation in the *SKA 2016 meeting* held in Goa, India during 7-11 November 2016.

5. Oral presentation in the *Wide Band Spectral and Timing Studies of Cosmic X-ray Sources* held at TIFR, Mumbai, India during 10-13 January 2017.

6. Poster presentation in the *Astronomical Society of India meeting* held at B. M. Birla Auditorium, Jaipur, India during 6-10 March 2017.

7. Oral presentation in the *Recent Trends in the Study of Compact Objects Theory and Observation (RETCO - III)* held at IIST, Thiruvananthapuram, India during 5-7th June, 2017.

8. Oral presentation in the *Astrosat Science Meet* held at ISRO, India during 26-27 September 2017.

9. Oral presentation in the *AstroSat View of AGN Central Engines Conference* held at IUCAA, Pune, India during 18-21 December 2017.

10. Oral presentation in the *Astronomical Society of India meeting* held at Osmania university, Hyderabad, India during 5-9 February, 2018

11. Oral Presentation at University of Cape Town (UCT), South African Astronomical Observatory (SAAO) and University of Western Cape (UWC) during 19-23 November, 2018.

Acknowledgements

My PhD research works could not have been carried out without the support of many people. I want to express my sincere gratitude to everyone who helped me to complete the work.

With immense love and respect, I thank Mousumi for her guidance, continuous support and motherly care throughout the Ph.D. period. I was inspired by her enthusiasm and positive approach toward the scientific problems. All advice, suggestions and freedom that you gave me enabled me to fulfill my Ph.D. I am deeply grateful to Preeti Kharb who has been always supportive, positive, friendly. Your advice and guidance on both research as well as on my career have been invaluable. I would like to thank Honey to help and guidance to carry out my research work. I extend my gratitude to Sandeep, Ankit, Jyoti and Kaushika to have healthy discussion and fun time. I acknowledge all the discussions held in the weekly meetings. Thanks to Rehana for helping me in UVIT project.

I feel obliged to the Director, the Dean and the Board of Graduate Studies (BGS) for giving me the opportunity to work in this institute and providing all the facilities required for my research work. I would also take this opportunity to thank my doctoral committee members Prof. Arun Mangalam, Prof. C. S Stalin and Prof. Bharati Mohan for their help and suggestions.

Thanks to Shankara sir for helping me in each every problem. I thank to the librarian for helping me to access necessary books and journals. I would like to thank Dr. Baba Varghese, Ashok, Fayaz, Anish and other staffs of ′Data Center′ for their help in computer and internet related issues. Many thanks to Administrative Officer, Personnel Officer, Accounts Officers and all other administrative staff for their timely help in the administrative related work. I thank the supervisors, cooks and other staff members of Bhaskara for taking care during my stay. I also

thank the staff at the Pondicherry University who has helped me regarding the administrative matters.

I acknowledge Ruta, Nissim, Ishwar, Dharam from NCRA who taught me radio astronomy in RAS school. A special thanks to Sumana di for having healthy discussion on radio astronomy. I would like to thank Dr. Russ Taylor for arranging my visit to Institute of Data Intensive astronomy (IDIA) in Cape Town, South Africa.

I express my gratitude to the course work instructors Prof. Joseph Samuel, Prof. Seetha, Prof. Prabhavati Chingangbam, Prof Tarundeep Saini, Prof. U. S. Kamath, Prof. S. P. Rajaguru, Prof. Prateek Sharma, Prof. Avinash Despande, Prof. Biswajit Paul, Prof. Shreedhar, Prof. Shiv Shethi for teaching me the basics of astrophysics. I thank Saurabh, Prasun, Varun, Janki, Karamveer and Naveen for their help during course work. I express my deepest gratitude to Prof. Ram Sagar for taking special classes at IIA and Kavalur, which played an indispensable role in understanding the basic as well as nuances of optical astronomy. I would like to thanks my Shivaji, Suparna for their excellent teaching during my M.Sc at St. Xavier's. I thank my M.Sc. project guide Sankha Subhra Nag, who helped me a lot in both academically and non-academically.

I am fortunate to have friends like Avrajit, Prasanta, Priyanka, Suman and Seniors like Ramya P, Samyaday, Sajal who are always there to stand by with me. Special thanks to Athira.

I am happy to thank my friends, seniors, colleages and junior Tanmoy, Sudip, Nancy, Susmitha, Sowmya, Supriya, Sangeetha, Avijeet, Vaibhav, Subham, Joice, Mayuresh, Prasanna S, Prasanna D, Brajesh, Kanhaiya, Asish Raj, Arun Surya, Avinash Surendran, Abha, Amit, Anirban, Avinash, Samrat, Dipanweeta, Tridib, Bhoomika, Chanyan, Sneha, Deepak, Prerna, Panini, Priya, Raghubar, Ramya,

Seerisha , Ritesh, Annu, Ambily, Anshu, Anwesh, Aritra, Ekta, Hemanth, Indrani, Joby, Jyothi, Mageshwaran, Megha, Nirmal, Partha, Pavana, Piyali, Mayuresh, Satabdwa, Sreekanth, Manoj, Varun, Deshmukh, Phanindra, Subhamay,Rakesh, Suman Saha, Tanya, Kshama, Shejeela, Meenakshi, Abha. I would like to thanks my friends Biny, Naayana, Sushma, Saili and Preetha. Thanks to Sanju, Sattar, Zibrail, Kibrail, Mikail and Tulla mama.

A special thanks to my college and school friends Barnali, Swagata, Deepa, Parpi, Jimi, Swapnali, Argha, Ananya, Soumen, Sucheta, Raghav, Ripon, Sowmadeep, Soumi, Dibyajyoti, Sangita, Eshita, Poulami di, Swapna, Nayan, Debudi, Ananya di, Neeti di, Rima, Asha, Hashi, Iti, Sonia, Mufle, Sanjib, Mister, Humaun, Rahul, Munna, Dalim, Biky, Farukh, Beauty, Reshma, Rubaya, Tanu, Pappu, Bishwa, Pandey.

At last but not the least, I would like to thank my Abba (Abdur Rahman), Amma (Saheba Khatun), Rubel, Tanve, Dibakar and other family members for their continuous support and blessings to pursue my research career.

Data usage

In this thesis work, we have used both ground and space based data obtained from various resources. I acknowledge data usage from different resources. I would like thank all the team members for making the data available.

Major radio observations are done using NRAO instrument Karl G. Jansky Very Large Telescope (VLA). We thank the staff of the VLA that made these observations possible. VLA archival data are also used in this study. The National Radio Astronomy Observatory is a facility of the National Science Foundation operated under cooperative agreement by Associated Universities, Inc.

Part of the radio observations are done using Giant Meter Radio Telescope (GMRT). We thank the staff of the GMRT that made these observations possible. GMRT is run by the National Centre for Radio Astrophysics of the Tata Institute of Fundamental Research.

This thesis uses the data from the *AstroSat* mission of the Indian Space Research Organization (ISRO), archived at the Indian Space Science Data Centre (ISSDC) which is a result of collaboration between IIA, Bengaluru, IUCAA, Pune, TIFR, Mumbai, several centres of ISRO, and CSA.

Optical observations were done at the Indian Optical Observatory (IAO) at Hanle. I especially thank the staff of IAO, Hanle, and CREST, Hosakote, that made these observations possible. The facilities at IAO and CREST are operated by the Indian Institute of Astrophysics, Bangalore.

This research has made use of the NASA/IPAC Extragalactic Database (NED), which is operated by the Jet Propulsion Laboratory, California Institute of Technology, under contract with the National Aeronautics and Space Administration.

The studies used both photometric and spectroscopic data from Data Release 12 of SDSS-III. Funding for SDSS-III has been provided by the Alfred P. Sloan Foundation, the Participating Institutions, the National Science Foundation, and the U.S. Department of Energy Office of Science.

I also acknowledge the usage of the HyperLeda database, maintained by Observatoire de Lyon (France) and the Special Astrophysical Observatory (Russia).

This research has made use of data obtained from the *Chandra* Data Archive and the Chandra Source Catalog, and software provided by the Chandra X-ray Center (CXC) in the application packages CIAO, ChIPS, and Sherpa.

Dedicated to
my Amma & Abba

Abstract

This thesis is aimed at studying dual nuclei in galaxies using radio and UV observations. Dual nuclei are formed during galaxy mergers in our Universe. Since we know that almost all nearby galaxies host a super-massive black-hole (SMBH) in their centres, galaxy mergers should produce pairs of SMBHs embedded in the dual nuclei. The term dual nuclei includes active galactic nuclei (AGN) pairs, AGN+star-forming (SF) nuclei pairs or SF+SF pairs. When the SMBHs are accreting, they form dual or binary AGN and can give rise to double-peaked emission lines in the optical spectra of the merger remnant, although the double peaks could also be due to jet-ISM interaction or rotating disks. One of the best ways to confirm the presence of dual/binary AGN in double-peaked AGN (DPAGN) is by using high resolution radio observations. In this thesis we compiled a sample of 20 DPAGN from the literature and observed them at two or more frequencies using the Karl G. Jansky Very Large Array (VLA). One of the sample sources 2MASXJ1203 shows a prominent S-shaped morphology with highly symmetric radio jets that extend out to a radius of $\sim 1.5''$ (1.74 kpc) on either side of the core which has a size of $\sim 0.1''$(116 pc). The radio jets have a helical structure resembling the precessing jets in the galaxy NGC 326 which has confirmed dual AGN. We fitted a simple model of precessing jets to 2MASXJ1203 and find that the precession timescale is around 10^5 years: this matches the source lifetime estimate via spectral aging. Also, the expected SMBH separation corresponding to this timescale is 0.02 pc. We concluded that the S-shaped radio jets are due to jet precession caused either by a binary/dual SMBH system, a single SMBH with a tilted accretion disk or a dual AGN system where a close pass of the secondary SMBH in the past has given rise to jet precession. For three other DPAGN sources in our sample, we have detected dual radio structures at separation of $\lesssim$ 10 kpc. Using the spectral index maps and optical spectra of the sources, we have confirmed that one of them is a dual AGN (DAGN), while the other two can be dual AGN or AGN+star-forming nuclei

pairs. The fifth source has a clear core-jet structure in our observations. However, the Z-shaped morphology changes direction at larger scales as traced by low frequency 1.4GHz emission; this can be due to a dual/binary AGN. The sixth source has an extended radio morphology. The next 13 sources are single cores and one source is not detected at any frequency. We find that for our dual AGN detections, the DPAGN emission lines do not originate from the dual/binary AGN. Instead, they could be due to outflows or jets. Hence, we conclude that DPAGN identified in low resolution SDSS spectra are not good indicators of dual/binary AGN. On the other hand, closely interacting galaxies or merger remnants are good candidates for detecting dual/binary AGN. We have also done ultra-violet imaging observations of a sample of 15 dual nuclei galaxies to detect the UV emission from their nuclei as well as star formation from the surrounding regions. We have used the high resolution ultra-violet imaging telescope (UVIT) which is mounted on the Astrosat satellite for these observations. We have detected emission from most of the sources which are a mixed class of AGN-AGN, AGN-SF and SF-SF nuclei. For one of the sources MRK 212 we have done followup multi-wavelength studies to confirm the nature of the nuclei. A radio, optical and X-ray study of the merging galaxy MRK 212 is presented in this thesis. With radio and UV data, we have confirmed that MRK 212 is a dual AGN (at nuclear separations of $\sim$ 6kpc) system. The deep 15 ksec UVIT image has resolved the star-forming knots in one of the nuclei (source 2) and in the tidal arms. The radio and UV emission from the two sided structure in source 2 suggests that jet is inducing star-formation. The optical spectra could not reveal the nature of the AGN; we think that is because of dust obscuration or poor sensitivity of the data. The X-ray data shows that source one has a soft spectrum while source 2 has a hard spectrum. We conclude that MRK 212 is a good example of a dual AGN with clear signatures of jet induced star formation.

List of Figures

List of Tables

Abbreviations

AGN	**A**ctive **G**alactic **N**uclei
DAGN	**D**ual **A**ctive **G**alactic **N**uclei
DPAGN	**D**ouble **P**eaked **A**ctive **G**alactic **N**uclei
SFR	**S**tar **F**ormation **R**ate
NASA	**N**ational **A**eronautics and **S**pace **A**dministration
NRAO	**N**ational **R**adio **A**stronomy **O**bservatory
VLA	**V**ery **L**arge **A**rray
HST	**H**ubble **S**pace **T**elescope
UVIT	**U**ltra-**V**iolet **I**maging **T**elescope
VLA	**V**ery **L**arge **A**rray
HCT	**H**imalayan **C**handra **T**elescope
NED	**N**ASA **E**xtragalactic **D**atabase
SDSS	**S**loan **D**igital **S**ky **S**urvey
GMRT	**G**iant **M**eter **R**adio **T**elescope
SMBH	**S**uper **M**assive **B**lack **H**ole
ISM	**I**nter-**S**tellar **M**edium
CGM	**C**ircum **G**alactic **M**edium
CCD	**C**harge **C**oupled **D**evice
$\mathbf{M}_{\odot}$	Solar **M**ass

Chapter 1

Introduction

1.1 Galaxies

Galaxies are the basic building blocks of our Universe. They are large gravitationally bound systems of stars, interstellar medium (ISM), stellar remnants and dark matter. From the Hubble morphological classification of galaxies, we know that galaxies can be of the following basic types: spiral, elliptical, lenticular and irregular (Binney & Tremaine 2008). Spiral galaxies have a spiral pinwheel appearance and most of the stars and gas are rotating in a disk along with a central bulge of older stars. The disks usually have two or more spiral arms that are associated with most of the star formation in the disks. Spiral galaxies are subdivided based on the relative size of the central bulge and tightness of their spiral pattern (Sa, Sb, and Sc). About half of all spiral galaxies have bar shaped features in their centers and they are called barred spiral galaxies (SBa, SBb, SBc). Our Milky Way (MW) is a spiral galaxy and is thought to have a bar of semi-major axis length 4.7 to 5.2 kpc (Wegg, Gerhard & Portail 2015).

On the other hand, elliptical galaxies have an ellipsoidal shape and optically appear to have very little structure. The most massive galaxies in our Universe are elliptical galaxies. They have large stellar masses but relatively little interstellar matter. There is usually no recent star formation in elliptical galaxies and if there is, it is usually due to a recent merger event with a gas rich galaxy. Ellipticals are classified from E0 to E7 based on the apparent flattening of their ellipsoidal structure (Binney & Tremaine 2008).

In the Hubble's diagram, lenticular galaxies fall in between the spiral and elliptical classes. They are denoted as SO or SB0. These galaxies have a smooth central bulge or spheroidal component surrounded by a large structure-less region of almost flat brightness (Barway et al. 2016). They have very little gas and do not show much ongoing star formation.

Irregular galaxies are small galaxies that do not have a pronounced disk structure. These galaxies may have had a strong disk structure in the past but it could have been disrupted through interactions. Alternatively they may have formed without a strong stellar disk (Binney & Tremaine 2008).

1.2 Galaxy merger and dual Nuclei

Galaxy interactions and mergers are the foremost drivers of galaxy evolution in our Universe (Barnes & Hernquist 1992). We can see signs of galaxy mergers around our own Galaxy. For example, the Andromeda galaxy or M 31 which is the largest neighboring galaxy, is approaching our Galaxy and will collide with our Galaxy in $\sim$ 3 Gyr (Binney & Tremaine 2008; Cox & Loeb 2008). Signatures of galaxy interactions were detected early on in optical images. Zwicky (1956) observed a luminosity concentration on one of the tidal tails of NGC 4038/4039 and speculated

that it might evolve into a dwarf galaxy. In 1972, Toomre & Toomre (1972) showed using numerical simulations that even with a simple model of interacting galaxies that had no self-gravity and relatively small number of particles, the morphology of a pair of interacting galaxies such as that observed in NGC 4038/4039 could be produced. Their predicted line-of-sight velocities (LOS) also agreed with the observed values. After that study, several numerical simulations have reproduced the sequence of morphological changes associated with galaxy interactions and conclude that the following processes occur during galaxy interactions: (a) the galaxy morphology changes due to tidal distortions during the various phases of mergers, (b) the close encounters of galaxies during mergers may induce enhanced star formation or starburst to occur, and (c) the sudden inflow of gas towards the centers of the individual galaxies or the merger remnant can trigger AGN activity as well as the onset of nuclear star-burst activity (Negroponte & White 1983; Sanders et al. 1988; Barnes & Hernquist 1992; Mihos & Hernquist 1994; Di Matteo, Springel & Hernquist 2005a; Springel 2005; Mayer et al. 2007; Karl et al. 2010). Toomre (1977) attempted to measure the major merger rate which turned out to be $\simeq 0.005$ Gyr^{-1}. A later estimate by Conselice (2006) found a roughly similar value. The timescale of a galaxy merger depends on the galaxy mass ratio, the orbital parameters and the relative orbital velocities of the merging galaxies (Lotz et al. 2008) and it is typically of the order of a Gyr (Mayer et al. 2007; Colpi 2014; Dotti, Merloni & Montuori 2015).

Galaxy mergers can be classified into two types depending on the mass ratio of the merging galaxies. When the mass ratio of the galaxies is $\geq 1/3$, it is a called major merger. In this case both the galaxies significantly affect each others' gravitational potential and the resulting merger remnant does not look like any of its progenitors (Binney & Tremaine 2008). On the other hand, minor mergers happen when the mass ratio of the progenitor galaxies is $< 1/3$. In minor mergers, the orbit of the smaller galaxy decays due to dynamical friction. Then the tidal force of the larger galaxy strips stars from the outskirts of the smaller galaxy and eventually the

smaller galaxy sinks towards the centre of the larger one. Such mergers are also called galactic cannibalism. Minor and major mergers lead to various peculiar galaxy morphologies such as tidal tails, rings surrounding the merger remnant, shells and other fine structures within and around the final galaxy (see review: Barnes & Hernquist 1992).

When classified according to gas content, galaxy mergers are mainly of two types: wet mergers and dry mergers (Lin et al. 2008; Amblard et al. 2014). Wet mergers occur between gas rich galaxies and lead to a large amount of star formation during the merging process and in the merger remnant. Hence, the merger remnants are usually blue in color. Dry mergers are mergers of gas poor systems. They do not lead to any significant star formation as the interacting galaxies are gas poor. Hence, they often result in the formation of red galaxies.

The merger of two galaxies naturally contains dual nuclei. These dual nuclei can be an AGN pair, an AGN and star-forming (SF) pair or a SF-SF pair. In the following sections, we first discuss AGN and then dual AGN in more detail.

1.3 Active Galactic Nuclei (AGN)

The light from normal star-forming galaxies originates from their stars and gives rise to the black-body thermal radiation which depends on the temperature of the stars. However, the nuclei of some galaxies have a much higher luminosity which cannot be explained by stellar emission. These extremely luminous nuclei are called active galactic nuclei (AGN) (figure 1.1) and their host galaxies are called active galaxies. AGN were discovered by Carl Seyfert in 1940. During photographic observation, he found that some of the spiral galaxies have extraordinary bright nuclei (Robson 1996) and their nuclear spectra have strong, broad

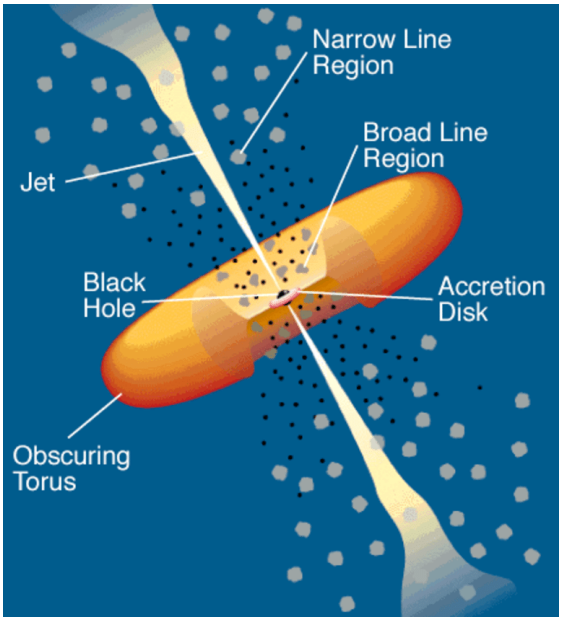

FIGURE 1.1: An AGN cartoon image. The different regions of an AGN are marked here. (Image credit:(Urry & Padovani 1995))

emission lines. The spectral energy distribution of AGN covers a very broad range of wavelength from X-ray to radio. AGN also show strong non-thermal continuum emission. Besides the high photometric luminosities of AGN over a broad range of wavelengths, they also show strong emission lines in their UV, optical and near-infrared spectra. Our current understanding of AGN indicates that they are composed of the following parts:

(i) the central supermassive black hole (SMBH): AGN emit a huge amount of energy from a small region at the center of the host galaxy which suggests that their central engine should be a massive compact object. The energy released through accretion of material onto a central SMBH is able to explain the large amount of energy arising from a very small region (Rees 1984; Peterson 1997). Observations suggest that a SMBH is present at the centre of all AGN with masses ranging from 10^6 to $10^{10} M_\odot$. The bolometric luminosity that corresponds to an outward radiation pressure that balances the inward gravitational force on infalling matter is called the Eddington luminosity. For spherical accretion, the relation between the central mass and Eddington luminosity is given by $L_{EDD} = 1.26 \times 10^{38} (M_\odot)$

ergs s^{-1} (Netzer 2006; Peterson 1997). The typical Eddington luminosity values for AGN ranges from 10^{42} to 10^{46} ergs s^{-1} for normal accretion rates onto SMBHs (Peterson 1997).

(ii) Accretion disk: It is a viscous disk of plasma around the SMBH and has a radius of R$\sim 10^{-3}$ to 10^{-2}pc. The SMBH accretes mass from the accretion disk. For an optically thick accretion disk model (e.g,, Shakura & Sunyaev 1976), the disk emits black-body thermal emission at a temperature of $\sim 2 \times 10^5$ K which peaks in the UV waveband for a SMBH with mass $M_{BH} = 10^8$ $M_\odot$ and Eddington ratio $\lambda_{EDD} \simeq 0.1$. Several factors like the magnetic field and the mass accretion rate affect the accretion disk structure. Around the accretion disk, there is an optically thin corona which is a collection of highly energetic thermal electrons. The Compton-scattering of the photons from the accretion disk produces the power law X-ray spectrum which is observed from AGN. The primary model of an accretion disk is discussed by Begelman (1985) and Blandford (1985) in their early landmark papers.

(iii) Broad line region (BLR): The BLR is situated very close to the SMBH and has a radius of R $\sim$ 0.1 - 1 pc. According to the models of AGN, the UV photons from the accretion disk excite the dense and high velocity gas clouds in this region (electron density $n_e \geq 10^8$ cm^{-3}). Hence, this region produce broad permitted emission lines with velocities of 1000 to 10000 km/sec. The BLR emits only permitted lines like H_β or H_α (Robson 1996).

(iv) Narrow line region (NLR): The narrow emission line region contains cold and low density gas ($n_e \leq 10^6$ cm^{-3}). It is situated at a distance of R $\sim$ 10 - 10^2 pc. The velocity of the narrow lines are 100 to 1000 km/sec. Along with permitted lines, the NLR emits forbidden and low probability lines such as [O III]λ5007/4959 or [NII]λ6584/6548. The lower density and lower temperature of the NLR region probably leads to smaller particle velocities and larger collisional

time scales compared to the BLR. Therefore, the ions and electrons have sufficient time to emit forbidden lines in the NLR.

(v) Dusty torus: Models predict that the BLR and NLR are surrounded by a dusty torus in the equatorial plane which obscures the central region. In general, the torus has a size of $\sim$ 1- 10 pc. The torus dust absorbs the photons from the accretion disk and becomes heated. The energy is re-emitted as thermal radiation in the infrared (IR) waveband ($\sim$ 1-1000 μm) (Pier & Krolik 1993). The torus spectrum peaks at $\lambda \approx$ 20-50 μm. The torus can polarize the AGN emission lines. The light obscuration due to the torus is determined by its size and optical depth.

(vi) Jet: Jets are collimated streams of plasma that are thought to have an orientation normal to the accretion disk. Jets are launched from the inner accretion disk around the rotating SMBH. Material is transported at relativistic speeds by jets, to distances beyond the size of host galaxy (Blandford & Znajek 1977; Blandford & Payne 1982). Observationally, it has been seen that jets may be one sided or two sided. One sided jets are quite common for radio quasars. The radiation coming from jets is non-thermal in nature. Synchrotron emission is the main process contributing to jet luminosities and is produced by accelerated relativistic electrons in the presence of a magnetic field. The magnetic field strength and the electron energy densities determine the emitted frequency of radiation. The linear sizes of radio jets can range from sub-pc to Mpc. Most jets are visible at radio wavelengths. There are very few detection in optical or X-ray (Kraft et al. 2002; Hardcastle, Birkinshaw & Worrall 2001; Worrall, Birkinshaw & Hardcastle 2003).

1.3.1 AGN classification

The photometric light from AGN divides them into two major classes which known as are Seyferts and quasars. Based on their optical spectra, Seyferts are further

sub-divided into two classes, Seyfert 1 and 2. Apart from these classes there is also another class of AGN called low-emission low ionization nuclear emission line regions (LINERS). Here we discuss each of these types of AGN and how they are distinct from one another (Urry & Padovani 1995).

Seyfert galaxies: Schmidt & Green (1983) defined Seyfert galaxies as those that have $M_B >$ -21.5+5 log h_0 where M_B is B-band magnitude and h_0 is the dimensionless Hubble parameter. They are low-luminosity sources where the AGN appear to be a star like bright object in the center of the host galaxy. The optical emission from Seyfert nuclei are found to contain strong high-ionization lines. Studies show that most Seyfert host galaxies are spiral galaxies. Seyferts are divided in two types based on their optical spectra. The spectra of Seyfert 1 nuclei have narrow emission lines as well as the permitted broad emission lines while the Seyfert 2 spectra contain only narrow emission lines. Along with emission lines, Seyferts also have weak absorption lines due to late type giant stars. One of the best ways in which to distinguish between normal AGN (Seyfert and quasars), LINERs (discussed below) and normal HII regions is by using the Baldwin, Philips and Terlevich (BPT; Baldwin, Phillips & Terlevich (1981a)) diagram. The different classes of sources are distinguished based on the flux ratios of following lines : [OIII]λ5007/Hβ, [SII]$\lambda\lambda$6716,6731/Hα and [NII]λ6583/Hα. Figure 1.2 shows an example of the BPT diagram. The narrow line spectra of type 1 Seyferts are clearly distinguishable from the spectra of the HII regions of a normal galaxy. The BPT plot also shows that the Seyfert 2 emission lines have a higher value for all the line ratios. The HII regions define a locus of lower flux ratio values that clearly do not coincide with the regions occupied by the Seyferts.

Quasar: Quasars are the most luminous AGN with nuclear magnitudes $M_B <$ -21.5+5 log h_0. Generally, quasars are so bright that the host galaxies are difficult to detect. The quasar optical spectra are similar to that of the Seyferts except that the absorption features are very weak and the narrow lines are more weaker

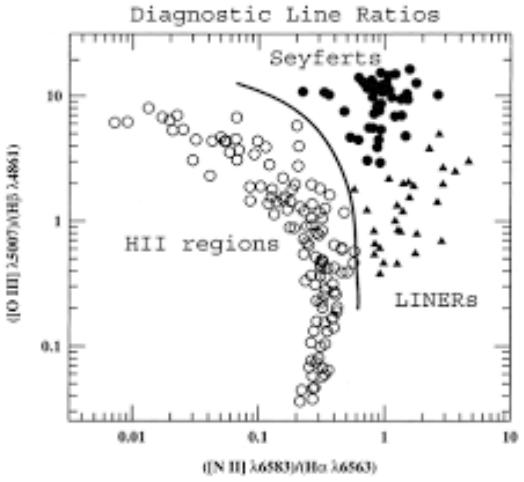

FIGURE 1.2: This is a BPT diagram. This is used to differentiate between Seyferts/Quasar, LINER and HII regions. (Image credit: (Baldwin, Phillips & Terlevich 1981a))

with respect to the broad lines.

LINER: LINERs are spectroscopically similar to Seyfert 2 nuclei. However, the low-ionization lines such as [OI] λ6300 and [NII] $\lambda\lambda$6548, 6583 are relatively strong. Most of the LINERs are present in spiral galaxies. LINERS have lower values of both [OIII]λ5007/Hα and [NII]λ6583/Hα flux ratios compared to Seyferts; this distinguishes them from the Seyferts.

Here we discuss the different types of AGN on the basis of their radio power and radio morphologies:

Radio-loud and radio quiet AGN: This is based on the ratio of the radio flux at 6 cm (5 GHz) to the optical B-band (4400Å) flux (R= f_{5GHz}/f_B (Urry & Padovani 1995)). Radio-loud AGN have R $\geq$10 (Kellermann et al. 1989) and radio-quiet AGN have R $\leq$10. However, in the broad picture of AGN, the majority ($\sim$ 85%) of the AGN are radio quiet while rest of the AGN ($\sim$ 15 %) are radio loud. In general, the host galaxies of radio-loud AGN are elliptical galaxies whereas the host galaxies of radio-quiet AGNs are spiral galaxies (Antonucci 1993).

Radio galaxies: They are a subclass of AGN that are brighter at radio wavelengths compared to visible wavelengths. They have a total radio luminosity that ranges from $\sim 10^{41}$ to 10^{46} erg s^{-1}. Synchrotron emission is the major origin of radio emission from radio galaxies. There are several radio galaxies show double sided radio structures such as the double-lobed radio source Cygnus A (Jennison & Das Gupta 1953). Radio sources have two main components : (i) Core: It is a compact region with a spectral index (α) of the order of zero. It is very difficult to resolve the central core region even with a $\sim$ milli-arcsec VLBI resolution. (ii) Radio jets: As mentioned earlier, radio jets are collimated streams of relativistic plasma which originate in the central part of the AGN. The resultant synchrotron spectrum of a jet is a power law, $S_\nu \propto \nu^{-\alpha}$ with $\alpha \geq 0.7$, S_ν is the flux density and α is the spectral index. Some jets are visible in optical and X-ray (Harris & Krawczynski 2006). (iii) Hot-spots: these are bright compact regions situated at the end of the jets. They are produced from the shocks generated by the jet and ISM interactions. The linear size of a hotspot is usually less than $\sim$1 kpc, and its typical spectral index is in the range $0.5 < \alpha < 1$. (iv) Lobes: They are extended structures, filled with plasma from the jet and extend out to the hot-spots. The radio emission is due to synchrotron emission.

Radio galaxies are divided into two groups depending on their radio morphology, Fanaroff & Riley (1974) Class I (FRI) and Class II (FRII).

• FRI are low-luminous ($P_{178} \leq 0.5 \times 10^{25}$ W Hz^{-1} sr^{-1}) radio galaxies defined by the turbulent decelerating jets with relaxed lobes. They have bright jets close to the core. Prominent hot-spots at the outer edges are absent. Most of the detected jets are FRI type. Their optical spectra show weak emission lines. There are several sub-classes of FRI sources such as head-tail, narrow angle tail and wide angle tail sources (Sebastian, Lal & Pramesh Rao 2017; Terni de Gregory et al. 2017; Mao et al. 2010).

• FRII are high-luminosity ($P_{178} \leq 0.5 \times 10^{25}$ W Hz^{-1} sr^{-1}) radio sources where the radio jet plasma appears to flow without much dissipation and produce bright hotspots towards the edges. Their optical spectra show strong emission lines.

Apart from the FRI and FRII classes, there is another set of radio loud sources, that are powerful radio emitters but have compact morphologies. Their radio emission peaks in the MHz to GHz frequency range. They are known as Compact steep-spectrum (CSS) and Gigahertz Peaked Spectrum (GPS) sources.

Blazar: Blazars are a sub-set of AGN where one side of the jet is pointing straight towards the observer. The jet has beamed synchrotron emission which is strong in the radio regime and all the way to infrared wavelengths. Blazers are radio-loud and have a flat spectral index. They are generally bright in all wavebands and show strong flux variability.

1.4 Dual AGN

In the merger driven picture of galaxy evolution, as galaxies merge, their super-massive black holes (SMBHs) lose angular momentum and spiral in towards the center of the merger remnant (Begelman, Blandford & Rees 1980a; Mayer et al. 2007; Komossa, Baker & Liu 2016). Cosmological theory (Kulier et al. 2015) and simulations (Menou, Haiman & Narayanan 2001; Roškar et al. 2015) also predict the formation of SMBH pairs and finally the formation of gravitationally bound binary SMBHs. Such mergers can trigger gas accretion onto the SMBHs, leading to the formation of active galactic nuclei (AGN) pairs or sometimes AGN-star forming nuclei pairs. At observed separations of ∼0.1 to 10 kpc, the AGN pairs are generally referred to as dual AGN (DAGN). At closer separations of a few

times 10 pc or less, the SMBHs become gravitationally bound and form SMBH binaries or a binary AGN.

There are three phases of the dual or binary SMBH evolution (Merritt & Milosavljević 2005a): (i) At first due to dynamical friction, the SMBHs sink towards the new merger remnant and form a binary. (ii) Then the binary system interacts with close-by stars and ejects them with velocities comparable to the binary orbital velocity (Khan, Just & Merritt 2011). (iii) The SMBH orbit shrinks through the emission of gravitational radiation and finally the SMBHs coalesce and emit gravitational waves that carry away the remaining angular momentum. (Berczik et al. 2006; Holley-Bockelmann & Khan 2015).

Binary/dual AGN are important to detect and study as they represent the last stages of the galaxy merging process. Mergers also affect the galaxy environment through star formation and AGN related outflows, that are collectively called feedback in the literature. Both binary and dual AGN can produce significant feedback, positive as well as negative feedback. Both processes enrich the circumgalactic medium (CGM) around the galaxy as well as affect the merging process through star-formation and AGN related outflows (Koss et al. 2012a; Blecha, Loeb & Narayan 2013; Mezcua et al. 2014). The negative feedback will drive gas out of the nuclear region (Benson et al. 2003; Di Matteo, Springel & Hernquist 2005b; Springel 2005; Hopkins et al. 2008) whereas the positive feedback will be due to shocked, cool gas falling back onto the disk (Ishibashi & Fabian 2012; Silk 2013). Finally, after the binary SMBHs coalesce the gravitational radiation emitted can be detected using pulsar timing arrays (PTA, Manchester et al. 2013) or the e-Laser Interferometer Space Antenna (eLISA Consortium et al. 2013).

According to models of galaxy mergers (Begelman, Blandford & Rees 1980a; Milosavljević & Merritt 2001; Yu 2002; Merritt 2013), DAGN should be fairly common but studies show that confirmed DAGN are still relatively rare (Figure

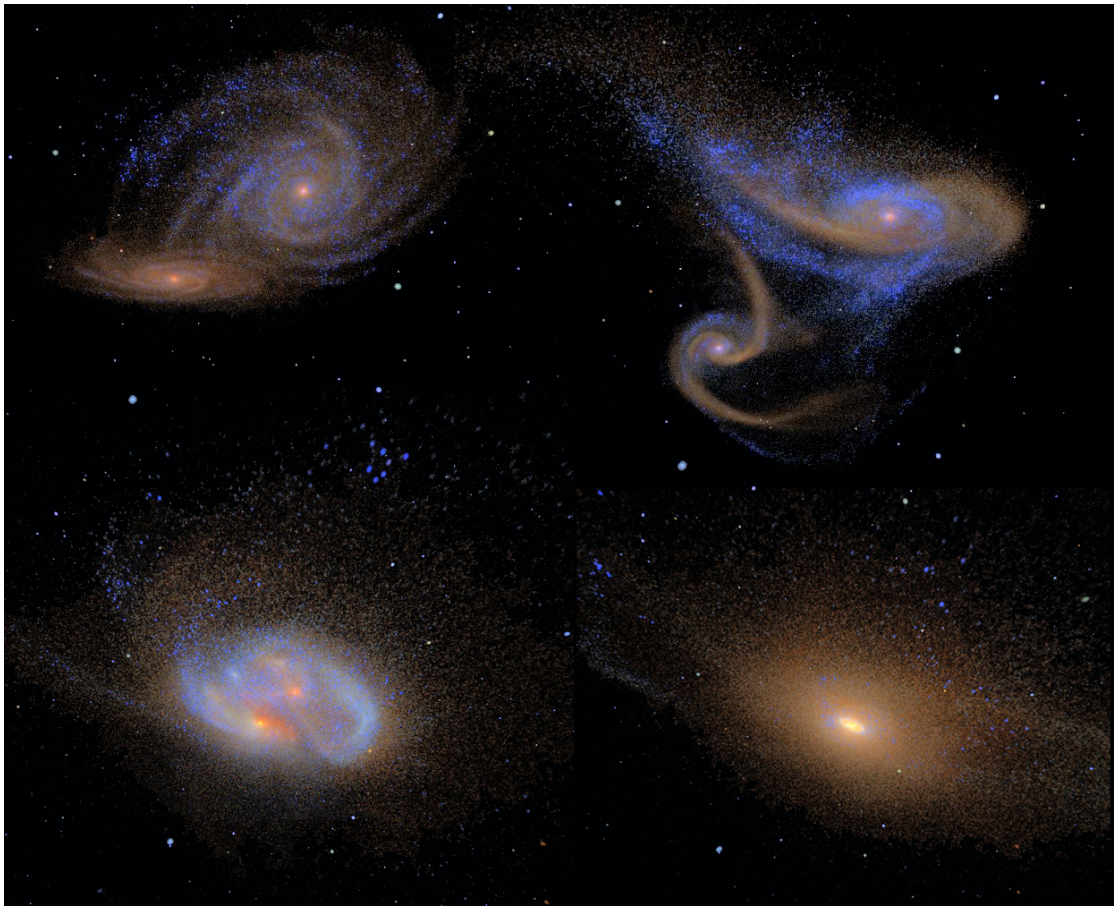

FIGURE 1.3: This image shows a time sequence mosaic of a galaxy merger. The upper left shows two Milky Way like spiral galaxies approaching each other. The upper right, during the first close-by pass, they tidally affect each other and pull out long tails of gas and stars. Lower left, then they move apart before gravity drags them back again and their centers merge. At this time, stars at larger distances from the center are sent into random orbits. Eventually, they merge (lower right) and produce an elliptical galaxy. Credits: Figure 49, Chapter 5 of "The New Universe and the Human Future" by Nancy Ellen Abrams and Joel R. Primack, 2011.

1.1) (Das et al. 2017; Rubinur, Das & Kharb 2018). One of the reasons for the low detection rate is that the resolution required to resolve the individual AGN in dual or binary systems is high, usually sub-arcsecond or milli-arcsecond scales for the nearby ($z \leq 1$) Universe (An, Mohan & Frey 2018). This resolution can be easily attained with high frequency radio interferometric observations such as with the Karl G. Jansky Very Large Array (VLA, Perley et al. 2011) where 8.4 GHz A-array observations can result in a resolution of $0.20''$ and the Very Long Baseline Array (VLBA) where 8.4 GHz observations can provide a resolution of

1 milliarcsecond (mas). The very long baseline interferometry (VLBI) technique is essential to confirm the high brightness temperature and trace the compact or extended emission from AGN on parsec and sub-parsec scales. The closest binary AGN have been detected with the VLBA (Rodriguez et al. 2006a; Kharb, Lal & Merritt 2017). However, the VLA with its higher sensitivity on sub-arcsecond scales is a better instrument to search for kpc scale dual AGN (Burke-Spolaor et al. 2014; Fu et al. 2015a; Müller-Sánchez et al. 2015a). Radio observations have the additional advantage of penetrating dust. There could be other reasons too for the rare detection - such as rapid binary coalescence timescales (Dotti, Merloni & Montuori 2015), where the SMBH mergers are accelerated by external factors such as gas accretion or interactions with passing massive objects. To understand the evolution of SMBH pairs from separations of a few kpc to final coalescence, we need a larger sample of DAGN.

The resolved DAGN are detected through high resolution imaging at radio, X-ray, optical or Near infrared (NIR) wavelengths. There is only one confirmed binary AGN which is the radio galaxy 0402+379. In this case, the Very Long Baseline Array (VLBA) has resolved the binary at 7 pc separation (Rodriguez et al. 2006b). On kpc scales, the few convincing examples are LBQS 0103-2753 (Junkkarinen et al. 2001), NGC 6240 (Komossa et al. 2003b), 3C 75 (Hudson et al. 2006), Mrk 463 (Bianchi et al. 2008), Mrk 739 (Koss et al. 2012b). More examples are in Fu et al. (2011a); Liu et al. (2013a); Comerford et al. (2015a) . In optical and NIR, the detection of two cores in imaging is not sufficient to detect two AGN because one of the cores may be a starburst nucleus or a stellar bulge. Therefore, spectroscopic observations of the cores is required along with imaging (McGurk et al. 2015).

There are a few indirect signatures of DAGN/binary AGN: (1) Periodicity in optical variability; (2) Double-peaked AGN (DPAGN) emission lines in optical nuclear spectra; (3) S- or X-shaped radio morphologies of galaxies. In the following

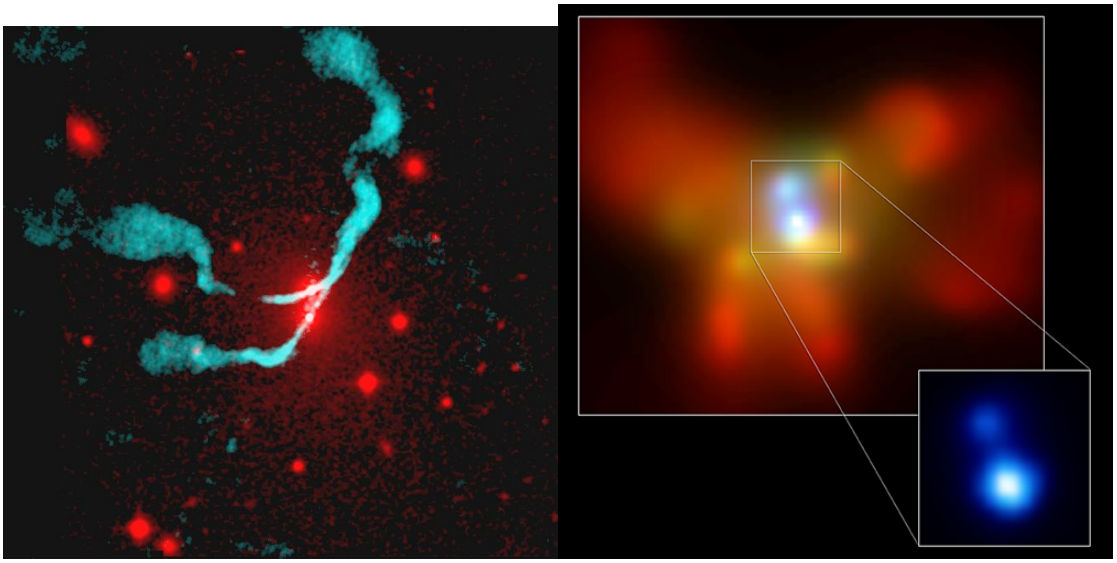

FIGURE 1.4: (left) Dual AGN galaxy 3C 75 with interacting radio jets in cyan color overlay with SDSS optical image in red (image credit: (Owen et al. 1985)). (right) The X-ray image of NGC 6240. The zoomed inset shows the two AGN (image credit: (Komossa et al. 2003a))

sub-sections we discuss the methods that are used to detect binary/dual AGN in more detail.

1.4.1 Periodicity in flux variability

The initial detection of binary/dual AGN were serendipitous and the earliest DAGN was detected due to the optical variability of the nucleus (e.g. OJ287 Sillanpaa et al. 1988; Lehto & Valtonen 1996). The quasar OJ287 has optical data available for last hundred years and shows variability in flux with a perodicity of $\sim$ 12 years (Sillanpaa et al. 1988; Valtaoja et al. 2000; Valtonen, Ciprini & Lehto 2012). It has repeated outbursts which have two peaks at separation of $\sim$ 1 yr. According to the best consistent model, there is a secondary SMBH moving in a precessing orbit about the primary SMBH and it impacts the accretion disk of the primary SMBH twice during each orbit. Recently, a close SMBH binary in the

TABLE 1.1: List of the confirmed DAGN from Rubinur, Das & Kharb (2018)

No	Name	Redshift	Projected Separation in kpc	Reference
1	Was 49	0.060979	8.3	Bothun et al. (1989)
2	LBQS 0103-2753	0.85	2.3	Junkkarinen et al. (2001)
3	NGC 326	0.047400	6.67	Murgia et al. (2001)
4	NGC 6240	0.024	0.9	Komossa et al. (2003)
5	4C +37.11	0.055	0.007	Rodriguez et al. (2006)
6	3C 75	0.023	6.4	Hudson et al. (2006)
7	MRK 463	0.050	3.8	Bianchi et al. (2008)
8	CID 42	0.359	2.46	Civano et al. (2010)
9	SDSS J150243.1+111557	0.39	7.4	Fu et al. (2011)
10	SDSS J095207.62+25527.2	0.339	4.8	McGurk et al. (2011)
11	SDSS J171544.02+600835.4	0.156300	1.9	Comerford et al. (2011)
12	SDSS J142607.71+353351.3	1.175	5.5	Barrows et al. (2012)
13	MRK 739	0.02985	3.4	Koss et al. (2012)
14	IRAS 05589+2828	0.033000	8.0	Koss et al. (2012)
15	ESO 509-IG066 NED 02	0.033223	10.5	Koss et al. (2012)
16	IRAS 03219+4031	–	10.8	Koss et al. (2012)
17	NGC 3227	0.003859	12.3	Koss et al. (2012)
18	MRK 266	0.028	6.0	Mazzarella et al. (2012)
19	SDSS J110713.22+650606.6	0.033	8.8	Teng et al. (2012)
20	2MASX J11085103+0659014	0.1816	2.1	Liu et al. (2013)
21	SDSS J114642.47+511029.6	0.1300	6.3	Liu et al. (2013)
22	2MASX J00383316+4128509	0.073	4.7	Huang et al. (2014)
23	SDSS J132323.33015941.9	0.35	0.8	Woo et al. (2014)
24	SDSS J112659.59+294442.8	0.101827	2.2	Comerford et al. (2015)
25	SDSS J220635.08+000323.1	0.046100	4.6	Fu et al. (2015)
26	SDSS J005113.92+002047.0	0.1126	3.4	Fu et al. (2015)
27	SDSS J230010.16-000531.3	0.1797	2.5	Fu et al. (2015)
28	SDSS J223222.41+001226.3	0.2210	3.2	Fu et al. (2015)
29	SDSS J115822+323102	0.1658	0.62	Müller-Sánchez et al. (2015)
30	SDSS J162345+080851	0.1992	1.55	Müller-Sánchez et al. (2015)
31	NGC 7674	0.028924	0.00035	Kharb et al. (2017a)
32	SDSS J1407+4428	0.143	8.3	Ellison et al. (2017)
33	SDSS J103631.88+022144.1	0.05040	2.8	Satyapal et al. (2017)
34	SDSS J130653.60+073518.1	0.11111	7.5	Satyapal et al. (2017)
35	SDSSJ122104.98+113752.3	0.05546	9.3	Satyapal et al. (2017)
36	SDSS 104518.03+351913.1	0.06758	9.0	Satyapal et al. (2017)

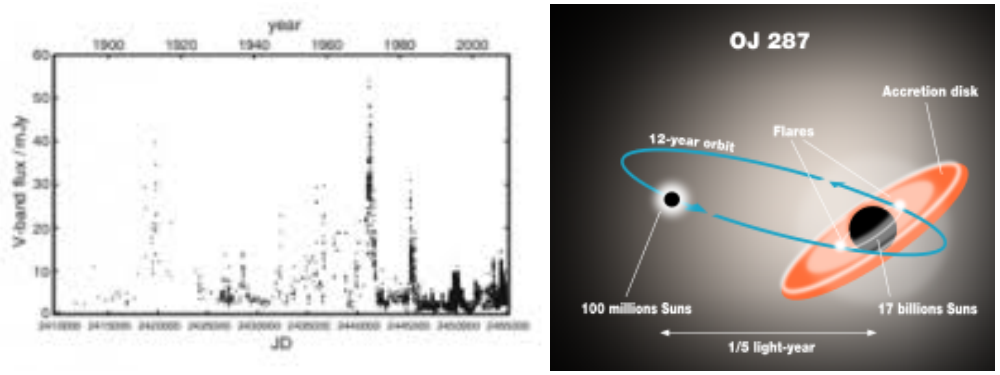

FIGURE 1.5: (left) The V-band magnitude flux versus Julian Day (JD) map of OJ 287. It has almost 100 yrs of data (Sillanpaa et al. 1988). (right) An artistic model of binary AGN which can explain the periodicity in the flux variability (image credit: Wikimedia).

quasar PG 1302-102 was also discovered from optical periodicity (Graham et al. 2015). The other example is PSO J334.2028+01.4075 (Liu et al. 2015).

1.4.2 Double-peaked Emission Lines in the Optical Spectra of AGN

Zhou et al. (2004) have suggested that double-peaked emission lines in the optical spectra of AGN (DPAGN) can be an effective way to detect DAGN with separations down to pc scales. If both the SMBH have individual NLR, then one NLR will be Doppler blue-shifted while the other one redshifted about the central wavelength due to the orbital motion of the two NLRs about the center of mass. Hence, one can imagine that during observations, one NLR is moving towards the observer and other one moving away. As a result, forbidden emission lines like [OIII]λ5007 are blue shifted by few angstroms less than λ5007 in one of the NLRs while it is red shifted in the other NLR. So instead of a single-peaked profile, the resultant spectra should have double-peaked [OIII] emission lines.

Double-peaked emission lines have been detected in AGN spectra for the last $\sim$50

years (Sargent 1972a; Veilleux 1991; Heckman et al. 2004) and were thought to be due to outflows or rotating disks. However, they can also arise from NLR gas kinematics (Gelderman & Whittle 1994; Stockton et al. 2007; Fu & Stockton 2009; Kharb et al. 2015a). High resolution Hubble Space Telescope (HST*) observations and imaging with Adaptive Optics (AO) have revealed that there are many galaxies (e.g NGC 1068) where the double-peaks in emission lines arise from the interaction of jets/outflows with the NLR (Crenshaw & Kraemer 2000). The double-peaked emission lines can also be due to nuclear rotating ionized gas disks (Müller-Sánchez et al. 2015a; Kharb et al. 2015a).

About $\sim$1% of all low redshift AGN identified by the Sloan Digital Sky Survey (SDSS) display double-peaked [O III]λ5007 emission (Smith et al. 2010). As double-peaked lines can arise from NLR kinematics, jet-ISM interaction or outflows, one needs to carry out high resolution X-ray or radio imaging to confirm the presence of DAGN. Many DAGN samples have been made from SDSS DPAGN galaxies and high resolution radio, optical, IR or in X-ray observations have been done to search for DAGN (e.g., Wang et al. 2009; Ge et al. 2012; Shen et al. 2011; Comerford et al. 2012a; Liu et al. 2010). Of all these different approaches, high resolution radio interferometry has the distinct advantage that it is not affected by dust obscuration and can give sub-parsec resolution images of the radio emission from two AGN. The disadvantage is that not all AGN have enough radio emission to be mapped at high resolutions since only 10% of galaxies are radio loud. At X-ray wavelengths, *Chandra* has the highest resolution (0.5″) which is comparable to the resolution obtained from VLA observations. But again, not all AGN show X-ray emission. Tingay & Wayth (2011a) observed 11 DPAGN using VLBI but did not find any double radio cores. They concluded that DPAGN may not be a good indicator of dual AGN. However, McGurk et al. (2015) have pointed out that the contribution of DPAGN sample in identifying DAGN is significant.

*www.spacetelescope.org/

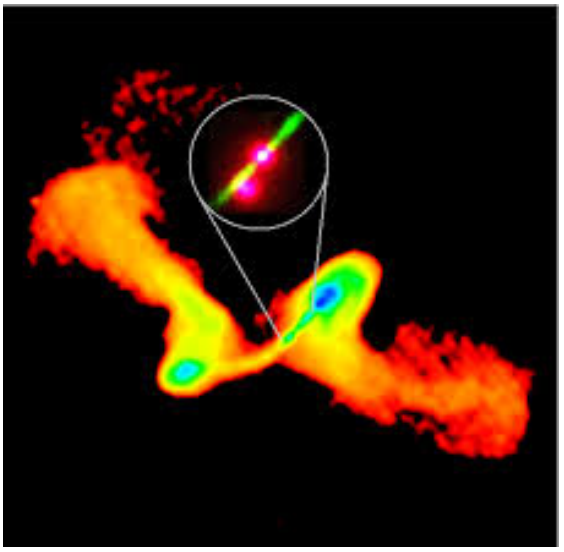

FIGURE 1.6: This is the VLA radio image of NGC 326 which has X or Z- shaped structure (Ekers et al. 1978) . The circle shows the dual AGN cores in optical HST image (Hodges-Kluck & Reynolds 2012) (image credit:wordpress.com).

Double-peaked broad emission lines have also been thought to be the tracer of binary/dual AGN (Gaskell 1983; Boroson & Lauer 2009). However, this signature can also be explained by a Keplerian accretion disk (Eracleous & Halpern 2003). Confirming the presence of binary/dual AGN in broad double-peaked emission line galaxies is difficult because of the large outflow signature in the optical spectrum. Instead, very high spectroscopic resolution and long term monitoring is required to measure the systematic changes due to orbital motion (Fu et al. 2012).

1.4.2.1 S-, Z-, X- shaped Radio source

The presence of S- or X- shaped radio jets was suggested to be connected with binary SMBHs by Begelman, Blandford & Rees (1980b). The merger of two SMBHs can give rise to an inversion symmetry in the radio jets (S, Z and X shaped sources) (Rottmann 2001; Komossa 2006; Gergely & Biermann 2009; Mezcua et al. 2011). The jet axis reorientation in the presence of a companion galaxy can be the reason for peculiar radio morphologies (Wirth, Smarr & Gallagher 1982). Also,

the interaction between the SMBHs in a DAGN can result in precessing jets that appear as X- or S-shaped radio sources (Merritt & Ekers 2002; Zier & Biermann 2002). A good example is NGC 326 (Figure 1.6) (Ekers et al. 1978) which is a Z-shaped radio source, whose radio morphology can be explained by jet precession. NGC 326 is now a confirmed dual AGN system (Murgia et al. 2001; Hodges-Kluck & Reynolds 2012). Another example is the micro-quasar SS433. This is a famous S-shaped radio source and is a binary stellar system (Blundell & Bowler 2004). In prevoius studies, Gopal-Krishna, Biermann & Wiita (2003) have suggested that Z- or S- shaped sources are SMBHs that are close to coalescence and are associated with gravitational radiation, whereas X-shaped radio sources are merged systems and have radiated away their gravitational waves. But warping of the accretion disks (Pringle 1996) or back flowing gas (Leahy & Williams 1984a) can also produce signatures of X- or S- shaped radio jets.

1.5 Star-formation and AGN feedback

Star formation plays an important role in understanding galaxy formation and evolution. The star formation rate (SFR) in galaxies can be estimated by determining the number of stars of a certain age and then using the models of the total stellar mass forming per unit time. The formation of stars in galaxies maybe triggered by various processes like galactic bars, spiral arms or supernova shocks. There are different indicators to calculate the SFR over the whole electromagnetic spectrum, starting from radio wavelengths to X-rays (Kennicutt 1998b; Bell et al. 2003; Hopkins et al. 2003; Calzetti et al. 2007). Young, hot O and B type stars are bright at UV wavelength. Hence, the UV light gives a direct evaluation of the young hot stellar population. Hα photons comes from the ionized gas by the massive stars. So, Hα can be used to detect the massive O and B stars ($> 17 M_{\odot}$)

(Kennicutt 1998b). Both Hα and UV emission are affected by dust. Therefor, dust obscuration needs to be taken into account while using these tracers.

Once the AGN activity is triggered and the SMBH reaches to a certain critical mass (Ishibashi & Fabian 2012), it gives out energy to the surrounding medium via winds, jets and radiation (Müller-Sánchez et al. 2015a). This can help in enriching the circum-galactic medium (CGM), triggering star formation beyond the AGN by shocking gas as well as suppressing gas infall and star-formation by blowing out the gas. This is collectively called AGN feedback and can prevent the mass accretion onto the SMBH. Studies indicate that it can produce the observed correlation in between the SMBH mass (M_{BH}) and the stellar velocity dispersion of bulges ($\sigma_\star$) i,e $M_{BH} - \sigma_\star$ (McConnell & Ma 2013; Greene & Ho 2006). King (2005); Ishibashi & Fabian (2012); Silk (2013) also include positive AGN feedback in their model. Ishibashi & Fabian (2012) modeled AGN feedback as a dusty shell of gas which gets pushed outwards by AGN generated winds that produce radiation pressure. They showed that the moving shells can squeeze and compress the gas which can create a fluctuations in local density and lead to star-formation. Tracing the direct evidences of AGN feedback is not an easy task. Sometimes this is explored using the disturbed gas kinematics of the NLR in AGN which show the multiple spectral components in emission lines such as O[III] (Müller-Sánchez et al. 2015a).

1.6 Motivation and Aim of Our Study

According to galaxy formation theories, binary and dual AGN should be fairly common as mergers of galaxies are seen frequently in our low redshift Universe. Simulations also provide a picture of galaxy mergers and their evolution includes the formation of binary/dual AGN. However, the detection of binary/dual AGN

is still very rare and there is no systematic sample selection method for dual/binary AGN candidates. Double-peaked emission line AGN (DPAGN) can be one signature of these systems. However, $\sim 1\%$ of the SDSS spectra shows DPAGN. Hence, a sample selection method is important before high-resolution observations. There is not much work done on the dual AGN galaxies. One reason is that it needs very high resolution multi-wavelength observations. Again the number of detections is also very low. Mergers can result in not just an AGN pair but also AGN+SF or SF+SF pairs. It is still not well understood how galaxies evolve with different types of nuclei pairs, and how they affect the star formation in the merger remnant.

Hence, we have the following objectives for this thesis:
(i) To determine a DPAGN sample using some basic theoretical concepts.
(ii) Observe the sample to detect dual/binary AGN and check that validity of the assumptions for the DPAGN sample.
(iii) Calculate the basic properties like Eddington luminosity, SMBH mass, SFR and check whether they are correlated or not.
(iii) To make a sample of the dual nuclei galaxies which may contain AGN+AGN, AGN+SF or SF+SF to do UV study to understand the star-formation as well as AGN feedback.
(ii) Do further multi-wavelength study of these galaxies to confirm the nature of the nuclei pairs.

1.7 Overview of the Thesis

- Chapter 1: We introduce the concept of galaxy mergers and the formation of dual nuclei. We discuss their evolution into dual/binary AGN. The direct and indirect signatures of dual/binary AGN are summarised. We

briefly summarise star-formation and AGN feedback processes in galaxies. We present the motivation and aim of the thesis.

- **Chapter 2:** We have discussed the instruments and observational techniques used in this thesis.

- **Chapter 3:** The sample selection method of 20 dual/binary AGN candidates from DPAGN galaxies are discussed here. We have discussed the results for one of the galaxies in our sample, J1203, which shows S-shaped radio structures.

- **Chapter 4:** Radio observation of the remaining 19 sources are discussed followed by the results and discussions.

- **Chapter 5:** We present the sample selection method of our dual nuclei galaxies for UVIT observations. Multi-wavelength study of one the sample galaxy MRK 212 is presented.

- **Chapter 6:** Summary with conclusion and future work are discussed in this chapter.

Chapter 2

Observing Facilities and Data Reduction Methods

2.1 Introduction

The aim of my research is the detection of dual/binary AGN and understanding their effect on star formation in galaxies. It is well known that a large fraction of AGN are strong radio emitters. Radio emission is not affected by the galactic dust, which makes it a good tracer of star formation. We also know that the earth's atmosphere can transmit radio waves in the wavelength range $\sim$ 1 cm to 10 m and optical waves in the range 0.36 μm to 4.50 μm. Hence, these wavelengths can be observed from earth.

However, radio waves not only have the advantage that they are not affected by dust, radio observations can yield very high resolution observations using the technique of interferometry. Radio telescopes can now achieve resolutions ranging

from sub-arcseconds to milli-arcseconds (mas). To detect dual AGN, we need higher resolution and it is most easily attained using radio observations.

Massive young stars are hot, luminous and short-lived. They emit powerful UV radiation. So, UV is very good tracer for star-formation in galaxies. However, UV light does reach earth. Hence, space observatories are needed to do UV astronomy. The OAO-2 satellite was the first UV observatory, launched in 1968. It observed many galaxies, comets and planets in UV. After this, many space telescopes observing at UV wavelengths have been launched; such as the Hubble Space Telescope (HST), Far Ultraviolet Spectroscopic Explorer (FUSE) and more recently the galaxy evolution Explorer (GALEX). These telescopes have helped us to understand the UV emission from stars and galaxies. The Ultraviolet Imaging telescope (UVIT) is a new UV telescope launched on the *Astrosat* satellite on 28 September, 2015.

In this chapter, we first discuss the radio telescopes, radio data reduction methodology. We then describe the UV telescope, UVIT. At the end of the chapter, we also discuss a few other instruments that are used during this research.

2.2 Radio Telescopes

In 1931, Karl G Jansky built an antenna to search the noise produced by radio sources in communication systems. Jansky concluded that there is some signal originating from the Milky Way. He confirmed that the radio signal from a celestial body can be detected with radio antennas on earth.

Radio telescopes have two basic components: an antenna and a receiver. Radio

antennas are typically a parabolic shaped reflector or dish. In a single dish telescope, a parabolic reflector converges the incoming signal at the focal point where feed is situated. The electric signal generated in the feed is received in the receiver and is further amplified and recorded. The telescope FAST (Five-hundred-meter Aperture Spherical radio Telescope) is today's largest single dish, filled-aperture radio telescope and the Arecibo radio telescope is the second largest one. Other important single dish telescopes are "the 64 meter radio telescope at the Parkes Observatory", "RATAN-600" and the "100 metre Green Bank Telescope (GBT)".

Diffraction limited Rayleigh criteria defines the angular resolution as $\theta \sim \lambda/D$ where λ is the observed wavelength and D is the diameter of the telescope dish. Hence, in the smaller wavelength region, say optical band, an aperture of $\sim$ few meter can provide a good resolution ($\sim$ arcsec). In the optical band (say V band, $\lambda \sim 5450$ Å), our eye, a telescope with a aperture size $\sim$6 mm can achieve a resolution of $\sim 19''$. However, at radio wavelengths one will need a gigantic dish to achieve the same resolution ($\sim$ km) and it is not possible to support such large telescope dishes.

Here, the interferomerty technique becomes important in radio astronomy. This technique combines a number of radio antennas to synthesize a large single antenna aperture. A few well known interferometers are Very Large Array (VLA), the Giant Meterwave Radio Telescope or GMRT, the Low Frequency Array (LOFAR). The interferometer MeerKat has recently started observations and is a precursor to the Square Kilometer Array (SKA). The SKA is an upcoming radio telescope which will become operational in the coming decade and will be built in South Africa and Australia. It will have 50 times higher sensitivity than any other present day radio instrument. India is one of the partners of the SKA.

FIGURE 2.1: Very Large Array (VLA). Image courtesy: NRAO

2.2.1 The Very large Array (VLA)

The Karl G. Jansky Very Large Array (VLA) (Thompson et al. 1980) is a radio interferometer which is devoted to centimeter wavelength radio astronomy. David S. Heeschen is the main driving force behind the development of the VLA and was inaugurated in 1980. It is situated Socorro, New Mexico at a latitude= 34°04′43.497″N and longitude= 107°37′03.819″W. It consists of 27 antennas, each of which has a diameter of 25 m. The observing frequency range is 74 MHz to 50 GHz. The VLA works in four different baselines at a separation of 36.0 km, 10.0 km, 3.6 km and 1 km which are called the A, B, C and D array respectively. Every four months , the configurations are changed. The maximum resolution is achieved in the A array configuration.

FIGURE 2.2: Giant Meter Radio Telescope. Image courtesy: www.skatelescope.org

2.2.2 The Giant Meterwave Radio Telescope (GMRT

The GMRT is a low-frequency interferometer (Swarup et al. 1991) located near Pune, India. It consists of 30 telescopes, each having a diameter of 45 m. The antennas are fully steerable and not movable. The longest baseline of the GMRT is $\sim$ 25 km and can achieve a maximum resolution of $\sim$2 arcsecs. Fourteen antennas are situated in central 1 km long square. These short baselines are important to observe large, extended sources. The remaining sixteen antennas are situated in three Y shaped arms along the East, West and South directions. The observable frequency range is from 150 to 1420 MHz and the frequency bands are centered at 150, 235, 325, 610 and 1420 MHz with maximum bandwidth 32 MHz. Recently, GMRT is upgraded to uGMRT with seamless frequency coverage from 50 to 1500 MHz. It has a maximum bandwidth of 400 MHz. The uGMRT bands are: (i) band-1: $50 - 80$ MHz, (ii) band-2: $120 - 250$ MHz, (iii) band-3: $250 - 500$ MHz, (iv) band-4: $550 - 850$ MHz, (v) band-5: $1050 - 1450$ MHz.

2.3 Radio data reduction

There are two packages used to reduce the radio data. These are the Astronomical Image Processing System (AIPS) and the Common Astronomy Software Application (CASA). Both packages follow almost similar method. Below we discuss in

more detail the data reduction that we did using CASA tasks.

2.3.1 CASA

CASA was developed to reduce the radio data from next generation radio telescopes like ALMA and the VLA. CASA works under an iPython interface and this permits the user to write the tasks on the terminal. The data-reduction tasks can be run manually after the input of individual parameters. Otherwise, one can add all the commands in a python script and execute on the interface. The MS (Measurement Set) format data is used in CASA. The radio data reduction process consists of flagging, calibration and image deconvolution. Self-calibration is also required in some cases to improve the image. These processes are described below.

Before starting the the flagging, the CASA task LISTOBS is used to display the information about the measurement set which includes target information, field names with serial numbers, date and time of observations, scan times, spectral window information, channel numbers and antenna positions.

2.3.2 Flagging

The first stage of data-reduction is the flagging of bad data. It is necessary to remove all kind bad data to obtain a good quality image. Bad data includes RFI (radio frequency interference), zero amplitude data, shadowed antennas. At first, we edit the data of the flux and phase calibrators which are point like sources. Usually, the visibility amplitude of any point source or unresolved source should remain constant with respect to baseline length. RFI can be an anomalous spike

in the amplitude vs baseline (i.e. uvdist) plot. Once the RFI is identified, that particular frequency range or time was flagged interactively. Zero amplitude data are searched by zooming in the plotms display and then identified the corresponding antenna and time ranges. We plotted antenna data for each spectral window (SPW) and again removed bad data. After removing the RFI and zero amplitude data, we checked for any spikes in the amplitude and removed that bad data as well. The channels at the start and at the end were checked for RFI.

2.3.3 Calibration

The observed visibility in radio interferometry, $V'_{n,m}$ for a pair of antennas n and m is correlated to the true visibility $V_{n,m}$ by this relationship:

$$V_{n,m}(u,v,f) = b_{n,m}(t)[B_n(f,t)B_m^{\star}(f,t)]g_n(t)g_m^{\star}(t)V_{n,m}(u,v,f)e^{i[\theta_n(t)-\theta_m(t)]} \quad (2.1)$$

Here u, v are referred as the spatial "baseline co-ordinates" in a frequency space, g_n and θ_n are the amplitude gains and phase complex gains of the antennas, B_n is the complex bandpass response which is a function of frequency (f) and b(t) is the baseline term, used to correct for latest updated antenna positions. Therefore, the calibration process is to solve the above equation for the amplitude, phase and bandpass gains. For this, we need to observe a source with known flux density. This calibrator is known as the flux density calibrator. 3C286, 3C48, 3C320 and 3C444 are flux density calibrators. The flux density values for these amplitude calibrators can be obtained using the task SETJY. Once the calibrations solutions are obtained, then one has to apply the calibration to bring the observed visibilities to closest possible true visibilities.

The initial phase calibration is done before bandpass to average the variation

of phase with respect to time over the bandpass. There can be prominent gain variations in-between different bandpass calibrator scans depending on frequency and configuration. This happens particularly when the scans are at significantly different elevations. Hence, using the gaincal command, the phase gains for the bandpass calibrator are derived and stored in a calibration table. The task PLOTMS is used to plot the solutions. Any extreme phase variations associated with any antennae are identified and flagged immediately. The first step of bandpass calibration is to solve the antenna based delays. The K gain type in task GAINCAL solves the relative delays in each antenna with respect to the reference antenna. Hence, it is important to choose a reference antenna which is good and then apply it for the entire scan.

The complex bandpass B_n corrections are solved using the task BANDPASS. The observed bandpass calibrator is usually a bright and flat-spectrum source at the observed frequency. Bandpass calibration is important as there can be frequency-dependent gain variations. Here, the different spectral windows may have a little different amplitude and phases for the observed bandpass calibrator as a function of frequency which should be a constant amplitude. Once the BANDPASS task is done and the solutions are saved in a table, then the complex gain calibration (g_n and θ_n) is performed using flux and phase calibrator sources.

The absolute magnitudes (g_n) are measured by observing a flux density calibrator and comparing the calculated values with known values. The gain amplitudes of the phase calibrator is also used to correct for the atmospheric differences between the target and the line of sight. Hence, the phase calibrator should be very close to the target. Then, these two set solutions of gain amplitudes are compared by using the task FLUXSCALE which determine the absolute flux density scale. This is used to determine the complex gains of the target source. The phase gains (θ_n) are determined using the phase calibrator. A phase calibrator is a point source which is observed at the phase centre. The expected amplitude is constant and

the expected phase is for the phase calibrator. Therefore, if there is any non-zero phase difference, it must be because of the antennas themselves and should take to be accounted. The calibration tables which are produced in previous tasks are then applied on the science target sources using the task APPLYCAL. Before applying the calibration, any bad data with extreme phases or amplitudes should be flagged. Once there is satisfied calibration, the science target is split to new file to do further study.

2.3.4 Deconvolution

Once the data is calibrated, the next step is to produce an image using the deconvolution algorithm. The visibilities measured by the interferometer are all discrete points which are Fourier transform of the sky in the uv- plane. This can be represented by

$$V'(u,v) = V(u,v)S(u,v) \tag{2.2}$$

Here, V′(u,v), V(u,v) are the measured and true visibilities. S(u,v) is the uv coverage which is also known as the sampling function. The inverse Fourier transform of the above equation gives

$$F^{-1}[V'(u,v)] = F^{-1}[V(u,v)] \otimes F^{-1}[S(u,v)] \tag{2.3}$$

So, the deconvolution of this equation can provide the source image i,e F^{-1}[V(u,v)]. Högbom (1974) provides the deconvolution algorithm which is one of the most popular and frequently used in recent times. This is implemented in the task CLEAN in CASA.

2.3.5 Self-calibration

The calibration before imaging can be insufficient in some cases. Especially since the ionosphere and the troposphere can be variable. Thus the gain solutions obtained during the above calibration can be unreliable. Hence, a calibration using the model image of the source itself produced by the initial clean is used to improve the complex gain of individual antennas. This is known as self-calibration. This depends on the initial model; the better the model, the better can be the updated gain. The tasks GAINCAL and APPLYCAL are used for self-calibration. Generally, the source field is split in the new MS file. Once the gain solutions are produced and applied. Then the new image and the model is formed using task CLEAN. In next cycle, the improved model is used. This process repeated until there is no improvement in SNR.

2.4 The Ultra-Violet Imaging Telescope (UVIT):

AstroSat is the first Indian space observatory dedicated to do multi-wavelength astronomy. It was launched by the Indian Space Research Organization or ISRO on 28th September, 2015. *AstroSat* consists of five payloads, where one of them is a UV camera and is called the Ultra Violet Imaging Telescope (UVIT). The other four payloads are X-ray cameras, the Scanning Sky Monitor (SSM), the X-ray imaging Telescope (SXT), the Cadmium-Zinc Telluride Imager (CZTI) and the X-ray Proportional Counters (LAXPCs).

The UVIT payload is composed of two co-aligned 35cm Ritchey-Chrtien telescopes. The spatial resolution is roughly $1.4''$ which is $\sim$ four times better than the resolution of GALEX and the field of view is $28''$. It has three detectors; the far-ultraviolet detector (FUV) operating from 1300 to 1800 Å, the near-ultraviolet

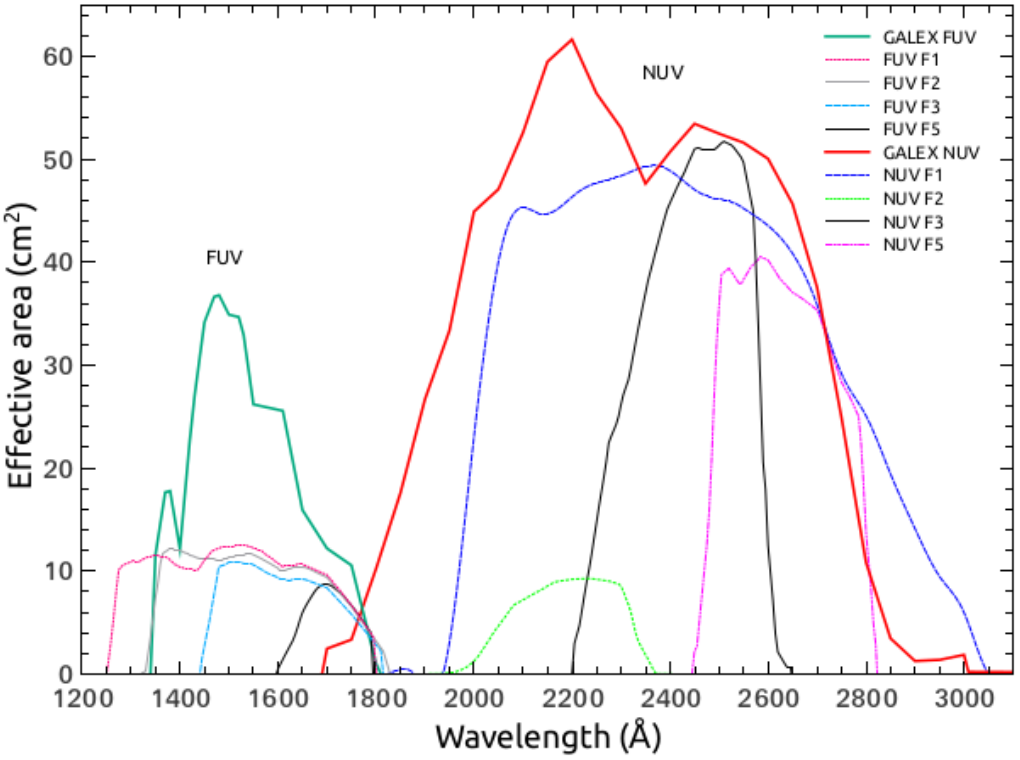

FIGURE 2.3: This image shows effective area of UVIT filters. GALEX NUV, FUV filters are also shown. Image courtesy: Rahna et al. (2018)

(NUV) detector operating between 1800 to 3000 Åand the visible (VIS) detector at 3200 - 5500 Å. These three detectors work simultaneously, each having a range of narrow and broad band filters. Kumar et al. (2012) have discussed the design of the telescopes. All three channels have five filters. The different filters are selected using a filter wheel. The visible channel is used for tracking and has a resolution of 2″.

The UV part of the electromagnetic spectrum is very important to study star formation as well as AGN activity in local galaxies, the properties of hot stars in cluster systems and the overall study of the history star-formation. The UVIT has the advantage that it not only has a wide field of view, but it also has a relatively high spatial resolution compared to the UV telescope GALEX. Hence, it is able to resolve star forming regions in nearby galaxies. This is why the UVIT was essential for studying the star formation in dual nuclei galaxies in this thesis.

We have used the JUDE pipeline to reduce the Level 1 data to Level 2 images (Murthy et al. 2016, 2017). We used Astrometry.net to do the astrometric correction for the images. The astrometry corrected images of multiple orbits are finally co-added to create the final image. L2 pipeline data is used in this work. This pipeline is developed by SAC-ISRO and UVIT team.

2.5 HCT

The 2 m Himalayan Chandra Telescope (HCT), Hanle, India is used for optical observations. It is controlled remotely from the Centre for Research and Education in Science and Technology (CREST) campus, Bangalore. The instruments mounted on it are the Himalayan Faint Object Spectrograph Camera (HFOSC), the Hanle Echelle Spectrograph (HESP) and an infrared instrument called the TIFR Near-infrared Spectrometer and Imager (TIRSPEC).

The HFOSC is an optical imager as well as a spectrograph, and it covers a wavelength range of 3500−9000 Å. It has a $10' \times 10'$ field of view (FOV). The CCD detector has a dimension of 2k×2k pixels. Each pixels has a size of 15×15 micron with plate scale $0.296''$/pixel. There are six broad band Bessell filters (U, B, V, R & I) and 6 narrow line filters available for optical imaging. There are eleven grisms with nine sets of slits that can be mounted on the instrument for optical spectrography. This provides a spectral resolution of 150 to 4500.

2.6 Archival data

2.6.1 SDSS:

The Sloan Digital Sky Survey (SDSS)* is a wide field spectroscopic and imaging survey. It has been done using a dedicated 2.5 m optical telescope located at the Apache Point Observatory, New Mexico. SDSS uses five broad-bands (*ugriz*) for imaging and the SDSS footprint covers almost one-third of the sky.The SDSS scans are done in strips and each strip consists of six scan lines.

SDSS optical imaging : The fundamental images of SDSS, called fields have sizes of 2048 $\times$ 1489 pixels corresponding to $10' \times 13'$. The image frames are identified with three sets of parameters which are run number (denoted by scan number), camera column (denoted scan-line) and field number. Observations are done in all the filters and are separated by 71.72 sec time intervals. The SDSS data is reduced using an automated pipeline.

SDSS optical spectroscopy : The SDSS Data Release 12 (DR 12) provides a set of complete spectra upto July, 2014. Many objects are observed simultaneously through SDSS spectroscopy. An aluminium plate with holes are kept at the focal plane. These individual holes are connected to the optical fibres that are plugged to the spectrograph. Until SDSS DR 8, the spectra were taken using the SDSS spectrograph with a wavelength range, 3800 to 9200 Å and had 640 fibres with a diameter of $3''$. Since then i.e. from SDSS DR 9 onwards, the new spectrograph is from the Baryon Oscillation Spectroscopic Survey (BOSS) and has a wavelength range of 2500 at 9000 Å. It has 1000 fibres per plate, each having a diameter of $2''$.

*https://www.sdss.org/

2.6.2 Chandra archival Data

The Chandra X-ray observatory (CXO)[†] is a flagship X-ray telescope, launched on 23rd July, 1999 by NASA. The spacecraft detects X-rays from extremely hot regions in the Universe. It can achieve resolution upto $\sim$ 0.5 arcsec. The high-energy X-rays photons are focused to the focal plane using the sensitive grazing incidence mirrors in the spacecraft as high-energy X-rays are able to penetrate normal mirrors. There are following instruments: High Resolution Camera or HRC, the Advanced CCD Imaging Spectrometer or ACIS, high and low energy grating spectrometers, the HETGS and LETGS. The Chandra Data Archive (CDA) allow to access Chandra data.

2.6.3 NED

The NASA Extragalactic [‡] is a multi-wavelength database which has information about extra-galactic objects. It also has an updated list of research publications. The published observations are cross matched and then added to the previous data. The information for individual sources or a set of sources can be retrieved using queries. The query requires the object name and near position. The galaxy parameters including the redshift, morphological classification, object types, survey names, redshift-independent distances, diameters, spectra, images, etc.

[†]chandra.harvard.edu
[‡]https://ned.ipac.caltech.edu/

2.7 Summary of our Observations and Data Reduction

The data and observations used in this study are summarised below:

- We have used mainly the radio and UV data to detect dual AGN and understand the star-formation in dual nuclei galaxies.
- The radio data is obtained from observations using the VLA and GMRT. Some archival VLA data is also used.
- Radio data reduction method is discussed briefly.
- The UV data is obtained from UVIT observations. We used the package JUDE to calibrate the data.
- Archival optical data (images and spectra) were obtained from the SDSS and Chandra databases.
- The optical spectrum of MRK 212 was observed using the HCT.

Chapter 3

Searching for dual AGN in galaxies using radio observation I: An S-shaped helical jet in 1203[†]

In this chapter we describe how we selected a small sample of candidate DAGN for radio observations with the VLA. We then describe the radio observations and results of one of the sample galaxy which shows an interesting S-shaped radio structure.

3.1 Sample Selection for Dual AGN candidates

We started with an initial sample of 3030 DPAGN from Ge et al. (2012), which was mainly composed of nuclei that had double peaked [O III] narrow emission

[†]Results of this chapter are published in Rubinur et al. (2017); Rubinur, Das & Kharb (2018, 2019)

lines (NEL) of separation ΔV. Out of 3030 DPAGN, only 81 are type 1 AGN and hence have broad line components. The NEL nature of the remaining sample meant that they did not have prominent AGN outflows. The double peaks in [O III] can be due to dual/binary AGN, jet- ISM interaction or rotating nuclear disks. In order to distinguish between DAGN and rotating disks, we plotted the velocity difference between the [O III] emission lines (ΔV), and the stellar bulge velocity dispersion (σ) for the 3030 NEL sample of Ge et al. (2012) (Figure 3.1). There is a significant correlation between ΔV and σ (Spearman rank correlation coefficient = 0.57, probability $< 10^{-5}$). This implies that these data lie on a line or plane, depending on whether the coefficient of proportionality is constant or not for all the sample DPAGN. The $\sigma \propto \Delta V$ correlation is likely due to a rotating disk as explained below. For gas rotating in a disk of mean radius R around a SMBH of mass M_{BH} the velocity v is given by,

$$GM_{BH}/R^2 = (v^2/R) \tag{3.1}$$

We assume that the virial theorem holds for the nuclear region so that $2T_E+V_E$=0, where T_E is the mean total kinetic energy and V_E is the mean total potential energy of stars moving with a velocity dispersion σ around a central SMBH of mass M_{BH} in a region of radius R. We can then use the relation

$$GM_{BH}/R = 2(\sigma^2/2) \tag{3.2}$$

Using these two equations, we obtain $\sigma \propto v$. If the double peaked [O III] line is due to a rotating disk, then we can assume $v = \Delta V/2$. Note that the rotating disks may be inclined at various angles with respect to our line of sight, so the general trend follows the $\sigma \propto v$ relation. Also, σ is the nuclear bulge velocity dispersion derived from the underlying absorption lines in the optical SDSS* spectrum. So, assuming that points along the $\sigma \propto v$ correlation in the σ *vs* ΔV plot represent

*www.sdss.org/dr12/

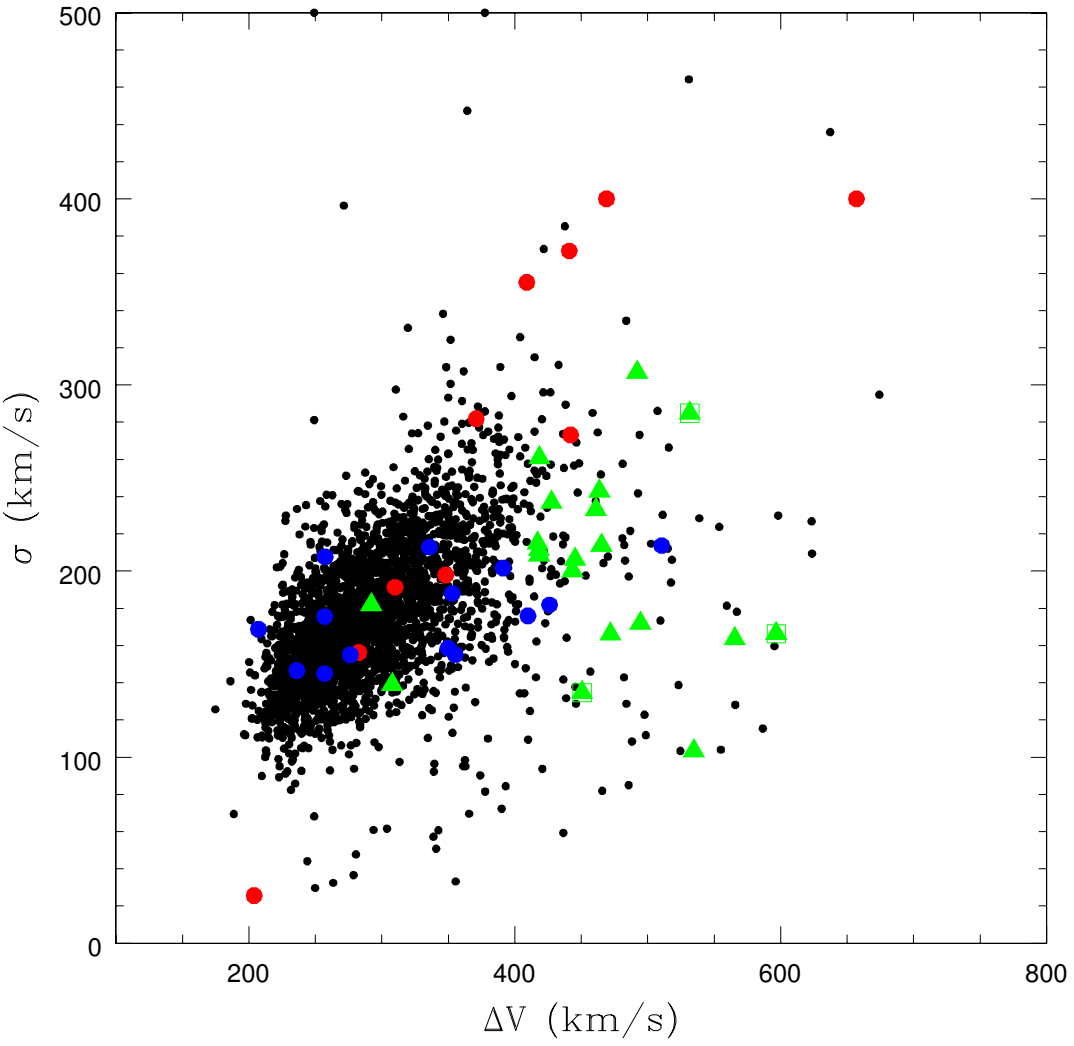

FIGURE 3.1: The $\sigma - \Delta V$ plot of 3030 double-peaked emission line galaxies from Ge et al. (2012). The velocity (ΔV) is the Doppler separation between the double-peaks in the [O III] emission lines and σ is the nuclear velocity dispersion derived from the bulge dispersion. The Ge et al. (2012) points are in black and our nineteen target sample galaxies are in green. The red points are all confirmed dual AGN which have SDSS spectra and the blue points are the DPAGN which did not yield the dual AGN in follow-up high resolution observations (see Table 3.1).

mainly rotating disks, we have tried to select DPAGN that are offset from this relation. However, this simple analysis cannot separate the jet-ISM interaction cases from the DAGN/rotating disk ones.

In Figure 3.1, we have over-plotted confirmed DAGN from the literature for which

σ *vs* ΔV data are available (red points, Figure 3.1; Table 3.1). We have also over-plotted the DPAGN that did not yield confirmed DAGN in follow-up high resolution observations (blue points, Figure 3.1; Table 3.1). We find that most of the confirmed DAGN have $\Delta V > 400$ km s^{-1} while the non-confirmed DPAGN have $\Delta V < 400$ km s^{-1}. This can be roughly explained as being due to the increase in relative velocities between the SMBHs as they come closer; hence DPAGN with larger ΔV are more likely to be dual AGN, provided the DPAGN emission is not associated with a rotating disk or jet-cloud interaction. Using the above two conditions we chose DPAGN from Figure 3.1 that (i) do not lie on the $\sigma \propto \Delta V$ correlation and (ii) have $\Delta V \geq 400$ km s^{-1}. It must be noted that these approximations are not based on any rigorous calculations and the $\sigma \propto v$ plot was constructed to increase our chance of DAGN detections. In fact, since we had first made the plot (year 2014), there have been three detections in the $\sigma \propto v$ region of Figure 3.1 (Table 3.1). However, most of the detected DAGN are still offset from this region.

In the following subsections, we discuss how the samples were selected using the σ *vs* ΔV plot. In sample 1, we restricted the sources to be low redshift disky galaxies that had ΔV ≥ 400 km s^{-1}. In sample 2 however, we included all the galaxies, irrespective of their morphologies, that are offset from the $\sigma \propto v$ correlation and had $\Delta V \geq 400$ km s^{-1}.

3.1.1 Sample 1

Most of the detected dual AGN are present in elliptical galaxies. Dual AGN in spiral or disk galaxies are relatively unknown, probably because they represent minor mergers and may be difficult to distinguish in distant galaxies. In fact there are only 3 examples of DAGN in a disk galaxy. Earlier NGC 3393 (Fabbiano et al. 2011) was the only spiral galaxy which was known to be a DAGN.

TABLE 3.1: **List of the confirmed DAGN with SDSS spectra from the literature (red points in Figure 3.1):** Column 1: SDSS name of the galaxy; Column 2: Velocity difference between the red-shifted and blue-shifted [O III] emission line (ΔV); Column 3: The velocity dispersion of the stellar population in the galaxies (σ); Column 4: References corresponding to the detection of the DAGN; **List of the DPAGN which could not yield DAGN after higher resolution observations (blue points in Figure 3.1) are added at the end. **Note:** SDSS J1023+3243 is a confirmed DAGN based on VLA data by Müller-Sánchez et al. (2015), however, subsequent VLBA imaging by Gabányi et al. (2016) failed to detect any really compact radio feature in this object.

Name	Velocity difference (km s^{-1})	Velocity Dispersion (km s^{-1})	Reference
SDSS J0952+2552	599	273	McGurk et al. (2011)
SDSS J1023+3243	371	281	Müller-Sánchez et al. (2015a)
SDSS J1108+0659	25	359	Liu et al. (2013b)
SDSS J1126+2944	191	310	Comerford et al. (2015b)
SDSS J1146+5110	156	282	Liu et al. (2013b)
SDSS J1158+3231	372	441	Müller-Sánchez et al. (2015a)
SDSS J1332+0606	355	429	Liu et al. (2010)
SDSS J1502+1115	400	647	Fu et al. (2011a)
SDSS J1623+0808	400	469	Müller-Sánchez et al. (2015a)
SDSS J1715+6008	197	358	Comerford et al. (2011)
**Non-confirmed	DPAGN	with	higher resolution obs
SDSS J0002+0045	486	221	Müller-Sánchez et al. (2015a)
SDSS J0731+4528	276	155	Müller-Sánchez et al. (2015a)
SDSS J0736+4759	257	175	Müller-Sánchez et al. (2015a)
SDSS J0802+3046	349	158	Müller-Sánchez et al. (2015a)
SDSS J0846+4258	510	213	Müller-Sánchez et al. (2015a)
SDSS J0858+1041	257	207	Müller-Sánchez et al. (2015a)
SDSS J0930+3430	257	144	Müller-Sánchez et al. (2015a)
SDSS J1023+3243	355	155	Müller-Sánchez et al. (2015a)
SDSS J1027+3059	207	168	Müller-Sánchez et al. (2015a)
SDSS J1112+2750	335	212	Müller-Sánchez et al. (2015a)
SDSS J1152+1903	236	146	Müller-Sánchez et al. (2015a)
SDSS J1556+0948	391	201	Müller-Sánchez et al. (2015a)
SDSS J1623+0808	426	181	Müller-Sánchez et al. (2015a)
SDSS J2254-0051	352	188	Müller-Sánchez et al. (2015a)
SDSS J0854+5026	320	130	Comerford et al. (2015b)
SDSS J1006+4647	229	171	Comerford et al. (2015b)
SDSS J1126+2944	309	169	Comerford et al. (2015b)
SDSS J1322+2631	397	184	Comerford et al. (2015b)
SDSS J1604+5009	368	189	Comerford et al. (2015b)
SDSS J0752+2736	281	119	Comerford et al. (2015b)
SDSS J1356+1026	413	238	Comerford et al. (2015b)
SDSS J1448+1825	251	139	Comerford et al. (2015b)
SDSS J1137+6120	237	301	Liu et al. (2017)
SDSS J1243-0058	521	311	Liu et al. (2017)
SDSS J1352+6541	373	268	Liu et al. (2017)
SDSS J23100900	327	187	Liu et al. (2017)
SDSS J2333-0049	516	90	Liu et al. (2017)
SDSS J0009-0036	332	203	Liu et al. (2017)
SDSS J0738+3156	297	258	Liu et al. (2017)
SDSS J0803+3926	391	192	Liu et al. (2017)
SDSS J0858+1041	384	222	Liu et al. (2017)
SDSS J1356+1026	413	238	Liu et al. (2017)
SDSS J1715+6008	347	131	Liu et al. (2017)

SDSS J113126.08−020459.2 (Shangguan et al. 2016) and NGC 7674 (Kharb, Lal & Merritt 2017) are two recent detection/candidate of dual/binary AGN in spiral galaxies. Hence in this study, although our broad goal was to detect DAGN in galaxies, we first focused on searching for DAGN in spirals as there are very few detections in the literature. We chose the galaxies from the $\sigma - \Delta V$ plot that were (i) offset from the $\sigma \propto v$ line; (ii) $\Delta V > 400$ km s^{-1}, (iii) z < 0.1, (iv) clear double peaked [O III] lines (since [O III] comes from the NLR and is a better dual AGN indicator), (v) showed clear disk morphologies (by visual inspection) in their SDSS images and (vi) had radio emission in the NRAO VLA Sky Survey (NVSS[†]; (Condon et al. 1998)) or Faint Images of the Radio Sky at Twenty cm (FIRST[‡]; (Becker, White & Helfand 1994)).

We rejected galaxies that had been studied in earlier radio observations (e.g., UGC 4229: Nagar et al. 1999). and finally obtained six galaxies based on the aforementioned criteria. We also chose two more disk galaxies from Fu et al. (2012) which have clear double-peaked Hα and [O III] lines, and show radio emission in NVSS as well as FIRST images. Both the galaxies have z < 0.1 but one of them has $\Delta V = 307$ km s^{-1}. These 8 galaxies were observed in the VLA cycles 15A (6 GHz) and 16A (15 GHz).

3.1.2 Sample 2

Sample 2 galaxies were also selected from Ge et al. (2012). The sample 2 sources have similar selection criteria as sample 1 sources except that there is no restriction on morphology or redshift. Our sample 2 consists of 14 DPAGN of which 2 have redshifts z <0.1, 11 sources have 0.1≤ z ≤0.5 and only one source has z >0.5. Some of the galaxies in this sample are elliptical. Two of the galaxies are

[†]https://www.cv.nrao.edu/nvss/
[‡]sundog.stsci.edu/

TABLE 3.2: **Properties of our sample galaxies:** Column 2: Name of the sample sources; Column 3,4: J2000 RA and DEC coordinates; Column 5: Redshift of the sources; Column 6: Scale at the Hubble flow distance; Column 7: Luminosity distance; Column 8: Velocity difference between the red-shifted and blue-shifted O[III] emission line (ΔV); Column 9: The velocity dispersion of the stellar population in the galaxies (σ).

Object No	Name	Right Ascension	Declination	z	**Scale** (kpc/$''$)	Distance **(Mpc)**	ΔV (km s^{-1})	σ (km s^{-1})
1	UGC 05353	09:58:40.09	+28:52:39.22	0.021	0.417	92	492.1	306.9
2	2MASX J12032061+1319316	12:03:20.7658	+13:19:31.39	0.058	1.159	245	292.1	189
3	2MASX J13245059+1758152	13:24:50.59	+17:58:15.04	0.079	1.711	381	534.6	103.3
4	2MASX J13490964+0404487	13:49:09.64	+04:04:48.87	0.085	1.582	351	445.3	206.3
5	2MASX J16170895+2226279	16:17:08.95	+22:26:27.00	0.065	1.313	284	450.6	134.7
6	2MASX J16441390+2528286	16:44:13.90	+25:28:28.60	0.055	1.113	238	463.7	243.1
7	2MASX J23044283-0933454	23:04:42.83	-09:33:45.40	0.032	0.645	130	307.8	139.0
8	SDSS J233604.04+000447.1	23:36:04.04	+00:04:47.10	0.076	1.532	327	472.0	166.2
9	2MASX J09120164+5320369	09:12:01.68	+53:20:36.90	0.101	2.033	454	418.4	208.7
10	SDSS J100602.13+071130.9	10:06:02.13	+07:11:30.90	0.121	2.407	550	596.7	166.4
11	SDSS J110215.68+290725.2	11:02:15.68	+29:07:25.24	0.106	2.111	476	417.2	215.2
12	SDSS J132318.81+030807.1	13:23:18.82	+03:08:07.13	0.269	5.353	1327	465.2	213.7
13	SDSS J135558.08+001530.6	13:55:58.09	+00:15:30.60	0.134	2.668	612	531.6	284.9
14	2MASX J14131625+2119374	14:13:16.25	+21:19:37.47	0.172	3.444	806	427.7	237.1
15	2MASX J14203147+4008166	14:20:31.51	+40:08:15.97	0.210	4.207	1005	461.0	233.0
16	2MASX J14454130+3341080	14:45:41.30	+33:41:07.86	0.131	2.615	595	494.5	172.0
17	2MASX J15001769+1051100	15:00:17.73	+10:51:09.81	0.170	3.404	795	443.5	200.0
18	B31459+399NED01	15:01:02.57	+39:42:00.07	0.355	7.077	1828	565.5	163.7
19	2MASX J15042218+4741116	15:04:22.21	+47:41:12.06	0.093	1.868	413	418.5	260.9
20	SDSS J160027.78+083743.0	16:00:27.78	+08:37:43.00	0.226	4.518	1089	418.2	211.6

merger systems, where the morphologies are not clear. Two of the objects had right ascension coordinates that could not fit within the observational schedule and hence could not be observed. We finally observed a total of 12 sources (Table 3.2) in the VLA cycle 16B (at 8.5 and 11.5 GHz).

In this chapter, we investigate the peculiar radio morphology of the source 2MASX J12032061+1319316 (J1203) Rubinur et al. (2017) from sample 1. It shows an interesting kpc scale S- shaped core-jet structure. Such S-shaped radio jets can arise from jet precession in the presence of second SMBH. We have discussed the radio morpholog and spectral index map of this source. Then we fitted the (Hjellming

& Johnston 1981) model on the S-shaped structure. Finally, the possible origin of the jet precession are discussed. The remaining 7 galaxies from sample 1 and 12 galaxies from sample 2 are discussed in chapter 4.

3.2 The radio source 2MASX J12032061+1319316 (J2MASXJ1203)

Our preliminary data analysis at 6 GHz revealed that the nuclear emission of 2MASXJ1203 had an interesting S-shaped morphology and two hotspots. On analysing additional archival data at higher frequencies (8.5 and 11.5 GHz), we clearly resolved the compact core and found S-shaped radio jets. 2MASXJ1203 has been studied earlier at optical wavelengths in DPAGN surveys (Fu et al. 2012; Ge et al. 2012; Wang et al. 2009). The galaxy has a moderate redshift (z = 0.058), a compact core and extended disk (Table 3.3). The underlying galaxy maybe an S0 or spiral galaxy (Fathi et al. 2010) but its HyperLeda [§] classification has a large error (Makarov et al. 2014). In Section 3.2.3.2, we discuss our own 2D galaxy image decomposition using GALFIT. The optical spectrum shows double peaks in [O III], [O II], Hα, [N II] emission lines (Figure 3.2). The underlying stellar velocity dispersion is 189.9 km sec^{-1} (see Section 3.2.2). The nucleus shows radio emission in both the NRAO VLA Sky Survey (NVSS)[†] and Faint Images of the Radio Sky at Twenty-cm (FIRST)[‡] images at 1.4 GHz. The NVSS peak flux density is 0.108 Jy at 1.4 GHz. The nucleus has a Seyfert 2 classification and is radio-loud with a radio loudness parameter of 156 (Fu et al. 2012). The Rossi All Sky Survey (RASS) [§] covered the source region during one of its survey scans for about 440 s; but 2MASXJ1203 was not detected in the RASS faint source catalogue

[§]http://leda.univ-lyon1.fr/
[†]http://www.cv.nrao.edu/nvss/
[‡]http://www.cv.nrao.edu/first/
[§]https://heasarc.gsfc.nasa.gov/docs/xte/XTE.html

TABLE 3.3: Sample Galaxy J12032061+1319316:

Parameters	Values	Reference
Galaxy name	2MASX J12032061+1319316	NED
RA	12:03:20.7658	NED
DEC	+13:19:31.39	NED
Galaxy Type	S0	(Fathi et al. 2010). HyperLeda
Redshift	0.058423	NED
Luminosity Distance	245.4 ± 17.2 Mpc	NED
Radio Loudness Parameter	156	(Fu et al. 2012)
1.4 GHz Peak Flux Density	0.103 Jy/beam	NVSS (beam = 45″)
Optical Absolute Mag (z band)	-22.07 ± 0.50	SDSS DR9
Velocity Dispersion	189.9 km s^{-1}	pPxf using SDSS DR9 spectra

which has a flux limit of $F_x \leq 1 \times 10^{-13}$ erg cm^{-2} s^{-1}. The galaxy was observed in the GALEX Survey for 107s in the near ultraviolet (NUV) band; the NUV flux density is 9.60×10^{-6} Jy. The NASA/IPAC Extragalactic Database (NED)[¶] shows that there are two galaxies within the velocity range from 17015 km s^{-1} to 18015 km s^{-1}. However, the galaxy does not show any signatures of interaction such as tidal tails in its optical image and hence may not be undergoing a major merger. A minor merger, however, cannot be ruled out.

3.2.1 Observation and Archival Data

We observed 2MASXJ1203 on 20 July 2015 (Project ID: 15A-068) (Table 3.4) in the C-band at 6 GHz using the A configuration (resolution 0.33″) for 5 minutes along with the flux density calibrator, J0542+4951 for 10 minutes. The nearest phase calibrator, J1239+0730 was observed for 50 seconds. The observations were done with a 1792 MHz wide baseband centered at 5.935 GHz with fourteen spectral windows, each of which have 64 channels with frequency resolution of 2 MHz. We

[¶]http://ned.ipac.caltech.edu/

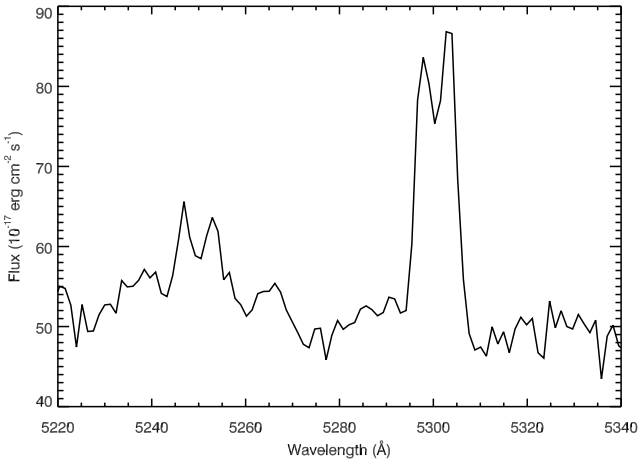

FIGURE 3.2: The double peaked emission lines in the SDSS optical spectrum from the nuclear region of SDSSJ120320.7+131931. The lines are [OIII, λ5007 Å] and [OIII λ4959 Å] of the [O III] doublet. There is no broadening which suggests the absence of AGN outflows.

TABLE 3.4: Observation Details

Frequency	Observing Date	ID	Reference
6 GHz	20 July, 2015	VLA/15A-068	Our Data
8.5 GHz	14 March, 2014	VLA/13B-020	Archival Data
11.5 GHz	14 March, 2014	VLA/13B-020	Archival Data
15 GHz	29 May, 2016	VLA/16A-144	Our Data

also reduced the 8.5 GHz and 11.5 GHz archival data of 2MASXJ1203 (Project ID:VLA/13B-020). The observations were carried out in the X-band, with two frequency centers at 8.5 GHz and 11.5 GHz in the A configuration with eight spectral windows. We have carried out VLA 15 GHz observations of 2MASXJ1203 in the B array configuration (resolution 0.42″) (Project ID: 16A-144) on 29th May 2016. The source 2MASX1203 was observed for 16 minutes along with the flux density calibrator 3C 286 and the phase calibrator J1224+2122. The flux density calibrator 3C 286 was observed for 11 minutes and J1224+2122 was observed for 8 minutes.

3.2.2 Data Reduction

We have used the Common Astronomy Software Applications (CASA) (McMullin et al. 2007) and Astronomical Image Processing System (AIPS) packages for data reduction. The bad data was flagged to obtain good solutions. PLOTMS is used to identify the bad data and the task FLAGDATA to flag it. We have used the task GAINCAL to obtain the calibration solutions and applied it using the task APPLYCAL. After a satisfactory calibration we imaged the source using the task CLEAN. We made both natural and uniform weighted images using the Briggs robust parameters 0.5 and -0.5 respectively. The natural weighted images recovered most of the flux density but gave a poor spatial resolution; hence we used it mainly to derive the total extent of the radio jets. The uniform weighted maps gave a better spatial resolution that enabled us to distinguish between the core and the jets. For the 6, 8.5 and 15 GHz maps, we obtained good images after one round of phase self-calibration. For 11.5 GHz, we obtained a better image after two runs of phase self-calibration. We have used IMFIT and IMSTAT tasks to get the core size, peak flux density and noise (Table 3.5).

We have used the 8.5 GHz and 11.5 GHz images to generate the spectral index map (Figure 3.7). We made a new 11.5 GHz image with same restoring beam as the 8.5 GHz map by constraining the beam size in the task CLEAN. We used the task COMB in AIPS and task IMMATH in CASA to obtain the spectral index map and spectral index error map. The spectral index image was created after blanking the flux density values below 3σ, at both frequencies. We followed a similar procedure to make spectral index map with the 6 GHz and 15 GHz images (Figure 3.7).

We have used the SDSS DR 12 I-band image for determining the morphology of 2MASXJ1203 using GALFIT (Peng et al. 2010, 2002). The SDSS images were first converted back into count units using an IDL program. We created the Point

Spread Function (PSF) and masked the nearby bright sources in the frame to obtain an accurate fitting. The residual images are produced in GALFIT by subtracting the image made by the convolution of the model with PSF from the original galactic image.

We have used the pPXF (Penalized Pixel-Fitting stellar kinematics extraction) code (Cappellari & Emsellem 2004) to calculate the velocity dispersion of the underlying stellar population in the nuclear region, which uses the Gauss-Hermite parametrization technique (Gerhard 1993). We have used the SDSS DR12 spectrum for this task (Figure 3.2). The code first masks the emission lines in the spectrum and then fits a model to the absorption lines using a combination of single stellar population templates of different ages. It starts with initial guess values of the galaxy systemic velocity and stellar velocity dispersion (σ). The best fit model gives the stellar velocity dispersion value $\sigma = 189.9$ km s^{-1}.

3.2.3 Results

3.2.3.1 Radio Images

The radio images at 6, 8.5, 11.5 and 15 GHz are shown in Figures 3.3, 3.4, 3.5. The uniform weighted images gave the optimum spatial resolution and flux densities but we used naturally weighted map at 8.5 GHz to examine the S-shaped structure (Figure 3.4). The 6 and 15 GHz radio images have two distinct radio lobes and hot spots on either side of the nucleus (Figure 3.3 and 3.4). The hot spot south of the nucleus has a larger flux density of 11.9 mJy (see Table 3.5) suggesting that it is the closer jet and is curved towards the east. The increased brightness could be indicative of Doppler boosting. The 8.5 GHz (Figure 3.3) and 11.5 GHz (Figure 3.5) images reveal a core lying between the radio lobes. The core-jet

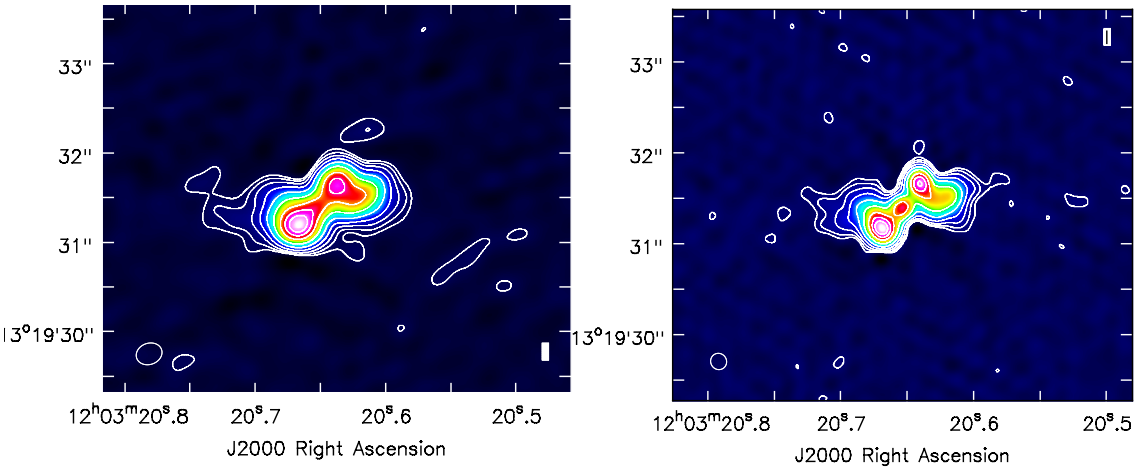

FIGURE 3.3: (left) The uniform weighted 6 GHz VLA image of 2MASXJ12032061+131931. The beam size is $0.29'' \times 0.24''$. The rms noise in the image is ~ 20 μJy. The contour levels correspond to 0.60, 1.25, 2.5, 5, 10, 20, 40, 60, 80 % of peak flux density at 11.90 mJy. (right) The uniform weighted 8.5 GHz VLA image of 2MASXJ12032061+131931. The beam size is $0.18'' \times 0.17''$. The contour levels correspond to 0.60, 1.25, 2.5, 5, 10, 20, 40, 60, 80 % of peak flux density value at 6.86 mJy.

structure is completely resolved at these frequencies and the deconvolved core has a size of $\sim 0.1''$ or 116 pc (Table 3.5). However, at 8.5 GHz the naturally weighted image (Figure 3.3) shows the full extent of the helical S-shaped jet structure out to a radius of approximately $\sim 1.5''$ or 1.74 kpc. Interestingly, both the high and the low resolution maps show distinctive curved radio jets, thus producing the S-shaped morphology for the radio source. The helical structure of the jets is very clear since the hot spots lie along the NW-SE direction, but the extended radio emission lies along the NE-SW direction.

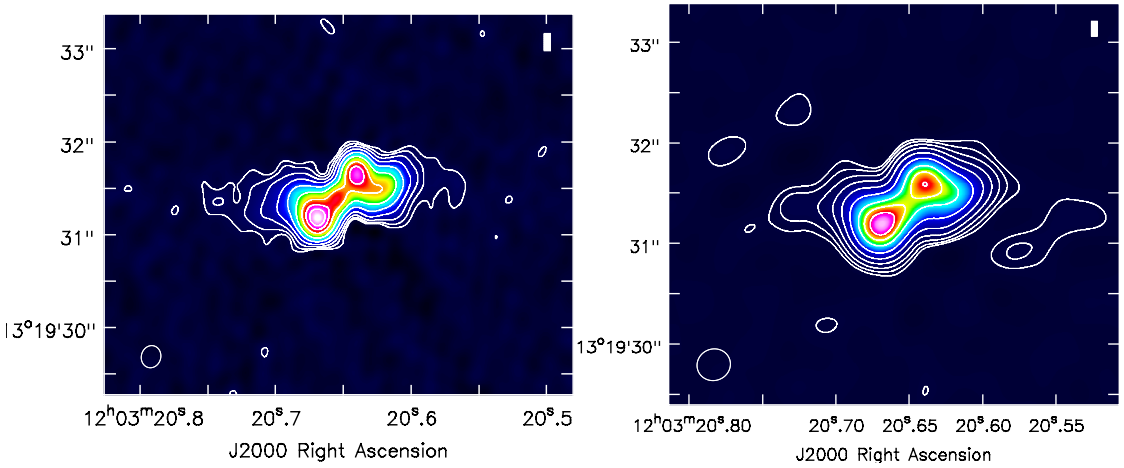

FIGURE 3.4: (left) The naturally weighted 8.5 GHz VLA image of 2MASXJ12032061+131931. The beam size is $0.24'' \times 0.21''$. The contour levels correspond to 0.60, 1.25, 2.5, 5, 10, 20, 40, 60, 80% of peak flux density at 8.20 mJy. (right) The naturally weighted radio contour map 2MASXJ12032061+131931 at 15 GHz. The beam size is $0.33'' \times 0.31''$. The contour levels correspond to 0.60, 1.25, 2.5, 5, 10, 20, 40, 60, 80% of peak flux density value of 7.30 mJy.

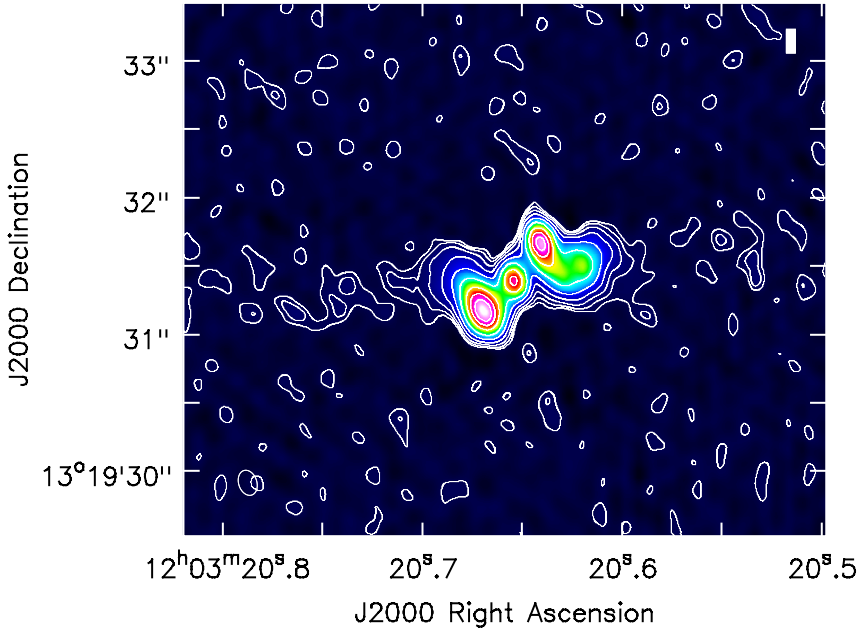

FIGURE 3.5: The uniform weighted radio contour map 2MASXJ12032061+131931 at 11.5 GHz. The beam size is $0.19'' \times 0.13''$. The contour levels correspond to 0.60, 1.25, 2.5, 5, 10, 20, 40, 60, 80% of peak flux density of value 4.90 mJy.

TABLE 3.5: **Radio Properties of 2MASXJ12032061+131931:** Column 1: VLA array configuration; Column 2: Robust parameter of Briggs weighting; Column 3: RMS noise; Column 4: Core size; Column 5: Peak flux of the core; Column 6: Size of East jet; Column 7: Peak flux in SE hotspot; Column 8: Size of West jet; Column 9: Peak flux in NE hotspot.

	Array configuration	Robust parameter	Image Noise in μJy	Core Size in $\theta_M \times \theta_N$ ($''$)	Core Peak Flux in mJy	East Jet size in $''$	South East Hotspot Peak Flux in mJy	West Jet size in $''$	North West Hotspot Peak Flux in mJy
6 GHz	A	-0.5	21	not resolved	–	1.50	11.90	1.03	8.40
8.5 GHz	A	-0.5	14	0.24×0.18	3.8	1.11	6.86	1.20	5.68
8.5 GHz	A	0.5	17	Not resolved	–	1.50	8.20	1.45	6.40
11.5 GHz	A	-0.5	19	0.20×0.14	3.2	1.05	4.90	0.96	4.44
15 GHz	B	-0.5	13	Not resolved	–	0.90	7.30	0.90	5.00

3.2.3.2 The 2D decomposition of the galaxy image

Dual AGN are rare in spirals, and S-shaped radio sources are usually associated with major mergers of elliptical galaxies (e.g. NGC 326). Hence, it is important to see if 2MASXJ1203 is an elliptical or a spiral galaxy. To determine the morphological class of 2MASXJ1203, we used GALFIT to first fit a single Sersic profile (which is used for elliptical galaxies) to the SDSS I band image. The fit is shown in Figure 3.6. The fit appears to be good and has a χ^2 value of 1.097. However according to Fathi et al. (2010) 2MASXJ1203 could be an S0 type galaxy. Therefore, we tried with two components simultaneously - a Sersic profile for a bulge and an exponential profile for a disk. While the two component fit results in an identical χ^2 value, the residual image looks better compared to the single component fit. GALFIT therefore favours the disky morphology for the host galaxy. However, the exposure time for the SDSS image is very short. A deeper image is required to confirm the morphological class of 2MASXJ1203.

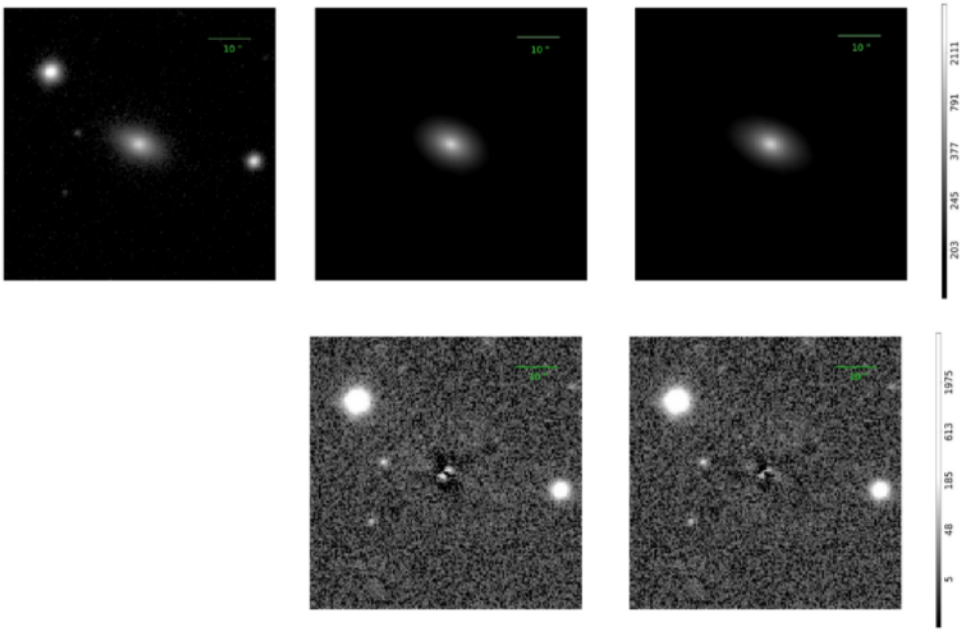

FIGURE 3.6: The optical image of the host galaxy of 2MASXJ1203 is fitted with Sersic and exponential profiles. Starting from the top left panel and moving from left to right, is the original galaxy image, the model with a single Sersic profile, and the model with a Sersic plus an exponential profile. The second row presents the residual images from the models presented immediately above. The color bars at the extreme right apply to all images in the respective rows. In all images, North is to the top and East towards the left.

3.2.3.3 SMBH mass, Eddington ratio and Star Formation Rate

We have used the velocity dispersion of the underlying stellar component to calculate the total mass of the central bulge which is also an upper limit to the mass of the dual SMBHs. Using the nuclear stellar velocity dispersion $\sigma_\star$ that we derived (Section 3.2.2) from the SDSS DR12 spectrum (Figure 3.2) and the M-$\sigma_\star$ relation in McConnell & Ma (2013), we obtained an upper limit of $M_{BH} = (1.56 \pm 0.26) \times 10^8 M_\odot$ for the SMBHs. Furthermore, we used an approximate model of a binary system with the components M_A and M_B in circular orbits about a common center of mass to obtain a very rough approximation for the individual SMBH masses. There are several assumptions in this calculation -

(i) there has been a major merger and the bulges have relaxed and hence the M-σ relation is valid, (ii) the BHs are rotating in a Keplerian disk with a separation of 0.1-2 kpc and the [O III] peaks trace their relative velocity, (iii) both SMBHs are accreting at a similar Eddington rate. According to Kepler's law, for a binary system the orbital velocity ratio of the two components is given by Wang et al. (2009)

$$V_A/V_B = M_B/M_A = \Delta\lambda_A/\Delta\lambda_B = 2.57/2.37 = 1.084.$$

Here V_A and V_B are the Doppler redshift and blueshift velocities of the [O III] line. $\Delta\lambda_A$ and $\Delta\lambda_B$ are the Doppler redshift and blueshift of the [O III] line in units of Åwhich have values of 2.57 and 2.37 respectively (Wang et al. 2009). Using the total mass to be $(1.56 \pm 0.26) \times 10^8 M_\odot$ the individual SMBHs are $\sim 0.82 \times 10^8 M_\odot$ and $\sim 0.74 \times 10^8 M_\odot$. In general, however, a constant separation between the SMBHs will not perturb the accretion disks and produce AGN activity; also the orbits are more likely to be elliptical than circular. We note that this calculation only gives a rough estimate of the individual SMBH masses since there is no clear signature of a major merger in the optical image, as mentioned in Section 3.2. The separation is also not confirmed as we will discuss later in Section 3.2.4.2

We have obtained the blue-shifted (16.6×10^{-16} erg cm^{-2} s^{-1}) and red-shifted (19.1×10^{-16} erg cm^{-2} s^{-1}) narrow-line [O III]λ5008 fluxes from Ge et al. (2012). The total flux density is 35.7×10^{-16} erg cm^{-2} s^{-1}. The [O III] luminosity turns out to be 2.79×10^{40} erg s^{-1}. We have estimated the bolometric luminosity (L_{bol}) using the relation from Heckman et al. (2004): $L_{bol}/L_{[O\ III]} \approx 3500$ and it's value is $L_{bol} = 9.79 \times 10^{43}$ erg s^{-1}. For a BH mass $(1.56 \pm 0.26) \times 10^8 M_\odot$, the Eddington luminosity ($\equiv 1.25 \times 10^{38} M_{BH}/M_\odot$) is $\approx 1.87 \times 10^{46}$ erg s^{-1}. The Eddington ratio in 2MASXJ1203 (L_{bol}/L_{Edd}) is ~ 0.0052 which is typical for Seyfert galaxies (e.g.,

Ho 2008).

The star formation rate (SFR) are derived for the nuclear region in 2MASXJ1203 using the UV flux and the H_α line emission estimated from the SDSS optical spectrum. We have assumed a Salpeter initial mass function (IMF) (Salpeter 1955) and stellar mass limits of 0.1 to 100 $M_\odot$ (Kennicutt 1998b). The UV SFR is $\sim$ 0.105 $M_\odot \mathrm{yr}^{-1}$ for the GALEX NUV flux of our target which is 9.60 μJy. We have obtained the H_α flux from the SDSS nuclear spectrum of 2MASXJ1203 and it has a value of 25.3×10^{-16} erg cm^{-2} s^{-1}. This yields a nuclear SFR of $\sim 0.156\ M_\odot\ \mathrm{yr}^{-1}$. The full H_α luminosity is from both star formation as well as from AGN activity. In order to obtain the SFR, we need to subtract the AGN contribution from the H_α line luminosity. We have used the AGN contribution as 70% (see chapter 4). The corrected SFR range is 0.056 $\mathrm{M}_\odot\ \mathrm{yr}^{-1}$. The GALEX UV flux is from the entire galaxy and the SDSS H_α emission is from the central region ($\sim 3''$ diameter SDSS fibre). Similar SFRs have been derived from infrared data in other Seyfert galaxies (Kharb et al. 2016)

We also checked the optical variability of 2MASXJ1203 using the Catalina Real-time Transient Survey (CRTS)[‖] (Drake et al. 2009). CRTS is a large sky, optical survey which publishes the light curves of sources within minutes of their observations. Thus the flux variation of transient sources with time can be obtained from CRTS data. However, for 2MASXJ1203 no clear periodicity is evident from its CRTS data.

3.2.3.4 Spectral index

The core has a spectral index value of $\alpha_{8.5}^{11.5} \sim -0.60 \pm 0.02$ between 8.5 GHz and 11.5 GHz which is moderately steep. Steep spectrum cores have sometimes been

[‖]http://nesssi.cacr.caltech.edu/DataRelease/

observed in Seyfert galaxies (Peck & Taylor 2001). The SE hotspot has a spectral index of $\alpha_{8.5}^{11.5} \sim -0.76 \pm 0.01$ and the NW one $\alpha_{8.5}^{11.5} \sim -0.72 \pm 0.02$ respectively (Figure 3.7). We have obtained the spectral index values of jets using the 6 GHz and 15 GHz images. The values are $\alpha_{6}^{15} \sim -0.68 \pm 0.01$ and $\alpha_{6}^{15} \sim -0.61 \pm 0.01$ for the SE and NW hotspot respectively (Figure 3.7). These spectral index values for the lobes are typical of lobes associated with jets in large radio galaxies (e.g., Laing & Peacock 1980; Dennett-Thorpe et al. 1999; Kharb et al. 2008).

3.2.3.5 Modeling the helical Jet-precession

S- or Z- shaped jets have been observed in many galaxies. Hutchings, Price & Gower (1988) found that almost 30 % of all quasars with z < 1 and radio structures show an S-shape. Pronounced S-shaped jets are often termed helical jets and can be explained in terms of precessing jets (Ekers et al. 1978; Parma, Ekers & Fanti 1985). We have modeled the helical jets in 2MASXJ1203 using the Hjellming & Johnston (1981) model, since it is simple and does not assume any origin for the jet precession. The model was used for SS433 but it can be used for extra-galactic jets as well. From visual inspection we have derived the proper motion plot that matches the radio image in the following way. We started with a typical jet advance speed of 0.03c (Ulvestad 2003) and varied the inclination angle i and half opening angle (ψ) from 0 to 90°. The best fitting model values are $i = 52°$, $\psi = 21°$, $v = 0.023$c, precession period $P = 0.95 \times 10^5$ years. Such precession timescales have been found for the jets of the Seyfert galaxy Mrk6 as well (Kharb et al. 2006). The angle of rotation required to rotate the geometrical model to align it with the 11.5 GHz image is $\chi = 33°$. The proper motion is plotted for a jet precession timescale of $t = 1.5 \times 10^5$ years in Figure 3.8. To estimate the errors associated with our precession model we determined the range of parameters that can fit the radio morphology in the following way. We fixed all the parameters except one and then varied this parameter until the visually identified fit got significantly

worse (Steenbrugge & Blundell 2008). The parameter ranges that we obtained were $i = 52° \pm 5°$, $\psi = 21° \pm 2°$ and $\chi = 33° \pm 3°$. The range of precession period is $P = (0.95 \pm 0.05) \times 10^5$ years. The best fitting velocity which gives jets of the same size as in the radio image with the above parameters is $v = 0.023c$. Small changes in jet velocity around this value do not change the shape much. But if v is continuously increased, the jets start showing relativistic effects which make the jet structure look increasingly asymmetric.

One of the most common explanations for jet precession is the presence of a binary black hole system, where the interaction of the black holes perturbs the spin of one or both black holes resulting in precessing jets (Blundell & Bowler 2004; Romero et al. 2000; Roos, Kaastra & Hummel 1993). Apart from binary black-hole systems, helical jets can arise when an accretion disk is irradiated by the central AGN and becomes unstable and warped thus producing jet precession (Pringle 1996; Livio & Pringle 1997); it can also be due to the net change in the spin of the SBMHs which affects the orientation of the radio jets (Rees 1978; Natarajan & Pringle 1998a). Models with accretion disks of single AGN have also been developed (Lu 1990). Black-hole mergers can result in short-timescale redirection of the jet axis (Merritt & Milosavljević 2005b) and this may also lead to bent radio jets, but these are X-shaped rather than S-shaped jets.

3.2.3.6 Equipartition Estimates and Lifetimes

We have obtained the magnetic field corresponding to the minimum total energy of the synchrotron emitting plasma which is close to the equipartition of the energy in particles and the magnetic field (Burbidge 1959). Using the radio luminosity (O'Dea & Owen 1987), we obtain the following expression.

$$L_{rad} = 1.2 \times 10^{27} {D_L}^2 S_0 {\nu_0}^{-\alpha} (1+z)^{-(1+\alpha)} ({\nu_u}^{1+\alpha} - {\nu_l}^{1+\alpha})(1+\alpha)^{-1}$$

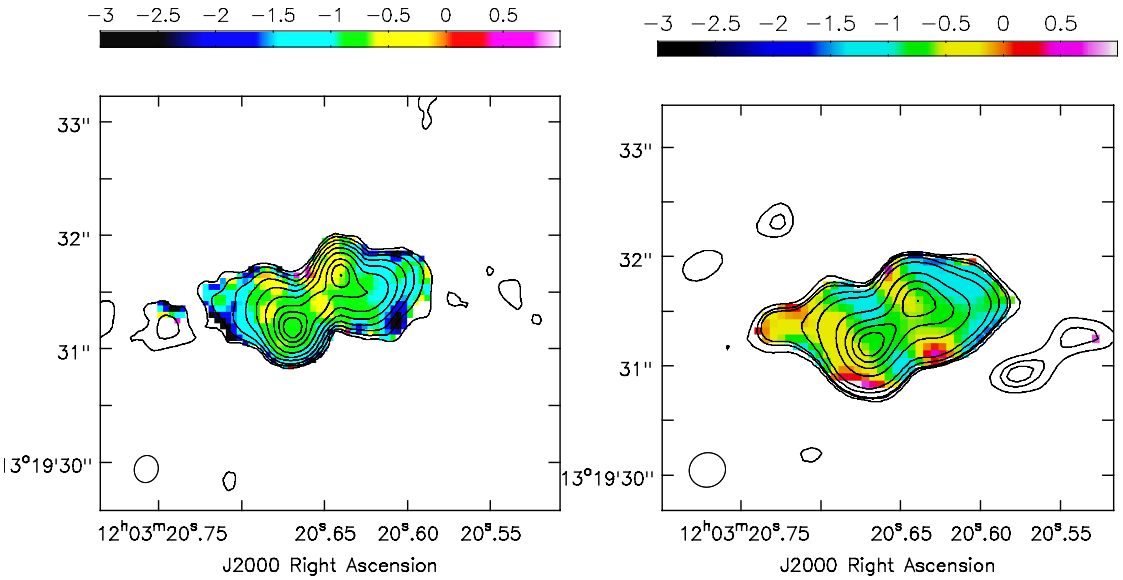

FIGURE 3.7: (left) The 8.5-11.5 GHz spectral index image in colour, superimposed by 8.5 GHz radio contours with levels corresponding to 60, 1.25, 2.5, 5, 10, 20, 40, 60, 80% of peak flux density value at 8.2 mJy. (right) The 6-15 GHz spectral index image in colour, superimposed by 15 GHz radio contours with levels corresponding to 60, 1.25, 2.5, 5, 10, 20, 40, 60, 80% of peak flux density value at 7.3 mJy.

$$B_{min} = [2\pi(1+k)\ c_{12}\ L_{rad}\ (V\phi)^{-1}]^{2/7}$$

Where L_{rad} is the radio luminosity in erg s^{-1}, D_L is the luminosity distance in Mpc, z is the redshift (Table 3.3), S_0 is the total flux density in Jy, ν_0 is the frequency in Hz, ν_u and ν_l are the upper and lower cutoff frequencies respectively in Hz, k is the ratio of the relativistic proton to relativistic electron energy, V is the source volume, c_{12} is a constant depending on the spectral index and frequency cutoffs (Pacholczyk 1970), ϕ is the volume filling factor and B_{min} is the magnetic field at minimum pressure in Gauss. We have used the total flux density $S_0 = 0.29$ Jy from the 11.5 GHz (ν_0) image (Figure 3.7). The minimum magnetic field is calculated using the following assumptions: the radio spectrum extends from 100 MHz to 15 GHz with a spectral index value of $\alpha = -1$ (Figure 3.4). The relativistic electrons and protons have similar energy i.e k = 1. The jets are uniformly filled with relativistic particle and magnetic field i.e $\phi = 1$. We have assumed cylindrical

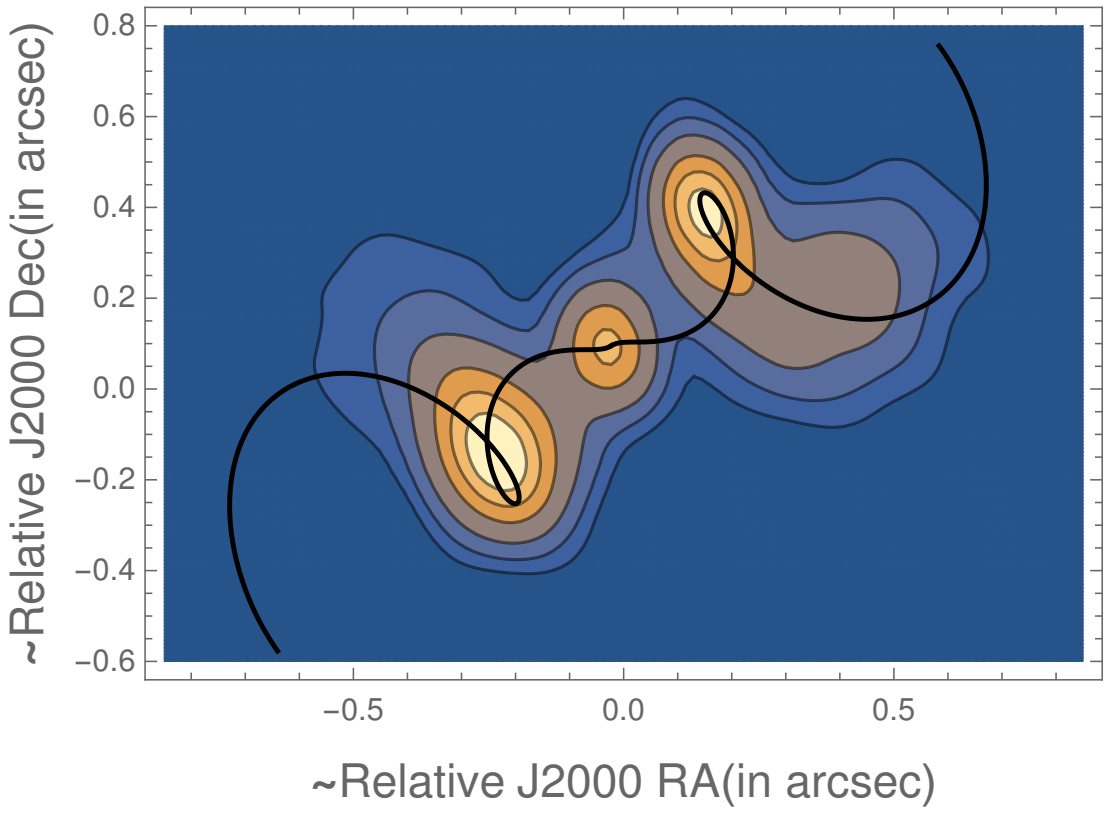

FIGURE 3.8: The uniform weighted 11.5 GHz radio image of 2MASXJ12032061+131931 in color, superimposed by the precessing jet model of Hjellming & Johnston (1981) in black. The best-fit parameters are described in Section 3.2.3.5.

symmetry for the jet and calculated the volume, $V = \pi(w/2)^2 l$, using a length of $l \sim 3$ kpc and a width of $w \sim 0.4$ kpc. The parameter c_{12} is 6.5×10^7 for our observed frequency. The estimated total radio luminosity is $1.9{\times}10^{41}$ erg s^{-1}. We obtain a minimum magnetic field of 105 μG for a plasma filling factor of $\phi = 1$.

We have used the relation from van der Laan & Perola (1969) to estimate the lifetime of electrons in the radio component undergoing both synchrotron radiative and inverse-Compton losses due to cosmic microwave background (CMB) photons,

$$t \approx \frac{2.6 \times 10^4 \; {B_{min}}^{1/2}}{({B_{min}}^2 + {B_R}^2)[(1+z)\nu]^{1/2}}$$

where B_{min} is the minimum magnetic field from equipartition in Gauss (G); $B_R \simeq 4 \times 10^{-6}(1+z)$ G is the magnetic field equivalent to the radiation, which

was assumed to be predominantly CMB photons and ν is the electron radiation frequency in Hz. For the estimated magnetic field of 105 μG at 11.5 GHz we obtained the lifetime of electrons to be t $\approx 2.1\times 10^5$ yrs.

The age of the source can also be estimated via the spectral ageing analysis (Myers & Spangler 1985). We have used Figure 3 from Myers & Spangler (1985) to obtain a rough estimate of X_0 which is the measure of maturity of synchrotron losses. We have used the α_6^{15} values (Figure 3.7) at the initial hot spots and where jet falls below 3σ; these frequencies match those used in Figure 3 of Myers & Spangler (1985). We have used the Kardashav-Poacholczyk (KP) model which assumes an isotropic pitch angle distribution. The initial electron energy is from synchrotron radiation which follows a power law. The magnetic field is assumed to be the equipartition value. The estimated timescale is t $> 1.3\times 10^5$ yrs. This is a lower limit since only the hot spot and the tail were considered instead of the entire core-jet structure. We have calculated the jet speed using the synchrotron time i.e 2×10^5 yrs and the size of one-side jet i.e 1.5 kpc which comes out to be $\beta = 0.023$. The calculated jet advance speed is the same as was obtained from the precession model in Section 3.2.3.5. The timescale is of the order of $\sim 10^5$ which is also consistent with the precession timescale obtained in Section 3.2.3.5.

3.2.4 DISCUSSION

Our radio observations show that 2MASXJ1203 has a core-jet structure with S-shaped or helical jets. In this section we discuss the mechanisms that could explain the radio observations of the DPAGN in 2MASXJ1203.

3.2.4.1 Mechanisms Causing S-shaped Core Jet Structures

In the literature, Z or S-shaped radio galaxies are referred to as X-shaped galaxies (Cheung & Springmann 2007). However, it is very difficult to explain this morphology with the models for X-shaped galaxies which consist mainly of (i) spin flip of a SMBH (Natarajan & Pringle 1998a) or (ii) backflow of plasma in radio jets (Leahy & Williams 1984a). In the back-flow model, the ISM of the host elliptical galaxy exerts a buoyancy pressure on the back-flowing plasma causing secondary wings of plasma to form from the terminal shocks evolving in the hot medium (Capetti et al. 2002). The rapid cocoon expansion along the direction of the hosts minor axis produces the X-shaped morphology. The relationship between the optical axis and wing orientation indicates that the formation of the XRSs is intimately related to the host galaxy's geometry (Gillone, Capetti & Rossi 2016). These results strengthen the interpretation that the X-shaped morphology in radio-sources has a hydrodynamical origin. The back-flow model can explain the radio structures associated with the large FR I Fanaroff & Riley (1974) galaxies. But the model is not able to explain why the secondary lobes are larger than the primary lobes in many radio galaxies such as NGC 326, 4C+00.58 (Hodges-Kluck et al. 2010). However, 2MASXJ1203 cannot be classified as an FRI radio source due to its small size and the secondary wings are larger than the primary. There is also no evidence of cocoon formation in the radio images. Therefore, the back-flow model cannot explain the radio morphology of 2MASXJ1203. Gopal-Krishna, Biermann & Wiita (2003) have proposed a different model which can explain both X and Z-shaped sources. In this model, as a galaxy spirals into the nucleus of the host galaxy, it perturbs the axisymmetric disk potential, causing disk rotation in the interstellar medium (ISM) of the host galaxy (Noel-Storr et al. 2003). The gas in the disk will interact with the jets causing them to bend at large radii - this may appear as jet precession i.e. Z or X shaped radio jets. A good example is the Z-shaped galaxy NGC 3801 (Das et al. 2005). Hota et al. (2009) showed that Z-shaped radio jets in NGC 3801 have gone through a recent merger and

it has a large fast rotating gas disk interacting with jets. In our case, however, there is no indication of jet-ISM interaction and our radio jets have small radii of $\sim$ 1.5 kpc. Thus, this model is probably not the explanation for the S-shaped radio jet morphology in 2MASXJ1203.

A helical jet structure can also be due to jet precession during the lifetime of a radio source (Ekers et al. 1978). The jet precession model fits the radio image of 2MASXJ1203 (see Section 3.2.3.5) and the calculated jet precession timescale is similar to the age of the electrons in the lobes i.e 10^5 yrs (see Section 3.2.3.6). Therefore, jet precession is the most probable explanation for the S-shaped radio structure of 2MASXJ1203. We discuss jet precession in greater detail in the next section.

3.2.4.2 Mechanisms Causing Jet Precession

S-symmetry due to precession has long been predicted associated with the presence of binary SMBHs (Begelman, Blandford & Rees 1980b). The secondary BH can induce the rapid precession in the inner region of the primary accretion disk (Romero et al. 2000). The motion of the secondary BH around the primary BH can also cause the orbit to precess resulting in helical or S-shaped radio jets (Roos, Kaastra & Hummel 1993; Valtonen et al. 2016). A good example is the BL Lac object Mrk 501 that has helical jets which can be explained by binary SMBH models (Villata & Raiteri 1999). We have calculated the separation of the binary system which can give the precession period of 10^5 years. The relation, $P_{prec} \sim 600\ {r_{16}}^{5/2}(M/m)\ {M_8}^{-3/2}$ yr (Begelman, Blandford & Rees 1980b) gives a separation of $\sim$ 0.02 pc, where r_{16} is the separation in units of 10^{16} cm, M_8 is the mass of the primary SMBH in units of 10^8 $M_\odot$ and (M/m) is the mass ratio of the primary SMBH to the secondary SMBH. We have used the mass ratio 1.084 and

$M_8 \sim 0.82$ (Section 3.2.3.3). Therefore, there could be a second SMBH at a separation of 0.02 pc in 2MASXJ1203, which we cannot detect with the present day telescopes. The other possibility could be that there exists a dual SMBH system and the secondary SMBH has passed the primary SMBH in the past; this could have induced the precession in the jet of the primary SMBH. Here the secondary SMBH may not have sufficient radio flux density to be detected in our observation; higher resolution observations however, could detect it, if present. In the case of 2MASXJ1203, there appears to be a second NIR Core in the Keck NIRC2 image (McGurk et al. 2015). The image contains a second core at a separation of 2.1 kpc from the nucleus. However, spectroscopic observations have not been carried out. The second faint core could form a DAGN system with the nuclear SMBH in the bulge. However, we cannot rule out an AGN-starburst system either. If the faint NIR core is a SMBH it does not have enough radio flux density to be detected in our maps. This second SMBH could cause the jet precession in 2MASXJ1203.

Although binary AGN models are interesting, a single AGN model can also explain the helical jet morphology. On the basis of the Sarazin, Begelman & Hatchett (1980) model for SS433, Lu (1990) suggested that a tilted accretion disk can also produce jet precession. This model of a tilted accretion disk around a single AGN gives a relation between the precession period and the luminosity. The radio source 1946+708 has jets with a tilted disk (Peck & Taylor 2001) and the observed morphology follows the period-luminosity relation of Lu (1990). The precession period is usually calculated using several precession models which have very large uncertainties and the magnitude values also differ from literature to literature. We have used the period-luminosity relation where the absolute B-band magnitude of our target** is M_{abs} = -20.34 and the calculated precession period is $\sim 10^5 - 10^9$ yrs. We note that the timescale uncertainties are very large. However, our jet precession model time estimate of $\sim 10^5$ yrs that was obtained in Section 3.2.3.5, falls within this time range. It is possible that the accretion disk

**http://leda.univ-lyon1.fr/

in 2MASXJ1203 has become warped or tilted due to non-uniform irradiation from the AGN. Such radiation can cause the accretion disk to become unstable and warped, resulting in jet precession (Pringle 1997). In radio images, we have not detected the second core so we cannot distinguish between these two mechanisms of precession. Thus in summary the jet precession in 2MASXJ1203 can be due to a close SMBH binary at a separation of 0.02 pc, a dual system in which a close passing of an SMBH has induced the precession or a single AGN with an warped accretion disk that has given rise to jet precession.

3.2.4.3 Is 2MASXJ1203 a CSS/CSO source ?

The other class of radio sources into which 2MASXJ1203 falls is that of the compact steep spectrum (CSS) objects or compact symmetric objects (CSO). Gigahertz peaked-spectrum (GPS)($\leq$1 kpc) and CSS ($\leq$20 kpc) sources are small bright sources with steep spectra and are young ($\leq 10^5$ yrs). CSS and GPS sources can be used to probe the NLR of AGN host galaxies (O'Dea 1998). CSO are radio objects which have compact symmetric double lobes that extend to small galactic radii of ≤ 1 kpc (Wilkinson et al. 1994). CSO are a subclass of GPS with symmetric jets. CSS are also symmetric in structure. Fanti et al. (1995); Readhead et al. (1996) have proposed that GPS and CSS are the evolutionary stages of large radio galaxies i.e GPS $\rightarrow$ CSS $\rightarrow$ large radio galaxies. Some CSOs show S-symmetry (Deane et al. 2014) which can be signature of binary SMBHs (Begelman, Blandford & Rees 1980b). The binary AGN with the smallest separation, 0402+379, is a CSO (Rodriguez et al. 2006b). We have calculated the break frequency of 2MASXJ1203 using $t_s = 1610 B^{-3/2} \nu_b^{-1/2}$ Myr from (Carilli et al. 1991), where t_s is the synchrotron age , B is the magnetic field and ν_B is the break frequency. We have used $t_s = 10^5$ yrs, B= 105μG from Section 3.2.3.6. The calculated break frequency is $\nu_B \sim 0.55$ GHz. This ν_B is in the break frequency range observed in CSO/CSS sources (Murgia 2003). The radio observations of 2MASXJ1203 show

an S-shaped jet of total extent ~ 3 kpc, the average spectral index $\alpha_{8.5}^{11.5} \sim -1$, ν_B is 0.55 GHz and the estimated age is $\sim 10^5$ yrs. Thus 2MASXJ1203 is a CSS/CSO source and its S-symmetry could be consistent with the binary/dual SMBH scenario.

3.2.4.4 Origin of Double-peaked [O III] line

Double peaked emission lines from the NLR have been detected in nuclear galaxy spectra since the 1970s (Sargent 1972b; Heckman et al. 1981) and are important for studies of NLR kinematics. It was previously thought that DPAGN emission lines are indicators of bipolar outflows or rotating disks (Greene & Ho 2005). However, they are now thought to also indicate the presence of binary or dual AGN (Zhou et al. 2004) at the separations of ∼100 pc to ∼10 kpc respectively (Wang et al. 2009). Since the data of large spectroscopic surveys such as SDSS became available (Smith et al. 2010; Fu et al. 2012), there has been a greater interest in finding large sample of DPAGNs since they may represent DAGN. However, there are several other mechanisms that can produce double-peaked emission lines from a single AGN (Xu & Komossa 2009). For example, jet-cloud interaction can also produce a DPAGN (Rosario et al. 2010). Smith et al. (2010) suggest that if two Gaussian components of a double-peaked [O III] line are symmetric than it can be explained by a rotating ring. Thus, it is very difficult to confirm the presence of dual/binary AGN just from DPAGN emission and one has to carry out high resolution imaging to confirm it. Tingay & Wayth (2011a) conducted a VLBI study of DPAGN to search for dual/binary AGN but they have not detected any. Comerford et al. (2012b) used an additional criteria to detect DAGN from a sample of DPAGN; they used long-slit spectroscopy to separate the outflow and rotating disks from candidate dual/binary AGN sources. They found 17 promising dual AGN candidates from 81 DPAGN sources. Müller-Sánchez et al. (2015b) have

tried to constrain the origin of DPAGN using VLA observations along with long-slit spectroscopic studies. They find that 15% of their sample are dual AGN and in 75% the DPAGN are due to gas kinematics. From these recent studies, it appears that DPAGN may not be promising candidates for dual/binary AGN.

In our study, we do not have a two dimensional [O III] map of the gas kinematics or high resolution long slit observations for our target. Therefore, we cannot be sure about the origin of the double-peaked emission lines in 2MASXJ1203 just from the SDSS spectrum. However, just to check if the double peaked [O III] lines could be due to two SMBHs, we used the velocity separation $\Delta v = 292\ km\ s^{-1}$ of the [O III] emission lines (Ge et al. 2012) to make an approximate estimate of the SMBH separation using $\Delta R \sim GM/(\Delta v)^2$ and used it to derive a precession timescale. The calculated separation for $M = 10^8\ M_\odot$ is ~ 8 pc. Using this value in equation 7 from Begelman, Blandford & Rees (1980b) gives a precession period of 4.6×10^{11} yrs which is more than the Hubble time. This value contradicts the model precession timescale (which is due to a binary of separation of 0.02 pc) as well as the synchrotron lifetimes of electrons in the radio jets, both of which are of the order of $\sim 10^5$ yr. Thus in the precession model it is not possible that a close binary is the origin of the double peaked emission lines in the SDSS spectrum of 2MASXJ1203. However, it could be that there is a dual system in which the precession has been induced during a close pass; in that case we cannot rule out the possibility that the DPAGN is due to two AGN. Alternatively, there is only a single AGN in which case the jet-ISM interaction is the probable origin of the DPAGN emission line. The kpc radio jets may be responsible for the double-peaks through jet-medium interaction.

3.2.4.5 Detecting the dual/binary AGN in 2MASXJ1203

The S-shaped radio morphology of 2MASXJ1203 is due to slow precession of jets during its lifetime and it is a CSS/CSO source. We have considered three scenarios for jet precession: (i) binary AGN at the separation of 0.02 pc, (ii) a dual AGN system where a close pass of the secondary SMBH in the past has given rise to the jet precssion or (iii) a single AGN with a tilted accretion disk. If the first case is true, i.e., the separation is 18 micro-arcseconds in the sky, we cannot resolve the second AGN with current ground-based VLBI telescopes. With our present data we are not able to rule out any of these possibilities but future higher resolution observations may help us if the SMBHs are at separation lying between $40 \leq d \leq 100$ pc. If the separation is more than 100 pc, the second AGN does not have sufficient radio flux density since it has not been detected in our observations.

3.2.4.6 The relevance of DPAGN to dual/binary AGN studies

Recent high resolution radio observations have shown that DPAGN are not usually dual/binary AGN (Shen et al. 2011; Fu et al. 2011b) as indicated by earlier studies and DAGN appear to be far more elusive than thought. However, they are very important for understanding the nuclear disk kinematics and good indicators of kpc scale radio jets or outflows (Müller-Sánchez et al. 2011; Kharb et al. 2015b). The lack of parsec scale resolution and the absence of radio or X-ray emission in a significant fraction of AGN makes it harder to detect DAGN. In some cases the NIR images or radio morphologies may have indirect signatures of the SMBH pair - such as lopsided disks or S-shaped jets as in 2MASXJ1203. These cases need to be followed with higher resolution observations. Thus multi-wavelength and high resolution observations are essential to detect dual/binary AGN in DPAGN galaxies.

The AGN in 2MASXJ1203 shows not only S-shaped precessing jets but also double peaked emission lines in its optical nuclear spectrum, both of which are signatures of dual AGN. However, it is possible that one of the AGN does not have significant radio emission or is so weak that its flux density lies below the detection limit in the 8.5 GHz and 11.5 GHz radio images. X-ray observations with high enough resolution is another way to detect the dual/binary AGN. Another possibility is that one of the SMBHs in the dual/binary system is accreting at a very low Eddington rate, resulting in AGN activity that is too weak to detect. In that case, the only way to detect the two SMBHs is by using high resolution near-infrared (NIR) imaging of the stellar bulges associated with the SMBHs. In fact the NIR imaging of 2MASXJ1203 already shows faint signatures of a small NIR compact core offset from the main bulge of the galaxy (McGurk et al. 2015). It can be possible that the galaxy has gone through a recent minor merger event leading to dual SMBHs in the nuclear region but leaving the galaxy relatively undisturbed. The probable ∼335 pc size of the SMBH pair suggests that 2MASXJ1203 is a good candidate for gravitational wave studies.

3.3 Summary

We summarise the conclusions of our study below:

1. We have selected 20 DPAGN galaxies on the basis of ΔV vs σ plot to search for dual AGN. Here, 8 galaxies are from sample 1 which have low redshift, disky morphologies and $\Delta V \geq 400$ km s^{-1}. Sample 2 have 12 galaxies irrespective of their morphologies and redshift and have $\Delta V \geq 400$ km s^{-1}. One of the sample galaxy 2MASXJ 12032061+1319316 is discussed here.

2. We have carried out radio imaging of the double-peaked emission line Seyfert 2 galaxy 2MASXJ1203 using VLA at 6, 8.5, 11.5 and 15 GHz. The 6 and 15 GHz images show two distinct radio hot spots on either side of the optical nucleus.

3. The 8.5 and 11.5 GHz images obtained via archival data, reveal the full extent of the emission and we are able to resolve the core jet structure. The radio jets have an S-shaped helical structure extending out to a radius of $\sim 1.5''$ (1.74 kpc) on either side of a deconvolved core of size $\sim 0.1''$ (116 parsec).

4. We have modeled the helical-jet structure using the Hjellming & Johnston (1981) model. The best-fit jet advance speed is 0.023c and precession timescale is $\sim 10^5$ yrs. The half opening angle is $\psi = 21^\circ \pm 2^\circ$ and inclination angle for the radio jets is $i = 52^\circ \pm 5^\circ$.

5. We have calculated the minimum magnetic field value of 105 μG and the electron lifetime of $\sim 10^5$ years from the equipartition theorem. This timescale matches the time the precessing jet was "on" in this Seyfert galaxy, providing support to the precession model.

6. 2MASXJ1203 is compact steep spectrum/compact symmetric object. Such sources have been suggested to be binary AGN in the literature.

7. The presence of S-shaped precessing radio jets in 2MASXJ1203 can be due to binary/dual SMBH or a single tilted SMBH with accretion disk. Double-peaked emission lines also can be due to binary/dual AGN or NLR kinematics of a single AGN. While the binary/dual SMBH scenario is supported by several suggestions, we are unable to rule out other possibilities with the present data. Future high resolution multi-wavelength (radio, X-ray, optical) observations are required to get a clearer picture for the double-peaked AGN, 2MASXJ1203.

Chapter 4

Searching for dual AGN in galaxies using radio observations II: the remaining 19 sources[†]

In this chapter we present the results of our radio observations of the 19 galaxies from sample 1 and 2 that are discussed in chapter 3.1. As mentioned earlier the targets are selected from a survey of double-peaked emission line galaxies. Some VLA archival data was also used in this study and is discussed in this chapter. In the following sections we first we present our radio observations, the analysis and then discuss the results. The main result of our radio observations is that we have detected one confirmed DAGN, two DAGN strong candidates and two interesting sources that have extended core-jet structure. The details of the sample galaxies are given in table 3.2

[†]Results of this chapter are published in Rubinur, Das & Kharb (2018, 2019)

TABLE 4.1: **Observation catalogue:**

Observation ID	Observed Frequency (GHz)	Configuration	Expected resolution (″)	Observed time (h)
15A-068	6.0	A	0.33	2.00
16A-144	15.0	B	0.42	2.00
16B-002	8.5 and 11.5	A	0.20	2.67
13B-020 (NRAO archive)	8.5 and 11.5	A	0.20	–

TABLE 4.2: **List of flux density and phase calibrators in the observations:** Column 1: SDSS name of the galaxy; Column 2: VLA project ID; Column 3: Name of the flux density calibrator; Column 4: Name of the phase calibrator; Column 5: Date of observation.

Name	Project ID	Flux density calibrator	Phase calibrator	DOB
2MASXJ09120164+5320369	16B-002	3C147	J0854+5757	15th Nov 2016
UGC 05353	15A-068	3C147	J0956+2515	19th July 2015
	16A-144	3C286	J1013+2449	20th May 2016
SDSS J100602.13+071130.9	16B-002	3C147	J0954+1743	15th Nov 2016
SDSS J110215.68+290725.2	16B-002	3C147	J1125+2610	15th Nov 2016
SDSS J132318.81+030807.1	16B-002	3C286	J1354-0206	7th Jan 2017
2MASX J13245059+1758152	15A-068	3C147	J1327+2210	19th July 2015
2MASX J13490964+0404487	15A-068	3C147	J1354-0206	19th July 2015
SDSS J135558.08+001530.6	16B-002	3C286	J1354-0206	7th Jan 2017
2MASX J14131625+2119374	16B-002	3C286	J1436+2321	7th Jan 2017
2MASX J14203147+4008166	16B-002	3C286	J1416+3444	7th Jan 2017
2MASXJ14454130+3341080	16B-002	3C286	J1416+3444	7th Jan 2017
2MASX J15001769+1051100	16B-002	3C286	J1504+1029	7th Jan 2017
B31459+399NED01	16B-002	3C286	J1500+4751	7th Jan 2017
2MASX J15042218+4741116	16B-002	3C286	J1500+4751	7th Jan 2017
SDSS J160027+083742	16B-002	3C286	J1608+1029	7th Jan 2017
2MASX J16170895+2226279	15A-068	3C147	J1613+3412	19th July 2015
	16A-144	3C286	J1613+3412	29th May 2016
2MASX J16441390+2528286	15A-068	3C147	J1613+3412	19th July 2015
	16A-144	3C286	J1613+3412	29th May 2016
2MASX J23044283-0933454	15A-058	3C48	J0137+3309	25th June 2015
	13B-020	3C48	J2323-0317	20th Feb 2015
SDSS J233604.04+000447.1	15A-058	3C48	J2323-0317	25th June 2015
	16A-144	3C48	J2320+0513	20th May 2016

4.1 New and archival data

• Sample 1: Seven DPAGN were observed with the VLA at 6 GHz in the A-array configuration for 1.5 hours (Project ID: VLA/15A-068; Table 4.1). The observations were carried out with a 1792 MHz wide baseband centered at 5.935 GHz with 14 spectral windows (SPW), each window having 64 channels with a frequency resolution of 2 MHz. Each target source was observed for 4 minutes. Based on the preliminary results from the 6 GHz data, we planned to observe 5 out of 7 galaxies at 15 GHz, to obtain the spectral index images. However, we finally obtained 15 GHz VLA B-array data for only 4 galaxies because one galaxy already had high resolution VLA data available in the NRAO archive. The 15 GHz observations were carried out on 29 May 2016 (Project ID: VLA/16A-144; Table 4.1) with a 1890 MHz baseband centered at 14.9 GHz. Each of the targets was observed for 15 mins. The fifth galaxy in our sample, J2304, had VLA archival data at 8.5-11.5 GHz (Project ID:VLA/13B-020). J2304 was observed for 24 min at two central frequencies 8.5 GHz and 11.5 GHz.

• Sample 2: We observed 12 DPAGN in sample 2 with the VLA (Project ID: VLA/16B-002). The observations were done on 15 November 2016, at the two central frequencies of 8.5 and 11.5 GHz in A-array configuration with 1.6 GHz baseband at each frequency center with total of 16 spectral windows. The targets were observed for $\sim$6 minutes. The observational details are provided in Table 4.1. A list of the flux densities and phase calibrators are given in Table 4.2. The expected VLA resolution in the X band in the A-array configuration is $0.2''$. The highest redshift for a galaxy in our sample is $z = 0.355$ which gives a spatial scale of 7 kpc/$''$. So we can resolve up to 1.4 kpc in this galaxy with VLA observations, while SDSS can resolve only up to 21 kpc with its $3''$ fiber. Data reduction method is discussed in section 3.2.2.

4.2 Results

4.2.1 Total Intensity and Spectral Index Images:

We have imaged a total of 19 DPAGN with the VLA at different frequencies. We have found that three galaxies have dual radio cores, one galaxy shows kpc-scale core-jet structures and one shows an extended structure which can be due to a DAGN or represent the core-jet structure of a single AGN. Of the remaining 14 galaxies, 13 show single cores and one source is not detected. We have used the spectral index (α) maps to understand the nature of these radio cores. Additionally, we have used the FIRST map to determine whether extended radio emission is present or not in the galaxies. For this purpose, we have calculated the ratio (Table 4.5) of the integrated flux density to the peak intensity of the FIRST map [$\theta_{FIRST} = (S_{int}/S_{peak})^{1/2}$] (Singh et al. 2015) (Table 4.5). The sources are defined to be extended if $\theta_{FIRST} \geq 1.06$. In this section, we first describe our results for the galaxies that have clear dual radio cores and extended structures in our observations. Then we discuss all the single core galaxies together at the end of the section.

SDSS J100602.13+071130.9

J1006 (hereafter) is an interacting system. The projected nuclei separation is 5.2″ or 12 kpc. The morphology classification of this galaxy and its companion is uncertain. Both nuclei have SDSS spectra. J1006 is classified as a star-forming, AGN broad line source. The companion has a QSO spectrum. The radio images at 8.5 and 11.5 GHz (Figure 4.1) show two radio structures in this merger galaxy system at a separation of ∼5″ or 12 kpc. The radio emission of the main galaxy (A) is very faint (∼0.06 mJy at 8.5 GHz). The upper limit in spectral index value

TABLE 4.3: **Radio properties of the single AGN in our sample:** Column 1: Name of the galaxies; column 2: the observation frequencies; column 3: The beamsize: Major axis (θ_1), minor axis (θ_2) and position angle (PA); column 4: The RMS noise in μJy/beam; column 5: the flux density (S_{int}) in the intensity images in mJy; column 6: the spectral index value (α); **Note:** (a) An upper limit of α is given for extended sources. (b) α of the J1102 core is given.

Name	Frequency (GHz)	Beamsize ($\theta_1 \times \theta_2$, PA)	Noise (μJy/beam)	S_{int} (mJy)	α
2MASX J09120164+5320369	8.5	0.37″×0.24″, -80.62°	15.79	62.80	-0.43±0.01
	11.5	0.24″×0.18″, -61.63°	16.27	55.50	
UGC 05353	6.0	0.43″×0.29″, 76.55°	13.02	3.82	-0.82±0.03
	15.0	0.52″×0.38″, 78.14°	7.76	1.79	
SDSS J110215.68+290725.2	8.5	0.24″×0.19″, -67.32°	15.42	2.40	≤ -1.81±0.46[a]
	11.5	0.17″×0.15″, -19.23°	15.99	1.64	0.45±0.44[b]
SDSS J132318.81+030807.1	8.5	0.38″×0.21″, 87.56°	19.67	1.57	-1.50±0.78
	11.5	0.28″×0.17″, 88.53°	20.70	1.01	
2MASX J13245969+1758152	6.0	0.32″×0.30″, -59.36°	13.20	4.06	-
2MASX J13490964+0404487	6.0	0.35″×0.31″, -38.88°	13.67	19.39	-
2MASX J14131625+2119374	8.5	0.25″×0.19″, 84.45°	24.80	2.11	-0.31±0.18
	11.5	0.19″×0.15″, 83.12°	28.50	1.91	
2MASX J14203147+4008166	8.5	0.24″×0.16″, -64.74°	22.13	3.33	-0.23±0.20
	11.5	0.19″×0.12″, -62.17°	25.30	3.11	
2MASX J14454130+3341080	8.5	0.22″×0.18″, -60.66°	21.35	0.62	≤-1.40±1.16[a]
	11.5	0.17″×0.14″, -59.20°	24.36	0.40	
2MASX J15001769+1051100	8.5	0.30″×0.19″, -77.60°	21.46	$<6.43\times10^{-2}$	-
	11.5	0.23″×0.15″, -77.03°	24.50	$<7.35\times10^{-2}$	
B31459+399NED01	8.5	0.21″×0.19″, -42.04°	21.97	10.66	-1.04±0.07
	11.5	0.16″×0.15″, -45.96°	24.93	7.99	
2MASX J15042218+4741116	8.5	0.26″×0.21″, 8.94°	23.76	1.81	-0.11±0.07
	11.5	0.19″×0.16″, -5.77°	27.34	1.75	
SDSS J160027.78+083743.0	8.5	0.23″×0.19″, -53.99°	20.55	0.75	0.32±0.40
	11.5	0.19″×0.16″, -5.77°	23.79	0.83	
2MASX J16441390+2528286	6.0	0.43″×0.30″, -69.54°	14.40	11.79	-0.35±0.02
	15.0	0.60″×0.38″, -73.07°	7.76	8.93	
2MASX J23044283-0933454	6.0	0.48″×0.28″, 6.60°	12.85	1.60	-1.03±0.11
	11.5	0.52″×0.38″, 78.14°	7.76	1.16	
2MASX J233604.04+000447	6.0	0.41″×0.29″, 0.34°	19.20	3.18	-1.06±0.05
	15.0	0.58″×0.38″, -5.72°	7.39	1.20	

TABLE 4.4: **Radio properties of dual AGN in our sample:** column 1: Name of the dual AGN galaxies; column 2: this shows core no. Primary core is called as core 1 and secondary core as core 2; column 3: the observed frequencies in GHz unit; column 4: Beamsize; column 5: Flux density (S_{int}) in mJy unit; column 6: noise in μJy/beam; column 7: the spectral index value of individual core; column 8:separation (D) of the cores in arcsec; column 9: the separation (D) in kpc. **Note:** *The second core (B) in J1006 shows two lobes. The average α is given. The primary core (A) of J1006 and secondary core (B) of J1355 have an upper limit of α as these are detected with 4-5σ confidence.

name	core	Frequency in GHz	Beamsize ($\theta_1 \times \theta_2$, PA)	S_{int} (mJy)	Noise (μJy/beam)	α	D ($''$)	D (kpc)
SDSS J100602.13+071130.9	1	8.5	$0.28''\times0.22''$, 87.50°	$\leq 7.44\times10^{-2}$	15.09	$\leq -0.93 \pm 1.16$	5.0	12.0
	1	11.5	$0.19''\times0.17''$, 52.98°	$\leq 5.77\times10^{-2}$	16.52			
	2	8.5	$0.28''\times0.22''$, 87.50°	1.01	15.09	$-1.19 \pm 0.50^\star$		
	2	11.5	$0.19''\times0.17''$, 52.98°	0.72	16.52			
SDSS J135558.08+001530.6	1	8.5	$0.31''\times0.24''$, −44.09°	6.00×10^{-1}	17.92	-1.18 ± 0.53	3.1	8.2
	1	11.5	$0.23''\times0.18''$, 45.19°	4.24×10^{-1}	20.80			
	2	8.5	$0.31''\times0.24''$, −44.09°	$\leq 1.30\times10^{-1}$	17.92	$\leq -0.97 \pm 1.07$		
	2	11.5	$0.23''\times0.18''$, 45.19°	$\leq 1.01\times10^{-1}$	20.80			
2MASX J16170895+2226279	1	6.0	$0.39''\times0.30''$, −72.25°	7.89×10^{-1}	12.78	-0.95 ± 0.10	4.3	5.6
	1	15.0	$0.59''\times0.39''$, −71.76°	3.29×10^{-1}	7.05			
	2	6.0	$0.39''\times0.30''$, −72.25°	3.14×10^{-1}	12.78	-0.28 ± 0.14		
	2	15.0	$0.59''\times0.39''$, −71.76°	2.37×10^{-1}	7.05			

is α= −0.93±1.16. The companion (B) shows an extended jet structure and the two hot spots are detected. The total size of the jet is 1$''$ or 2.4 kpc. The hot spots are in the NE-SW direction. One of the hot spots is brighter than the other which can be due to Doppler boosting.

SDSS J135558.08+001530.6

J1355 (hereafter) is a galaxy pair but the galaxy morphologies are uncertain. There is a single SDSS spectrum associated to this system which is classified as a broadline AGN. We have detected two radio sources in the 8.5 and 11.5 GHz images (Figure 4.2) at a separation of ∼3.1$''$ or 8.06 kpc. Both the cores (A, B) are compact and the spectral index values are steep (∼-1.0).

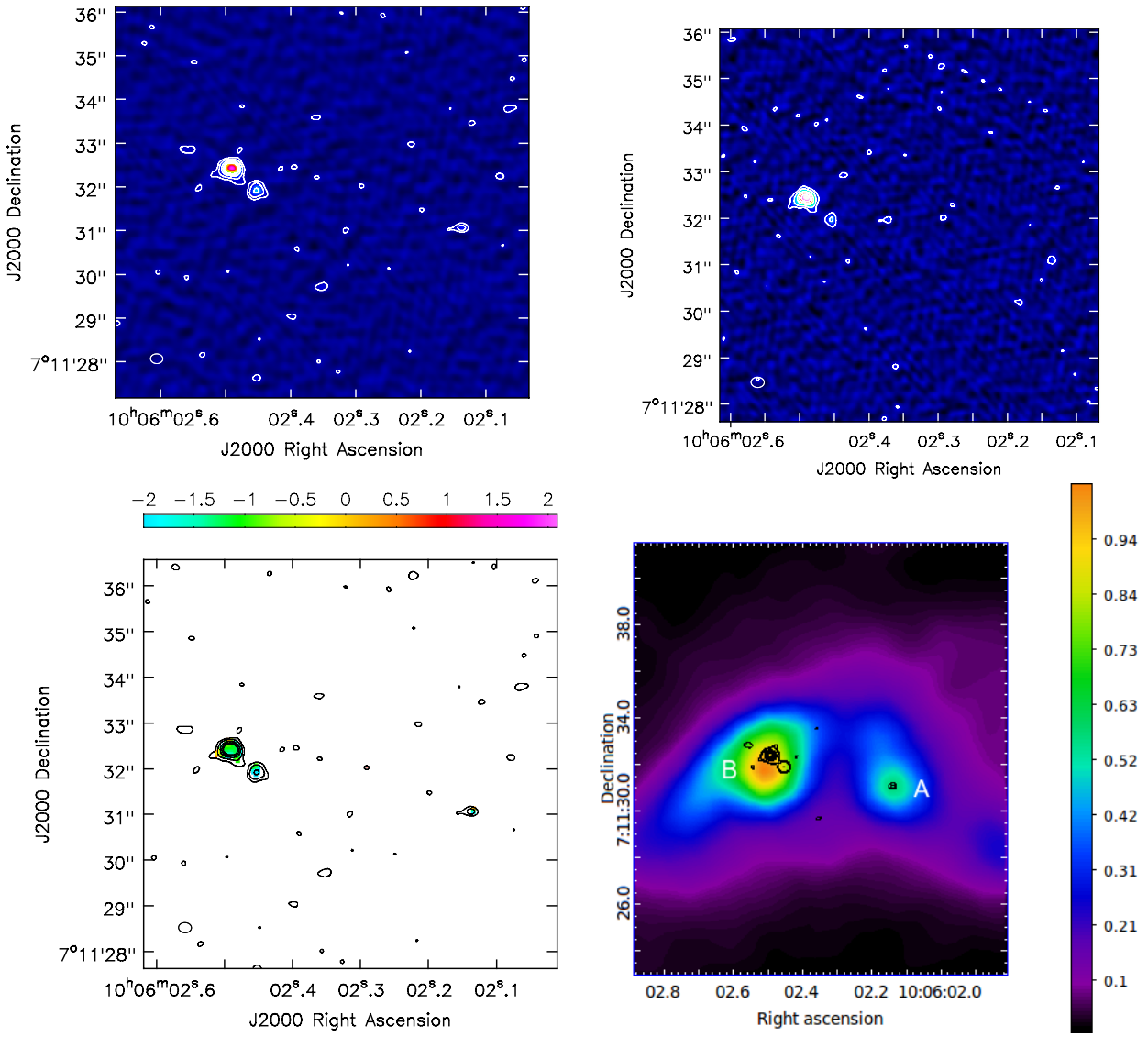

FIGURE 4.1: The dual radio core galaxy J1006. Moving from top left to right and bottom left to right : (i) the radio image at 8.5 GHz, (ii) the radio image at 11.5 GHz, (iii) the spectral index map using 8.5 GHz and 11.5 GHz images and (iv) the 8.5 GHz contours superimposed on the SDSS g band image of the galaxy. This is a confirmed DAGN at the separation of 12 kpc. The contour levels are 10%, 20%, 40%, 60% and 80% of the peak intensities (table 4.4).

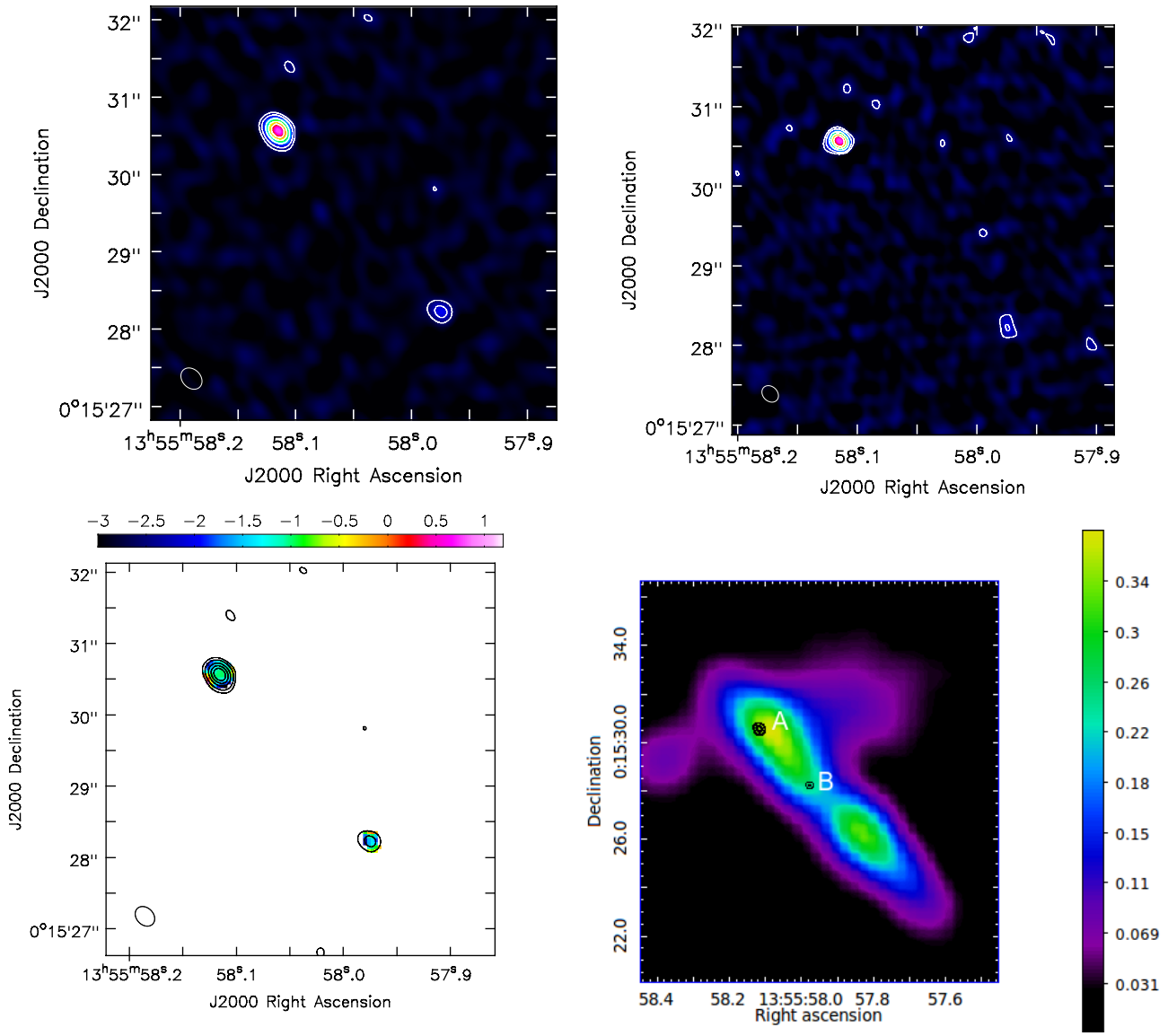

FIGURE 4.2: The dual radio core galaxy J1355. Moving from top left to right and bottom left to right: (i) the radio image at 8.5 GHz, (ii) the radio image at 11.5 GHz, (iii) the spectral index map using 8.5 GHz and 11.5 GHz images and (iv) the 8.5 GHz contours superimposed on the SDSS g band image of the galaxy. The contour levels are 10%, 20%, 40%, 60% and 80% of the peak intensities (table 4.4).

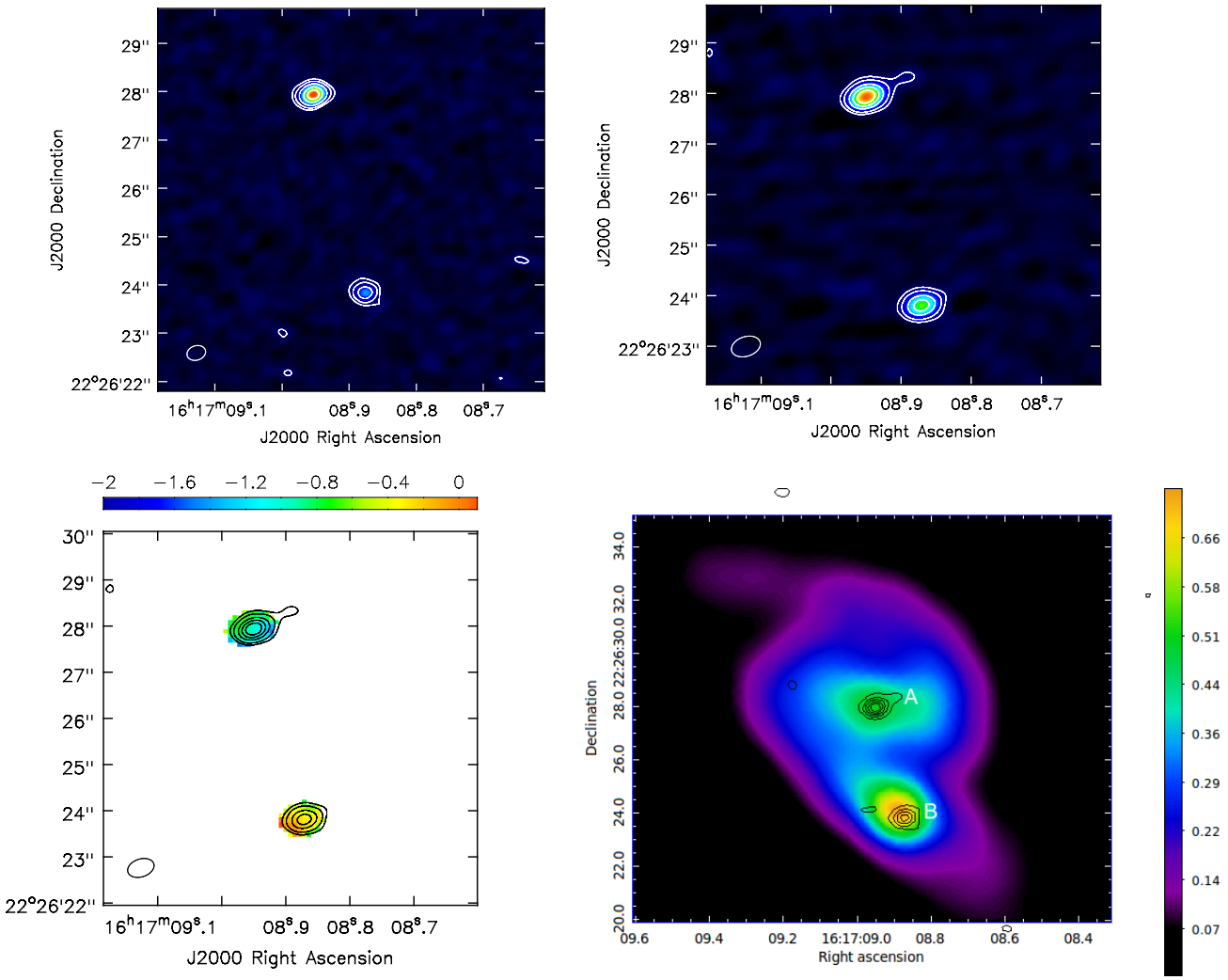

FIGURE 4.3: The dual radio core galaxy J1617. Moving from top left to right and bottom left to right: (i) the radio image at 6.0 GHz, (ii) the radio image at 15.0 GHz, (iii) the spectral index map using 6.0 GHz and 15.0 GHz images and (iv) the 15.0 GHz contours superimposed on the SDSS g band image of the galaxy. This can be DAGN or AGN+SF nuclei pair at the separation of 5.6 kpc. The contour levels are 10%, 20%, 40%, 60% and 80% of the peak intensities (table 4.4).

TABLE 4.5: **Radio properties of sample galaxies from FIRST (1.4 GHz) map:** Column 1: SDSS name of the galaxy; Column 2: Integrated flux density (S_{int}) of the FIRST image in Jy unit; Column 3: Peak intensity (S_{peak}) of the FIRST image in Jy/beam; Column 4: The ratio of the integrated flux density to the peak intensity (θ)=(S_{int}/S_{peak})$^{1/2}$.

Name	FIRST integrated flux density (Jy)	FIRST peak intensity (Jy beam^{-1})	θ =(S_{int}/S_{peak})$^{1/2}$
2MASXJ09120164+5320369	0.13	0.12	1.04
UGC 05353	3.15×10^{-3}	3.14×10^{-3}	1.00
SDSS J100602.13+071130.9	7.80×10^{-3}	6.46×10^{-3}	1.09
SDSS J110215.68+290725.2	Core-jet	–	–
SDSS J132318.81+030807.1	Core-jet	–	–
2MASX J13245059+1758152	1.41×10^{-2}	1.38×10^{-2}	1.01
2MASX J13490964+0404487	6.28×10^{-2}	5.96×10^{-2}	1.02
SDSS J135558.08+001530.6	4.64×10^{-3}	3.88×10^{-3}	1.09
2MASX J14131625+2119374	2.49×10^{-3}	2.19×10^{-3}	1.06
2MASX J14203147+4008166	7.07×10^{-3}	6.57×10^{-3}	1.03
2MASXJ14454130+3341080	4.21×10^{-3}	3.87×10^{-3}	1.04
2MASX J15001769+1051100	8.88×10^{-3}	2.56×10^{-3}	1.86
B31459+399NED01	4.56×10^{-2}	4.26×10^{-2}	1.03
2MASX J15042218+4741116	9.45×10^{-3}	5.88×10^{-3}	1.26
SDSS J160027+083742	hotspot	–	–
2MASX J16170895+2226279	4.21×10^{-3}	2.81×10^{-3}	1.22
2MASX J16441390+2528286	7.94×10^{-3}	7.56×10^{-3}	1.02
2MASX J23044283-0933454	8.78×10^{-3}	8.66×10^{-3}	1.00
SDSS J233604.04+000447.1	1.60×10^{-2}	1.38×10^{-2}	1.07

2MASX J16170895+2226279

J1617 (hereafter) is a spiral galaxy with a companion at 4.3″ (5.6 kpc) separation. Both galaxies have SDSS spectra. The J1617 spectrum has double-peaked emission lines but the companion does not have double-peaked emission lines. The optical image shows a common envelope in all bands and hence, this may be a minor merger. We have detected two cores at 6 GHz as well as at 15 GHz which coincide with the optical cores (Figure 4.3). The separation of the cores are 4.3″ or 5.6 kpc. The primary core (A) has a spectral index value of $\alpha = -0.95 \pm 0.10$. This

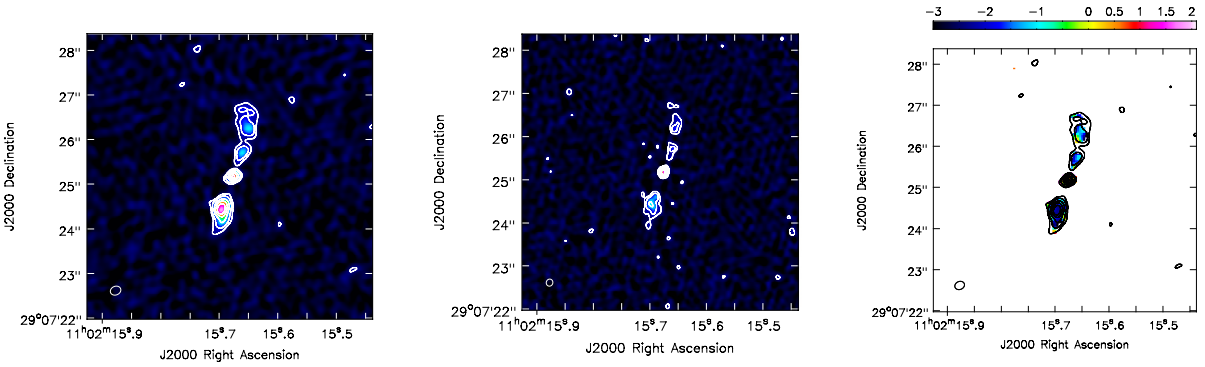

FIGURE 4.4: The radio images and the spectral index map of J1102. Moving left to right is the 8.5 GHz image, 11.5 GHz image and spectral index map using 8.5 GHz and 11.5 GHz images. The images are overlaid with its contours and the spectral index map is overlaid with the 11.5 GHz radio image contours. The contour levels are 10%, 20%, 40%, 60% and 80% of its peak intensities respectively (table 4.3).

core has a one-sided jet in the 15 GHz image. The companion core (B) has a flat spectral index value $\alpha = -0.28 \pm 0.14$.

SDSS J110215.68+290725.2

J1102 (hereafter) is an elliptical galaxy with a bright bulge and broad AGN emission lines. It has a two sided jet extended in the north (N) - south (S) direction. The total size of the core-jet structure is $\sim 2.9''$ or 6.2 kpc in the 8.5 and 11.5 GHz images (Figure 4.4). The northern jet is composed of two blobs while the southern jet has a single blob. The southern blob is brighter than the northern one which can be due to Doppler boosting. However, the FIRST image of J1102 shows a large scale core-jet structure of size $\sim$ 120 kpc in the NE and SW directions (Figure 4.5). This change in direction from the small scale radio jet to the large scale one is a signature of an Z-shaped core-jet structure in this galaxy (see section 4.3.2). We overlaid the high-resolution radio image on the FIRST image (Figure 4.5). The spectral index map of the small scale radio structure shows that the core has a flat spectral index ($\alpha = 0.45 \pm 0.44$) and the jets have relatively steep indices ($\alpha < -1.81 \pm 0.46$). J1102 has been observed in several surveys in the

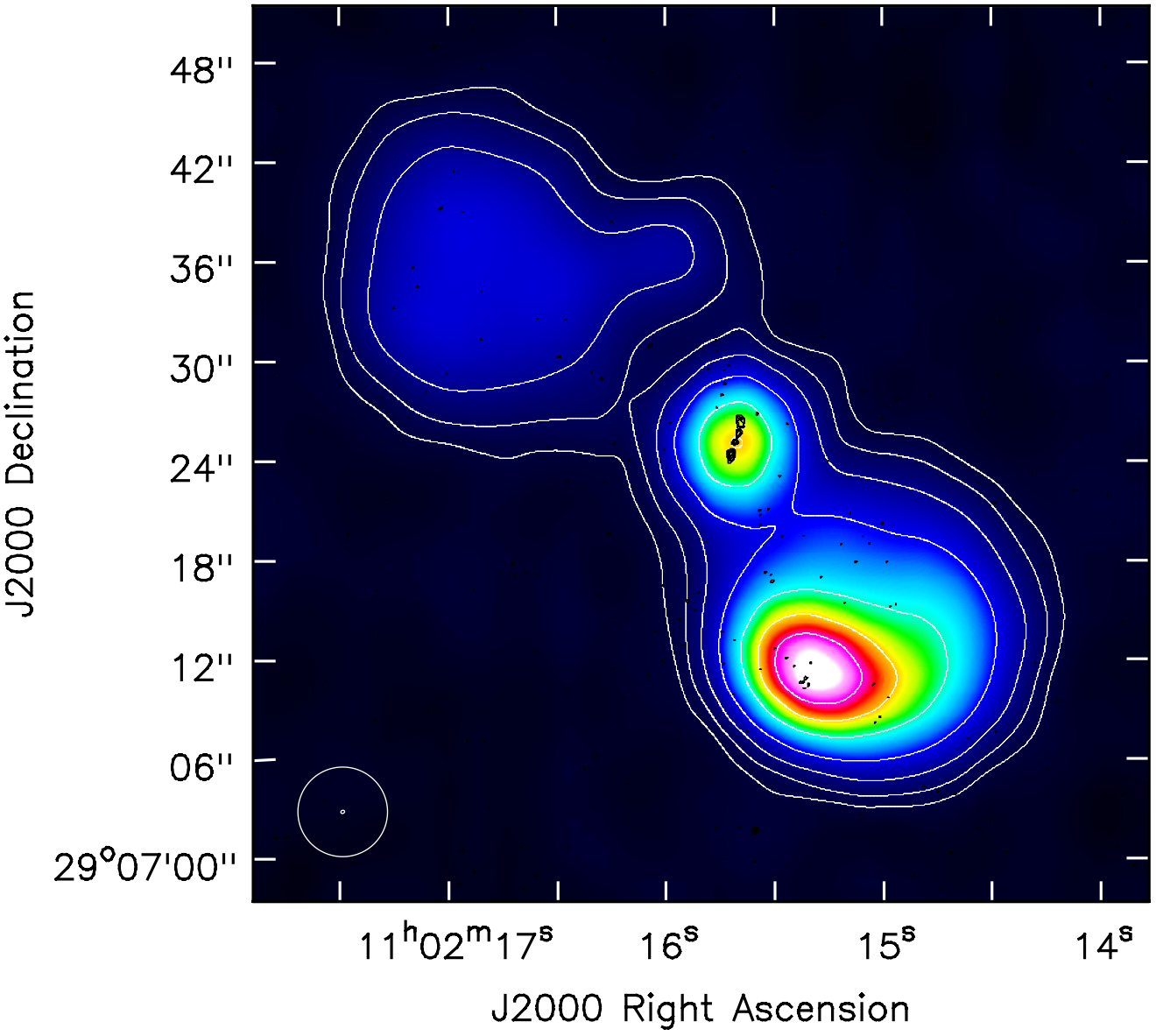

FIGURE 4.5: The FIRST image of 1102 with the 8.4 GHz contours overlaid in black. The FIRST image shows $\sim$ 120 kpc jet and the 8.5 GHz shows 6 kpc jet. There is a change in the jet directions from small scale to large scale. This can be an S- or Z-shaped source. The contour levels in FIRST image are 2.5%, 5%, 10%, 20%, 40%, 60% and 80% of its peak intensity respectively. The contour levels in 8.5 GHz image are 10%, 20%, 40%, 60% and 80% of its peak intensity respectively (table 4.3).

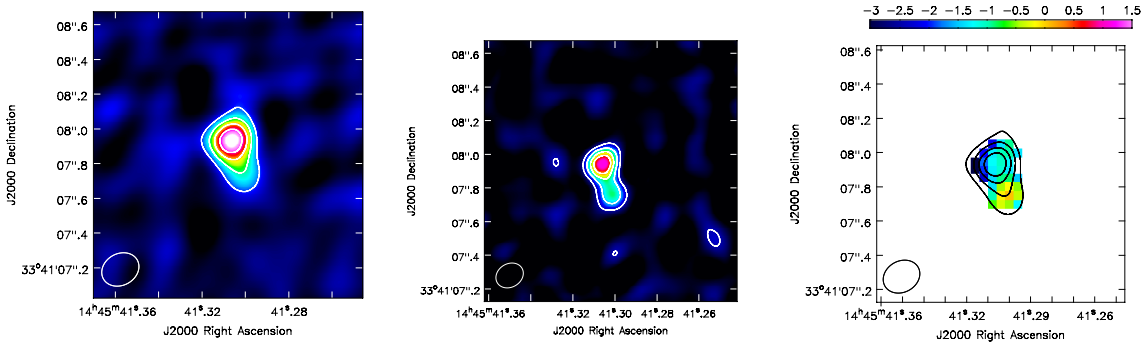

FIGURE 4.6: The radio images with contours and the spectral index map of J1445. Moving from left to right is the 8.5 GHz image, 11.5 GHz image and spectral index map using 8.5 GHz and 11.5 GHz images overlaid with the 11.5 GHz radio contours. The contour levels are 20%, 40%, 60% and 80% of its peak intensity respectively (table 4.3). J1445 shows an extended structure which can be core-jet or dual AGN.

frequency range 0.365 to 4.85 GHz (e.g. Becker, White & Edwards 1991; Douglas et al. 1996; White & Becker 1992).

2MASX J14454130+3341080

J1445 (hereafter) is a QSO. J1445 shows a one-sided, small, extended structure at 8.5 GHz and 11.5 GHz (Figure 4.6). It contains a bright region with extended radio emission. The bright region has steep spectral index ($\alpha = -1.57 \pm 0.58$) and the extended region has $\alpha = -0.79 \pm 0.74$. The size of the radio emission is $\sim 0.44''$ or 1.14 kpc. We have found a radio core in the FIRST image along with an extended low radio emission ($\sim 4\sigma$) in the southwest direction. We are not sure whether this extended emission is a jet associated with the radio core or not. So, we have calculated the θ_{FIRST} which is ≈ 1.00. This implies that most of the radio emission is concentrated at the center (~ 10 kpc). Here, the extended radio emission at 8.5 and 11.5 GHz can be a core-jet structure or dual AGN (see section 4.3.2).

We now discuss the remaining 14 sources (Table 4.3). The targets J1324 and J1349 have single frequency observations at 6 GHz. They both have compact cores. From their FIRST and NVSS images, we find that they have similar flux densities at 1.4 GHz, which indicates that they are both compact sources.

We have not been able to detect the source J1500 at any of the observed frequencies (8.5 and 11.5 GHz). However, we have obtained the upper limits to the flux densities by taking 3 times the rms noise at 8.5 and 11.5 GHz (Table 5). We have made a ball park estimate of the spectral index by using these flux densities. The calculated value is +0.44 which represents a radio source with an inverted spectral index. The VLA FIRST image shows an extended radio core. It has θ_{FIRST}= 1.66 which also supports an extended jet emission. The SDSS spectrum indicates that it is an AGN. Hence, we can say that this is an AGN with low radio power which is not detected at the observed sensitivity.

We have detected flat spectral indices (Table 4.3) in six galaxies (J0912, J1413, J1420, J1504, J1600, J1644); indicative of compact AGN emission. However, in a recent VLBA study, Liu et al. (2018) have found that J0912 has a three component core jet structure on sub-arcsecond scales. There is an unresolved radio source at 30″ to the southeast of the J0912 in the FIRST image. This is the radio counterpart of the optical source SDSS J091204.83+ 532018.5 and its optical counterpart is very faint. We have detected an extended radio source with size of 0.75″ at the same position at 8.5 and 11.5 GHz (Figure 4.7). The bright core has a spectral index of $\alpha = -1.3 \pm 0.08$. The spectral index values increase towards the edges. The northeast region has $\alpha = -1.66 \pm 0.2$ and the southwest region has $\alpha = -1.46 \pm 0.4$. This suggests that this could be a kpc core-jet radio source (Figure 4.7). J1413 shows a large, two sided jet of size 275″ or ∼935 kpc in the NVSS image. J1504 has a jet of size 45 kpc in the FIRST image. The NVSS map of J1600 shows a jet of size 1 Mpc (Figure 4.8). The large size of this source suggests it to be a giant radio galaxy. Deeper uGMRT observations can help us

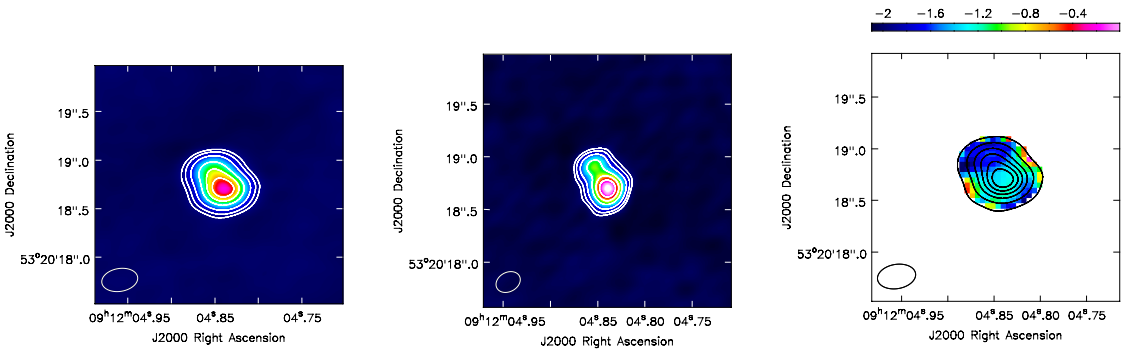

FIGURE 4.7: The images of SDSS J091204.83+ 532018.5, situated 30″ away from our target source J0912. Moving left to right is the 8.5 GHz image, 11.5 GHz image and spectral index map using 8.5 GHz and 11.5 GHz images. The contour level are 10%, 20%, 40%, 60% and 80% of its peak intensities respectively. We have resolved the extended radio structure in this object.

to understand the large scale morphology of the radio jets. J1420 and J1644 show compact cores in our observations and $\theta_{FIRST} \sim 1.0$ which is also consistent with compact emission.

The remaining 5 sources have single steep-spectrum cores (UGC 05353, J1323, J1501, J2304 and J2336). UGC 05353, J1501 and J2336 do not have any extended jet emission in their FIRST or NVSS images. The calculated $\theta_{FIRST} < 1.06$ for UGC 05353 and J1501 also supports the lack of extended emission. However, the steep spectral index indicates that the optically-thin jet emission may be dominant in the cores. J2336 has $\theta_{FIRST} = 1.08$. Here again we cannot rule out the presence of extended jet emission inside the detected core. The source J1323 has a core with steep spectral index value ($\alpha = -1.50 \pm 0.78$). It has extended radio emission in its NVSS image and its FIRST image shows a two sided large-scale jet with a total size of 550 kpc. We have detected a core and some radio emission in small blobs at the separation of $\sim 8''$ (40 kpc) in the 8.5 and 11.5 GHz images of J1323. The source J2304 has a single core at the observed frequency (6, 8.5 and 11.5 GHz). Gabányi et al. (2016) have observed this source with the Very Long Baseline Array (VLBA) at 1.5 GHz where they have detected a core-jet structure in the same direction as the 11.5 GHz image.

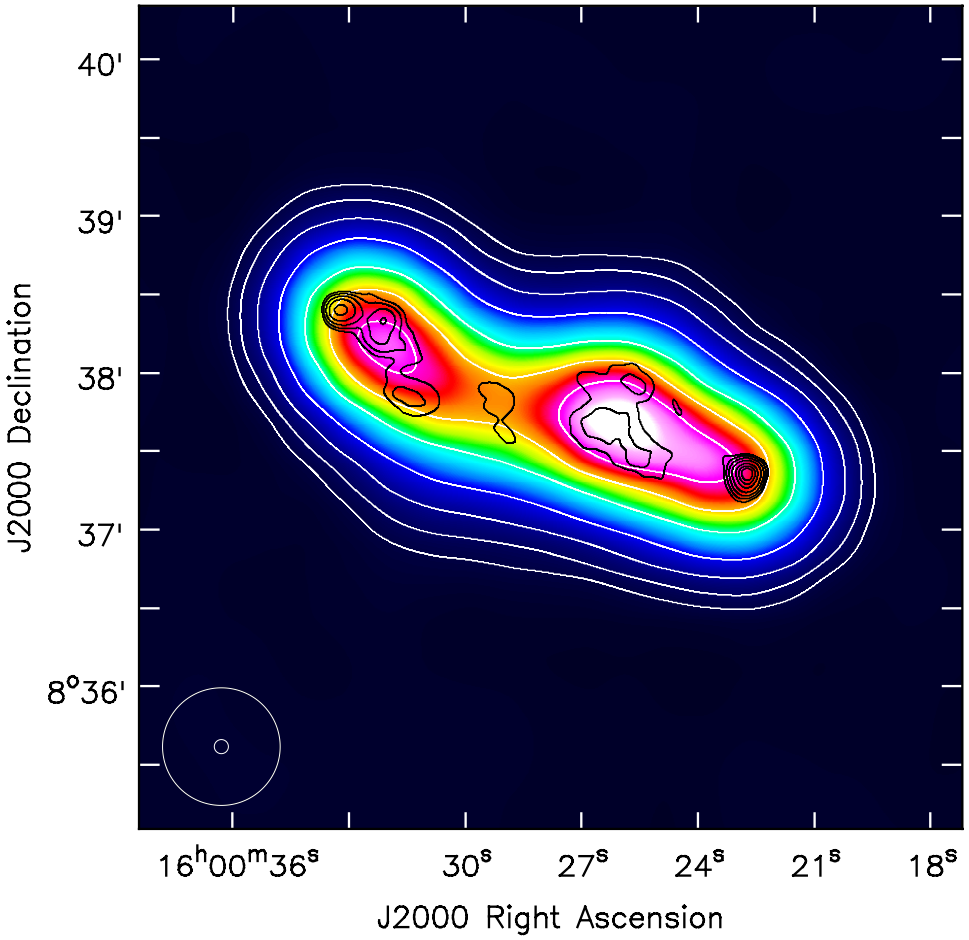

FIGURE 4.8: The NVSS image of J1600 with the FIRST image contours overlaid in black. The NVSS jets have a size of 1 Mpc. This size suggests it to be giant radio galaxy (GRG). Deep GMRT image is needed to explore this galaxy.

TABLE 4.6: **Mass of the BH (M_{BH}), Eddington ratio (λ) and Star-formation rate (SFR) calculations:** Column 1: The name of the galaxies; Column 2: SMBH mass in $M_\odot$ units using the M-σ_* relation where σ is taken from Column 9, Table 3.2; Column 3: The [O III] luminosity in erg s^{-1} units; Column 4: the bolometric luminosity in erg s^{-1} units; Column 5: The Eddington luminosity in erg s^{-1} units calculated using M_{BH} (Column 2); Column 6: The Eddington ratio; Column 7: Hα luminosity ($L_{H\alpha}$) in erg s^{-1} units; Column 8: Radio luminosity in W Hz^{-1} units; Column 9: The star formation rate ($SFR_{H\alpha}$) in $M_\odot$ yr^{-1} using Hα flux from SDSS spectra; Column 10: The star formation rate (SFR_{Radio}) in $M_\odot$ yr^{-1} using radio luminosity at 1.4 GHz from NVSS survey;

Name	M_{BH} ($M_\odot$)	$L_{O[III]}$ (erg s^{-1})	L_{Bol} (erg s^{-1})	L_{Edd} (erg s^{-1})	$\lambda = L_{Bol}/L_{Edd}$	$L_{H\alpha}$ (erg s^{-1})	L_{Radio} (W Hz^{-1})	$SFR_{H\alpha}$ ($M_\odot$ yr^{-1})	SFR_{Radio} ($M_\odot$ yr^{-1})
2MASX J09120164+5320369	$(2.65 \pm 0.68)\times10^{8}$	$(6.30 \pm 0.63)\times10^{40}$	$(2.20 \pm 0.22)\times10^{44}$	$(3.18 \pm 0.82)\times10^{46}$	$(0.06 \pm 0.01)\times10^{-1}$	$(5.65 \pm 0.30)\times10^{40}$	$(4.19 \pm 0.01)\times10^{24}$	0.44 ± 0.02	310.67 ± 3.16
UGC 05353	$(2.33 \pm 0.26)\times10^{9}$	$(1.02 \pm 0.25)\times10^{39}$	$(3.60 \pm 0.88)\times10^{42}$	$(2.80 \pm 0.31)\times10^{47}$	$(1.28 \pm 0.34)\times10^{-5}$	$(1.63 \pm 0.31)\times10^{40}$	$(1.82 \pm 0.47)\times10^{21}$	0.12 ± 0.02	0.13 ± 0.11
SDSS J100602.13+071130.9	$(7.40 \pm 3.73)\times10^{7}$	$(2.69 \pm 0.03)\times10^{41}$	$(9.41 \pm 0.13)\times10^{44}$	$(8.88 \pm 4.48)\times10^{45}$	(0.10 ± 0.05)	$(4.83 \pm 0.03)\times10^{41}$	—	3.81 ± 0.03	—
SDSS J110215.68+290725.2	$(3.15 \pm 0.66)\times10^{8}$	$(1.29 \pm 0.05)\times10^{41}$	$(4.51 \pm 0.18)\times10^{44}$	$(3.78 \pm 0.79)\times10^{46}$	$(0.11 \pm 0.02)\times10^{-1}$	$(1.01 \pm 0.04)\times10^{41}$	—	0.79 ± 0.03	—
SDSS J132318.81+030807.1	$(3.03 \pm 1.69)\times10^{8}$	$(1.56 \pm 0.02)\times10^{42}$	$(5.48 \pm 0.09)\times10^{45}$	$(3.64 \pm 2.02)\times10^{46}$	(0.15 ± 0.08)	$(6.31 \pm 0.18)\times10^{41}$	—	4.98 ± 0.14	—-
2MASX J13245059+1758152	$(5.03 \pm 1.97)\times10^{6}$	$(1.43 \pm 0.10)\times10^{40}$	$(5.03 \pm 0.37)\times10^{43}$	$(6.03 \pm 2.37)\times10^{44}$	(0.08 ± 0.03)	$(9.06 \pm 0.54)\times10^{40}$	$(2.33 \pm 0.07)\times10^{23}$	0.71 ± 0.04	17.24 ± 1.81
2MASX J13490964+0404487	$(2.48 \pm 0.42)\times10^{8}$	$(1.50 \pm 0.32)\times10^{40}$	$(5.25 \pm 1.12)\times10^{43}$	$(2.98 \pm 0.51)\times10^{46}$	$(0.17 \pm 0.04)\times10^{-2}$	$(2.19 \pm 0.27)\times10^{40}$	$(9.32 \pm 0.07)\times10^{23}$	0.17 ± 0.02	69.03 ± 1.79
SDSS J135558.08+001530.6	$(1.53 \pm 1.05)\times10^{9}$	$(2.98 \pm 0.23)\times10^{40}$	$(1.04 \pm 0.08)\times10^{44}$	$(1.84 \pm 1.27)\times10^{47}$	$(0.05 \pm 0.03)\times10^{-2}$	$(1.02 \pm 0.08)\times10^{41}$	—	0.80 ± 0.06	—
2MASX J14131625+2119374	$(5.45 \pm 1.66)\times10^{8}$	$(9.89 \pm 0.94)\times10^{40}$	$(3.46 \pm 0.32)\times10^{44}$	$(6.54 \pm 1.99)\times10^{46}$	$(0.05 \pm 0.01)\times10^{-1}$	$(6.49 \pm 0.66)\times10^{40}$	—	0.51 ± 0.05	—
2MASX J14203147+4008166	$(4.94 \pm 1.87)\times10^{8}$	$(6.26 \pm 1.12)\times10^{40}$	$(2.19 \pm 0.39)\times10^{44}$	$(5.93 \pm 2.25)\times10^{46}$	$(0.03 \pm 0.01)\times10^{-1}$	$(6.89 \pm 1.34)\times10^{40}$	$(1.66 \pm 0.05)\times10^{23}$	0.54 ± 0.10	122.68 ± 13.85
2MASX J14454130+3341080	$(8.92 \pm 3.48)\times10^{7}$	$(7.64 \pm 0.39)\times10^{41}$	$(2.67 \pm 0.13)\times10^{45}$	$(1.07 \pm 0.41)\times10^{46}$	(0.24± 0.09)	$(4.24 \pm 0.12)\times10^{41}$	$(1.85 \pm 0.17)\times10^{23}$	3.35 ± 0.09	13.71 ± 4.34
2MASX J15001769+1051100	$(2.08 \pm 0.58)\times10^{8}$	$(3.67 \pm 0.76)\times10^{40}$	$(1.28 \pm 0.26)\times10^{44}$	$(2.50 \pm 0.69)\times10^{46}$	$(0.05 \pm 0.01)\times10^{-1}$	$(1.19 \pm 0.16)\times10^{41}$	$(7.87 \pm 0.35)\times10^{23}$	0.93 ± 0.12	58.27 ± 8.79
B31459+399NED01	$(6.75 \pm 5.35)\times10^{7}$	$(1.93 \pm 0.19)\times10^{41}$	$(6.76 \pm 0.67)\times10^{44}$	$(8.10 \pm 6.42)\times10^{45}$	$(0.83 \pm 0.66)\times10^{-1}$	$(9.76 \pm 6.63)\times10^{40}$	$(1.81 \pm 0.02)\times10^{25}$	0.77 ± 0.52	1339.18 ± 70.21
2MASX J15042218+4741116	$(6.52 \pm 2.89)\times10^{7}$	$(5.10 \pm 0.73)\times10^{39}$	$(1.78 \pm 0.27)\times10^{43}$	$(7.82 \pm 3.47)\times10^{45}$	$(0.02 \pm 0.01)\times10^{-1}$	$(3.25 \pm 0.50)\times10^{40}$	$(2.18 \pm 0.07)\times10^{23}$	0.25 ± 0.04	16.18 ± 1.75
SDSS J160027.78+083743.0	$(2.87 \pm 1.01)\times10^{8}$	$(3.74 \pm 0.09)\times10^{41}$	$(1.30 \pm 0.03)\times10^{45}$	$(3.44 \pm 1.22)\times10^{46}$	(0.03 ± 0.01)	$(2.11 \pm 0.08)\times10^{41}$	—	1.67 ± 0.06	—
2MASX J16170895+2226279	$(2.24 \pm 1.03)\times10^{7}$	$(7.54 \pm 0.24)\times10^{40}$	$(2.64 \pm 0.08)\times10^{44}$	$(2.69 \pm 1.24)\times10^{45}$	(0.09 ± 0.04)	$(5.38 \pm 0.17)\times10^{40}$	$(2.40 \pm 0.31)\times10^{22}$	0.42 ± 0.01	1.78 ± 0.77
2MASX J16441390+2528286	$(6.28 \pm 1.00)\times10^{8}$	$(1.13 \pm 0.15)\times10^{40}$	$(3.96 \pm 0.52)\times10^{43}$	$(7.53 \pm 1.20)\times10^{46}$	$(0.05 \pm 0.01)\times10^{-2}$	$(5.10 \pm 3.34)\times10^{39}$	$(5.92 \pm 0.31)\times10^{22}$	0.04 ± 0.02	4.38 ± 0.76
2MASX J23044283-0933454	$(2.68 \pm 0.42)\times10^{7}$	$(1.65 \pm 0.07)\times10^{40}$	$(5.78 \pm 0.27)\times10^{43}$	$(3.22 \pm 0.50)\times10^{45}$	$(0.17 \pm 0.02)\times10^{-1}$	$(1.75 \pm 0.05)\times10^{40}$	$(2.24 \pm 0.11)\times10^{22}$	0.13 ± 0.01	1.66 ± 0.27
2MASX J233604.04+000447	$(7.35 \pm 3.06)\times10^{7}$	$(3.81 \pm 0.10)\times10^{40}$	$(1.33 \pm 0.36)\times10^{44}$	$(8.82 \pm 3.63)\times10^{45}$	$(0.15 \pm 0.06)\times10^{-1}$	$(3.69 \pm 0.14)\times10^{40}$	$(2.46 \pm 0.06)\times10^{23}$	0.29 ± 0.01	18.20 ± 1.53

4.2.2 SMBH masses, Eddington ratios and Star Formation Rates

We have calculated the SMBH mass (M_{BH}) of all our sources. We have used the velocity dispersion (σ) of the underlying stellar component from Ge et al. (2012) and the M-$\sigma_\star$ relation from McConnell & Ma (2013). The SMBH values are given in (Table 4.6). The SMBH masses range from 10^6 to 10^9 $M_\odot$. We calculated the total flux density using the blue shifted and red shifted component of the [O III]λ5008 line from Ge et al. (2012). Using source distances from NED*, we obtained the [O III]λ5008 luminosities ($L_{[OIII]}$). We used Heckman et al. (2004) to calculate the bolometric luminosities (L_{Bol}) of the sources. Using the SMBH masses, we calculated the Eddington luminosities (L_{Edd}) and the Eddington ratios (λ_{Edd}) (Table 4.6).

$$L_{O[III]} = F_{[OIII]} \times 4\pi D^2; \quad L_{Bol} = L_{[OIII]} \times 3500$$

$$L_{Edd} = 1.25 \times 10^{38} M_{BH} M_\odot^{-1}; \quad \lambda_{Edd} = L_{Bol}/L_{Edd}$$

We have used the $H\alpha$ flux from the SDSS spectra to calculate the star formation rate (SFR). The $H\alpha$ emission can arise from star formation as well as from the AGN. Therefore, the SFR calculated from the total $H\alpha$ emission is an upper limit. We have followed the SFR relation from Kennicutt (1998a):

$$SFR_{H\alpha}(M_\odot yr^{-1}) = 7.9 \times 10^{42} L_{[H\alpha]}(ergs^{-1})$$

Supernovae (Type II and Ib) remnants (SNRs) can give rise to accelerated relativistic electrons which produce non-thermal synchrotron emission. Massive stars in H II regions also produce free-free thermal emission. This radio emission results in the radio and far-infrared (FIR) correlation observed for normal galaxies

*http://ned.ipac.caltech.edu/

(Condon 1992). However, AGN host galaxies are offset from this correlation due to a "radio excess". We have used the radio excess objects which are AGN from Yun, Reddy & Condon (2001) to obtain the expected AGN/SF fraction in radio flux density (see Table 2 in Yun, Reddy & Condon 2001). To do this, we have calculated the expected radio emission using the FIR (F60 μm) flux density in the fitted correlation. Then we subtracted the calculated radio flux density from their observed values and found the AGN/SF contribution. We have done this exercise for all the objects in that table (table 2; Yun, Reddy & Condon 2001). The AGN contribution in all the radio-loud objects is 99% while in Seyfert galaxies, it is 80 to 90%. Therefore, we have assumed the AGN contribution to have an upper limit of 70% and the star formation contribution to be 30%.

We have calculated the SFR using the radio flux density in the following relation (Condon 1992):

$$SFR_{Radio}(M_{\odot}yr^{-1}) = L(WHz^{-1})/5.3 \times 10^{21}\nu(GHz)^{\alpha}$$

We have used the radio flux density from the NVSS map at 1.4 GHz, assuming $\alpha = -0.8$ to calculate the SFR. Here, we have calculated the SFR_{Radio} only for objects which have a single radio core. The SFR for the objects which show large core-jet structures are not calculated. This is because the SFR_{Radio} would be much higher if the radio emission from the AGN jets are included.

We have plotted the M_{BH} vs $\mathrm{L}_{[OIII]}$, λ_{Edd} vs $\mathrm{L}_{[OIII]}$, $\mathrm{SFR}_{H\alpha}$ vs $\mathrm{L}_{[OIII]}$ as well as the SFR_{Radio} vs $\mathrm{L}_{[OIII]}$ in Figure 4.9 and calculated the Pearson correlation (R) with probability (P) for each pair of variables. We find that M_{BH} and $\mathrm{L}_{[OIII]}$ are not correlated and the correlation coefficient has a value R= -0.11, P= 0.64. We find that the λ_{Edd} follows the same trend as the single AGN control sample in Shangguan et al. (2016). The value ranges from 0.013×10^{-3} to 0.249. The λ_{Edd} values are correlated with $\mathrm{L}_{[OIII]}$, and has a value R= 0.79, P= 10^{-5}. The $\mathrm{SFR}_{H\alpha}$

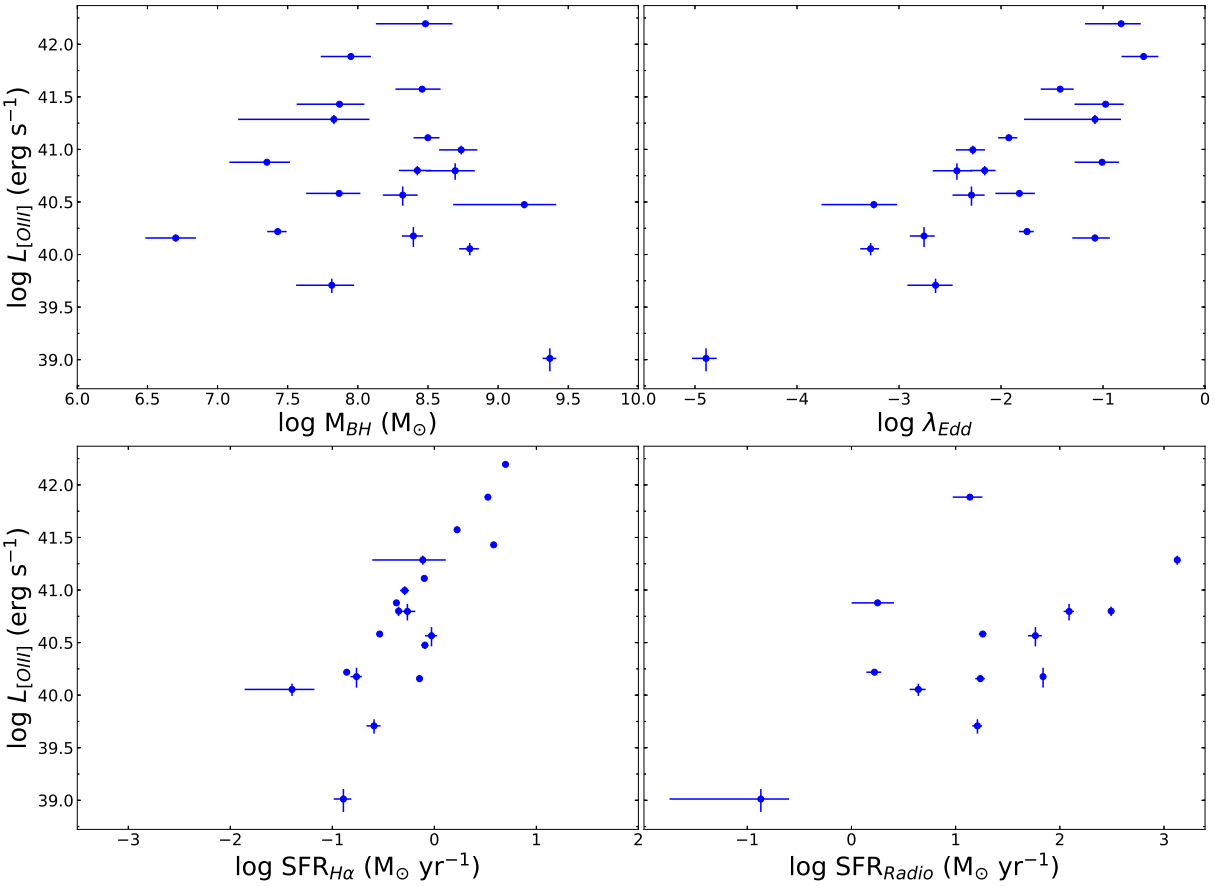

FIGURE 4.9: The top left panel shows M_{BH} vs $L_{[OIII]}$. There is no correlation between the plotted quantities. Top right panel shows the λ_{Edd} vs. $L_{[OIII]}$. Here λ_{Edd} falls in the range of single AGN λ_{Edd} and there is a strong positive correlation with $L_{[OIII]}$. The bottom left panel shows the $SFR_{H\alpha}$ vs $L_{[OIII]}$ which are also strongly correlated. The bottom right panel shows the SFR_{Radio} vs $L_{[OIII]}$. Errors have been plotted for all the quantities.

is correlated with $L_{[OIII]}$ and R= 0.82, P= 10^{-5}. Although λ_{Edd} is correlated with $L_{[OIII]}$, we know that λ_{Edd} depends on $L_{[OIII]}$ and hence also with L_{Bol}. Therefore, we cannot say that this is a real correlation. However, the $L_{[OIII]}$ and $SFR_{H\alpha}$ are independent parameters and hence this correlation is real. It may mean that star formation has been triggered by outflows or jet-ISM interaction (Dugan et al. 2014).

4.3 Discussion

We have detected dual radio cores in three of our sample double peaked emission line galaxies. In this section, we discuss the physical mechanisms that can explain both the nature of the optical spectra as well as the radio morphologies of the sources.

4.3.1 DAGN in J1006, J1355 and J1617

Observations of kpc scale DAGN can help us to constrain the theoretical merger models of galaxies (Van Wassenhove et al. 2012; Blecha, Loeb & Narayan 2013; Colpi 2014). Fu et al. (2015a) have searched for kpc scale DAGN using a high resolution, 1.4 GHz VLA survey of the ∼92 deg2 SDSS Stripe 82 field. They confirmed 4 DAGN in merger systems using both SDSS spectra and VLA observations (Fu et al. 2015b). Satyapal et al. (2017) used a mid-IR pre-selection method to identify the DAGN candidates in merger systems where the AGN are obscured by the presence of heavy dust obscuration. Since radio waves are not obscured by dust, high resolution radio observations have helped to reveal many DAGN (Müller-Sánchez et al. 2015a; Fu et al. 2015a). However, the radio emission can be due to nuclear star-burst as well as AGN activity. Hence, along with the detection of two cores in radio images, the spectral index values of the individual cores are needed to confirm the origin of the radio emission. Müller-Sánchez et al. (2015a) have detected three DAGN with VLA observations where they have found that the spectral indices of the cores are flat which is expected from AGN. On the other hand, Fu et al. (2015b) have found that the spectral indices of the confirmed DAGN compact cores are steep. The steep spectral index found in compact steep spectrum (CSS) sources indicates that they are very young sources and probably have small scale jets.

The optical spectroscopy of the individual cores can also support the AGN scenario. The BPT diagram is one of the key tools to confirm or distinguish between the AGN or star-forming nature of the nuclei. The line ratios are used in the diagram to distinguish between the AGN and star-burst nuclei (Baldwin, Phillips & Terlevich 1981b). However, in many cases, it is found that the emission lines are obscured by dust. In such cases, the AGN can be detected with a mid-infrared color selection method using the *Wide-Field Infrared Survey Explorer (WISE)*[†] data which gives a higher detection rate compared to optical methods (Satyapal et al. 2014). In our study, we have used the spectral index values as well as the SDSS optical spectra (when available) to determine the nature of the dual cores in our sample galaxies. We have identified two cores in our images that we refer to as the primary core or core A, which is generally identified with the optical position of the larger galaxy and the secondary core or core B which is usually associated with the companion galaxy.

Figure 4.1 shows the 8.5 and 11.5 GHz images of J1006 which has two radio sources at a separation of $\sim 5''$ or 12 kpc. As mentioned earlier, it is a merger system and both the sources are aligned with the optical cores (Figure 4.1). Source B shows a two sided jet with lobes/hot spots. The spectral index values of the lobes are steep ($\alpha = -1.3 \pm 0.4$ and -1.8 ± 0.9). Such spectral index values are expected from radio jets. We have calculated the line ratios, plotted them on the BPT diagram and found that it lies in the AGN region. Therefore, the radio images and optical spectra together confirm that source B is an AGN. The source A has $\alpha \leq -0.93 \pm 1.16$ and has a diameter of $0.37''$ (0.72 kpc). The calculated radio power ($\log P_{1.4}$) is $\sim$22 W Hz^{-1} which is much lower than the expected radio power of young AGN ($\log P_{1.4} \geq 25$ W Hz^{-1}) (O'Dea 1998; An & Baan 2012). However, the optical emission line ratios in the BPT diagram support the AGN nature of this radio source (Ge et al. 2012). Source A is therefore a low radio power AGN. Thus, J1006 is a DAGN with an AGN separation of 12 kpc.

[†]http://irsa.ipac.caltech.edu/Missions/wise.html

J1355 (Figure 4.2) is another galaxy merger where three optical nuclei can be clearly distinguished in the SDSS image of the galaxy. The optical sources are SDSS J135558.08+001530.6 (z= 0.134149), 2dFGRS N338Z121 (z= 0.1334) and SDSSCG 119 (z=0.1333). The separation of these sources from the main galaxy are 1.05″ and 5.87″. In our radio images, we have detected the main radio source at the position of SDSS J135558.08+001530.6 and the second radio source at a separation of 3.2″. However, it does not coincide with the other optical nuclei. Here we identify J1355, the radio source that coincides with an optical nuclei, as source A and the second radio core as source B. The spectral index value of source A is -1.18 ± 0.53. The source is compact with a size of 0.4″. We have calculated the [O III]/Hβ and [N II]/Hα and put them in the BPT diagram. It lies in the AGN region. So, from both the radio and optical data, we confirm that source A is an AGN. The spectral index of source B is -0.97 ± 1.07. The size of the source is ∼1 kpc. This can be an AGN or a star-forming nucleus. The calculated radio power (log $P_{1.4}$) is ∼23 W Hz^{-1}. However, there is no optical source at the position of the radio source B. Hence, we cannot confirm the actual position of the source. It can be a background or foreground object. Without an optical spectrum of source B, we cannot rule out any of these origins. Hence, J1355 is a merger system containing either a DAGN or a AGN-SF nuclei pair at a separation of 3.1″ or 8.20 kpc provided the second radio source is at the same redshift as the first source.

We have detected dual sources in J1617 at 6 GHz and 15 GHz (Figure 4.3) at a separation of 4.3″ or 5.6 kpc. This appears to be a minor merger. Here, we identify the main galaxy as source A and the accreting system as source B. The SDSS spectrum of source A shows double peaked emission lines with an AGN broad-line classification. We have made the spectral index image of source A which has an average α value of -0.95 ± 0.10. We have detected a one-sided jet of size 1″ or 1.3 kpc. The steep spectral index value is consistent with jet emission. Therefore, we conclude that source A is a confirmed AGN. Source B has narrow emission

lines in its SDSS spectrum and has a star-burst classification. The spectral index value of source B is -0.28 ± 0.14, which is relatively flat and consistent with an AGN. It is possible that the second SMBH is present but is dust obscured in the optical image. The calculated radio power ($\log P_{1.4}$) is $\sim$22 W Hz^{-1} which is much lower than the expected AGN power (An & Baan 2012). Hence, we cannot rule out a star-forming nucleus with the present data. In previous studies of DAGN, SDSS J171544.05+600835.7 is an example of a system where in optical images only one nucleus is seen but with the help of spectroscopy and X-ray observations, this second nucleus has been found to host a DAGN and the AGN emission is obscured by dust (Comerford et al. 2011). Koss et al. (2016) have similarly discovered an obscured dual AGN in J2028.5+2543 using *Swift*, where both nuclei are heavily obscured to Compton-thick levels. Hence, to confirm the presence of a DAGN in J1355 and J1617, hard X-ray band observations are required.

4.3.2 Are J0192, J1445, J1102 dual AGN?

2MASX J09120164+5320369

The SDSS image shows that J0912 has 3 optical cores where the secondary cores are at the separations of 2″ and 5″ from the primary core (A, B, C in Figure 4.10). We have detected a single radio core in our 8.5 and 11.5 GHz images that coincide with the primary core (A) in the optical image. There is Chandra archival data for this galaxy. We found two X-ray cores in the Chandra image (Figure 4.10). One of the Chandra cores coincides with the radio core associated with the primary optical core (A). The second Chandra core coincides with a secondary optical core (C) at a separation of 5″ or 10.165 kpc. The Chandra fluxes are $6. \times 10^{-15}$ and 3.96×10^{-14} erg cm^{-2} s^{-1} respectively for the primary and secondary cores (Evans et al. 2010). The redshift of this secondary core is not available from NED or SDSS

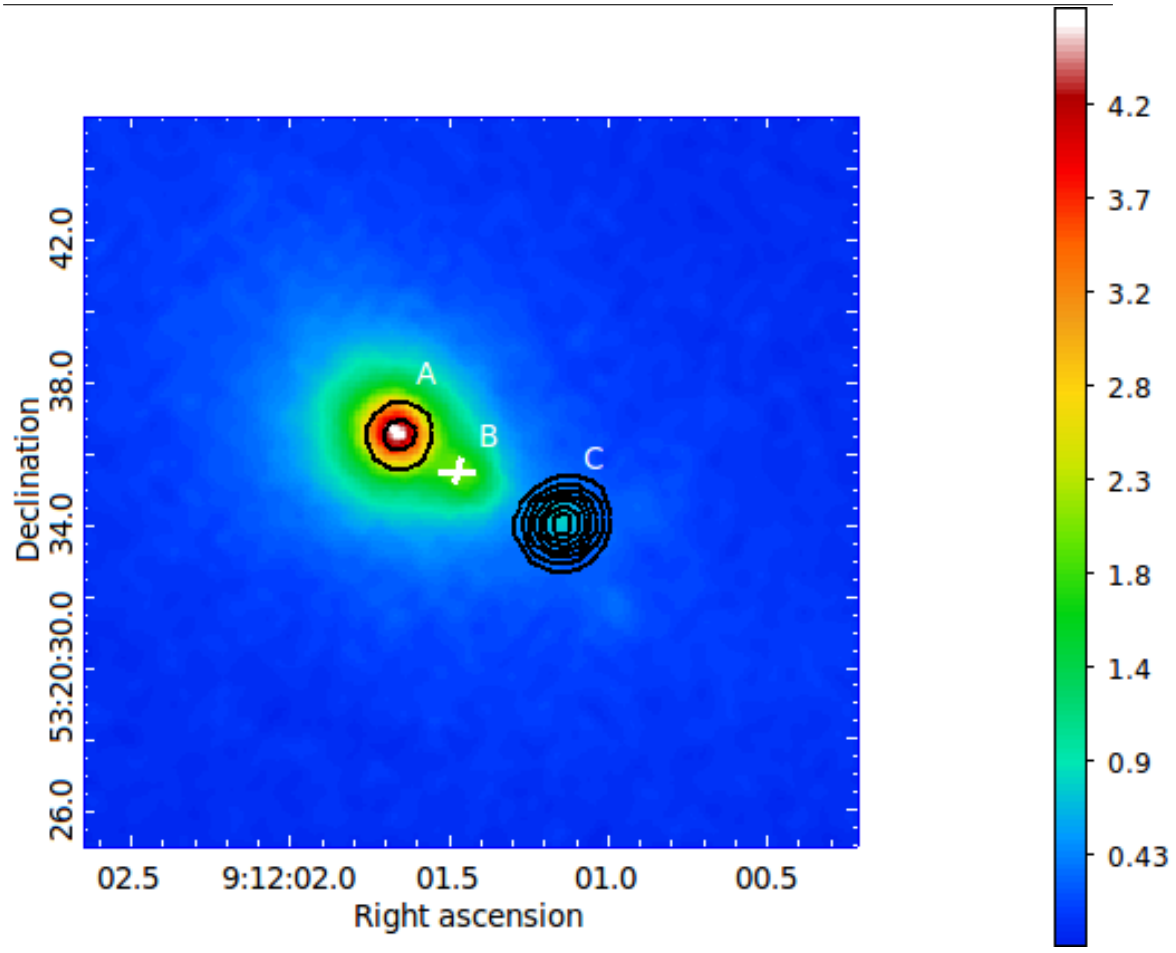

FIGURE 4.10: The optical g-band image of J0912 with the Chandra 0.7-3 keV X-ray image contours overlaid in black. The contour levels are 14%, 28%, 42%, 57%, 71% and 85% of the peak X-ray intensity. The optical image of J0912 shows three cores (A, B, C) but we detected only one core (A) in our radio observations. In the Chandra image, two cores (A and C) are detected at a separation of 10 kpc.

and we have not been able to find any spectra from this core in the literature. If the secondary X-ray source is at the same redshift, then J0912 could be a DAGN at nuclear separations of $\sim$ 10 kpc.

SDSS J110215.68+290725.2

The 11.5 GHz radio image shows a core-jet structure of 2.8″ or 5.9 kpc for this source. Both sides of the jets are aligned. However, we have found that the FIRST

(1.4 GHz) image shows a large scale core-jet structure of size $\sim 60''$ or $\sim$120 kpc. The large scale jets have a Z-shaped structure (Figure 4.5). There are many radio galaxies which show misaligned jets (Hutchings, Price & Gower 1988; Roberts et al. 2018). Sometimes these misaligned jets have S, Z or X- shapes. The X-shaped sources in the literature (Cheung & Springmann 2007) have been explained by (i) the spin-flip model (Natarajan & Pringle 1998b) or (ii) the backflow model (Leahy & Williams 1984b). However, the S-shaped morphology is difficult to explain with these models. The S- or Z- shaped morphologies are better explained as helical or precessing jets (Begelman, Blandford & Rees 1980b). NGC 326 is a good example of a Z-shaped radio source (Hodges-Kluck & Reynolds 2012), J1203 is another S-shaped galaxy (Rubinur et al. 2017). The precession of the jets in Z or S shaped sources can be due to (i) the presence of a dual AGN system or (ii) the tilted accretion disk of a single AGN.

2MASX J14454130+3341080

J1445 shows an extended structure in which the bright component is likely to be the core and the extended emission is the radio jet. However, the spectral index image indicates the opposite to be true, i.e. the bright region has a spectral index value of -1.38 ± 0.56, whereas the extended region has $\alpha = -0.79 \pm 0.74$. Therefore, it is possible that this system has two AGN where both nuclei have a steep spectral index due to the core-jet structures. Alternatively it could have a single core jet structure. We need high-resolution observations to distinguish between a DAGN or a single core-jet structure in this radio source.

4.3.3 Double-peaked emission lines in our dual radio source galaxies

We have selected our sample based on their nuclear double-peaked emission lines expecting that these double-peaks may arise from the dual AGN. However, we have detected dual radio sources in 3 of our sample galaxies at the separation $\geq$ 3″; the SDSS fiber has a radius of 3″. Therefore, the dual radio structures cannot produce the double-peaks in the spectra of our sources as they lie at separations greater than the SDSS fiber diameter. Instead, jet-ISM interaction, outflows or NLR rotating disks can be the origin of the double-peaks. In the rotating disk model, the red-shifted and blue-shifted line components should have the same flux densities as they originate from a single object (Smith et al. 2010). We cannot rule out any of the three possible origins of double-peaked lines with only radio data and SDSS spectra. Müller-Sánchez et al. (2015a) has mapped the [O III] region of their sample DPAGN galaxies. They have estimated the position angle of the [O III] emission, the position angle of the radio emission and the position angle of the galaxy. Due to lack of [O III] observations, we cannot rule out any one of the three possible origins of double-peaked lines only with radio data and SDSS spectra.

Here, we discuss the three types of origin of the double-peaks in our detected dual radio source objects. J1006 has compact core (A). We have not detected any jet structure though the spectral index (α) is steep. The SDSS spectrum has a double peaked [O III] doublet. It also has a double-peak in the Hβ line. The [O I] doublet is also present which indicates the presence of shock-heated gas (Kharb et al. 2017). The [O III] double-peaks are not symmetric. Hence, this rules out an NLR disk origin for the DPAGN emission. As radio jets were not detected, it is possible that outflows or shock heated gas can produce the double-peaks in the J1006 optical spectrum.

J1355 has a steep spectrum compact radio core (A). The [O III] double peaks are not symmetric. Multiple narrow line components are usually associated with outflows (Crenshaw et al. 2010). We find that the narrow lines in J1355 have multiple components. [O I]6363 is not present in the SDSS spectrum but AGN broad lines are present. Hence, in J1355, outflows can give rise to the double-peaks.

J1617 has multiple peaks in the narrow lines. The [O III] emission line double peaks are symmetric. Ge et al. (2012) have fitted the spectra and found that the [O III] has a blue-shifted wing with velocity 508 km s^{-1}. We find that the radio image of J1617 shows a one sided jet at 15 GHz (A, Figure 4.3). Hence, the origin of the double-peaks can be either due to a rotating disk, outflows or jet-ISM interaction. None of these possibilities can be ruled out.

4.3.4 The double-peaked emission lines in the remaining sources

Two galaxies in our sample have extended radio emission. As we do not have [O III] maps of these sources, the direction of the [O III] regions cannot be determined. Hence, we cannot justify whether the jet is interacting with the [O III] region and producing the double-peaks. Therefore, jet-ISM interaction or outflows are the possible origin of double-peaks in these galaxies. At the same time, if the double-peaks are symmetric then the NLR disk can also give rise to the double-peaks. Multiple kinematic components in NLR, the presence of broad-lines or asymmetric wings are the the signatures of outflows. For example, the radio source J2304 has been studied earlier using the VLBA (Gabányi et al. 2016). They found that the DPAGN lines in J2304 can arise from jet- ISM interaction as they did not detect a second AGN or radio core. Furthermore, AGN broad- lines are also present in the SDSS spectrum of J2304. We found that all of our sample galaxies have broad

emission lines present in their SDSS DR12 [‡] spectra. So, there is a possibility that AGN outflows are creating the double-peaks in this source as well as the remaining sources in our sample.

4.3.5 The detection of dual AGN in our sample

We have observed 20 DPAGN, expecting that the double peaks are due to dual AGN and we would be able to resolve those DAGN with high resolution radio observation. We have detected one confirmed DAGN but this DAGN is not responsible for the double peaks in the sample galaxy. As discussed in the section 4.3.3, the detected DAGN is at the separation $\geq$ 3″ which is the size of the SDSS optical fiber. The detected DAGN is in a merging galaxy systems. Hence, we can say that the detection of DAGN from our DPAGN sample is zero and DAGN detections are more likely from closely merging galaxies.

Shen et al. (2011) have found that 10% of the DPAGN in their sample are DAGN. Müller-Sánchez et al. (2015a) have observed their sample at 8.5 GHz and 11.5 GHz. They have detected 3 dual AGN which is 15% of their sample. About 75% of the DPAGN in their sample arise from jet-ISM interactions. They have selected their sample from long-slit observations of DPAGN. Tingay & Wayth (2011b); Gabányi et al. (2016); Liu et al. (2017) have conducted VLBA studies of DPAGN sources but no binary/dual AGN were detected. Kharb et al. (2015a, 2017, 2019) have studied the DPAGN KISSR 1494, KISSR 1219 and KISSR 434 with the VLBA and found that the double-peaks are likely due to outflow-ISM interaction. Recently, Fu et al. (2015b) have searched for DAGN using the SDSS and FIRST images of the Stripe 82 degree region on the sky. They have searched for close companions or merger systems. They have observed that reliable dual core galaxies have SDSS AGN spectra that are associated with the individual cores in the VLA images.

[‡]www.sdss.org/dr12/

Fu et al. (2015b) have detected 4 dual AGN out of the 6 merging galaxies. From our observations also, we have found that most of the DPAGN are due to the jet-ISM kinematics or outflows. Hence, DPAGN are not a good tracer of DAGN. Satyapal et al. (2017) have also pointed out that many AGN are obscured in optical due the heavy dust. Hence, selecting the sample using SDSS low resolution optical spectra is not a good idea. They have used the IR color for their sample selection of DAGN and they have subsequently carried out Chandra observations of the sample. The detection rate is quite high in their sample. Although it is likely that the sample of merging galaxies would not always provide very close DAGN ($\leq 3''$) but there is a high probability of DAGN detection at the separation $\leq$ 10 kpc.

4.4 Summary

1. We have selected 20 DPAGN galaxies on the basis of the ΔV vs σ plot to search for dual AGN. We have studied these galaxies using high resolution VLA observations. The source 2MASXJ 12032061+1319316 shows a clear S-shaped radio jet suggesting precession (Rubinur et al. 2017) which we discussed in last chapter. The remaining 19 sources are discussed in this chapter.

2. From the radio morphologies, we find that three galaxies in our sample of 19 galaxies are dual radio sources at the separations of $\lesssim$ 10kpc, other two have extended radio structures. The remaining 13 galaxies have single radio sources and one galaxy is not detected.

3. The dual radio source galaxies are SDSSJ100602.13+071130.9, SDSSJ135558.08+001530.6 and 2MASXJ16170895+2226279. The radio sources have projected separations of 12, 8.2 and 5.6 kpc, respectively. All three galaxies are in merger systems.

4. From the spectral index map and SDSS spectra we have confirmed that radio sources in J100602.13+071130.9 form a dual AGN system. The primary object is a radio-weak AGN while the secondary has resolved two sided jets in 8.5 and 11.5 GHz images.

5. SDSSJ135558.08+001530.6 has two steep spectrum cores which can be a dual AGN or an AGN -starforming nuclei pair.

6. 2MASXJ16170895+2226279 has two cores where the primary core has a steep spectrum which is because of jet contribution detected at 15 GHz. The second core has a flat spectral index. This also can be an AGN or star-forming nucleus.

7. SDSSJ110215.68+290725.2 and 2MASXJ14454130+3341080 have extended radio structures in our observations at 8.5 and 11.5 GHz. SDSS J110215.68+290725.2 has a two-sided core-jet structure of size $\sim$6 kpc. This source has a large-scale jet of size 132 kpc in its VLA FIRST image. We found a directional change in the radio jet from the small scale (few kpc) to the large scale (100 kpc) image and it appears to have a Z shape. This radio structure can be due to precession of the radio jets caused by a dual/binary AGN system or a tilted accretion disk associated with a single AGN. The source 2MASXJ14454130+3341080 has a bright core and is extended out on one side to a radius of 1.14 kpc. Both the core and the extended structure have steep spectral indices.

8. We determined the SMBH masses, Eddington ratios and the star formation rates using the optical spectra and the radio emission (1.4 GHz). We found that the [O III] luminosity (L[O III]) is strongly correlated with the SFR(Hα).

9. As our detected dual AGN is at a separation of $> 3''$, we believe that the DPAGN in our sample do not originate from the dual AGN in these systems.

Jet-ISM interaction, outflows or NLR rotating disk give rise to the DPAGN in these galaxies.

10. High resolution radio observations alone cannot help us to determine the origin of the DPAGN in our sample galaxies. We deduce that most of the DPAGN arise from NLR-jet kinematics as we have not detected dual AGN in these systems. However, we can not rule out the possibilities of a faint second AGN or a nearby AGN which is below our resolution and sensitivity limits.

11. We find that DPAGN in low resolution optical spectra such as those in SDSS, are not good indicators of dual/binary AGN. Instead, closely interacting galaxies and merger remnants are good candidates for detecting dual/binary AGN.

Chapter 5

UVIT observation of dual nuclei and a multi-wavelength study of MRK 212

5.1 Introduction

Galaxies evolve through major or minor mergers as well as through distant interaction with nearby galaxies. It has been long known that mergers can trigger bursts of star-formation (Sanders et al. 1988). This is because tidal forces of interactions and mergers produce non-axisymmetric gravitational forces across the disks resulting in enhanced cloud collisions, shocks and star-formation in the galaxy disks. Simulations show that galaxy mergers/interactions also cause gas inflow onto the nuclei resulting in the accumulation of dense gas around the nuclei (Bournaud 2010). This triggers vigorous star-formation around the single or double nuclei. Thus, starbursts are found associated with the molecular gas clumps in the central regions of galaxies (Sargent & Scoville 1991). Hence, mergers and

close interactions of galaxies often fall in the category of starburst galaxies.

Gas that accumulates within the co-rotation radii (typically a radius of a few kpc) experiences gravitational torques and flows into the nuclear regions. Co-rotation rings are formed by collecting gas in the co-rotation radii. Gas also flows outwards resulting in long tidal tails. Thus models of star-formation predict an increase of the star formation rate both in the disks, in the nuclei and also in the outer tidal tails (e.g. Duc et al. 2000). The UV images of interacting and merging galaxies (e.g., the Arp Atlas) show that spatially extended (>1 kpc) star-formation and nuclear activity (on scales <1 kpc), each contribute approximately 50% to the total star-formation in the merging systems (e.g. Kaviraj et al. 2009)

During mergers, as the nuclear mass concentration and gas inflow increases, AGN activity can be triggered in one or both nuclei. It is due to mass accretion onto the SMBHs of the individual galaxies. The UV emission arises from the accretion disk around the SMBHs (Peterson 1997) as well as star formation around the AGN. Thus AGN are are often associated with galaxy mergers and starburst activity, a good example being the ultra-luminous infrared galaxies (ULIRGs) that often have AGN as well as extreme star formation (Nagar et al. 2003; Clemens et al. 2010; Collier et al. 2018).

The new ultra-violet telescope UVIT on *Astrosat* satellite has a spatial resolution of $\sim 1.5''$ which is four times better than the resolution of *GALEX*. The high sensitivity and good spatial resolution of UVIT can help us detect dual AGN, starburst-AGN pairs as well as trace the associated star formation in their disks and tidal tails. Hence, we planned to observe a sample of nearby dual nuclei galaxies with UVIT. In the following subsection we summarise our main UVIT objectives.

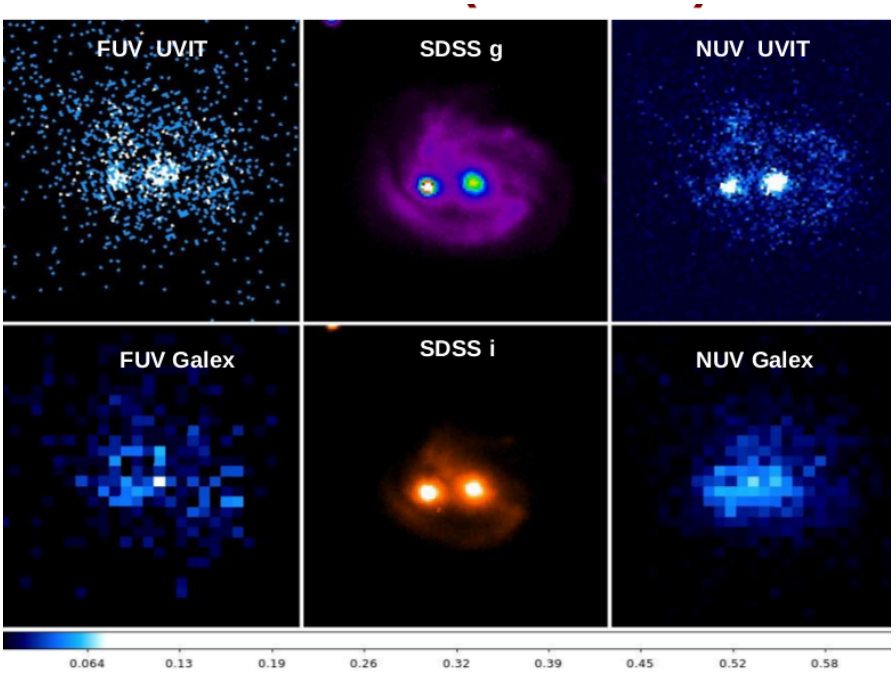

FIGURE 5.1: This panel shows images of MRK 739 which is a confirmed dual AGN. The UVIT images are not smoothed. This image show the resolution power of UVIT. Two nuclei are resolved in the UVIT image.

5.2 Objectives of our UVIT Observations

The main aims of our UVIT observations are the following:

(i) UV emission from dual AGN or starburst-AGN cores: The UV emission can arise from the accretion disks in the AGN or from star-clusters in the nuclear regions. Since our sources are nearby, we expect to resolve the starburst and AGN activity. The high spatial resolution of UVIT will be able to detect harder UV emission from individual AGN accretion disks in sources having dual AGN. Softer UV spectra would be consistent with starburst nuclei. In the present study we have only done UV imaging but in future we plan to study the UV spectra from DAGN as well.

(ii) Galactic Disk Structures: The higher sensitivity of UVIT will help us detect the extended star formation in the disks of the galaxies, as well as faint

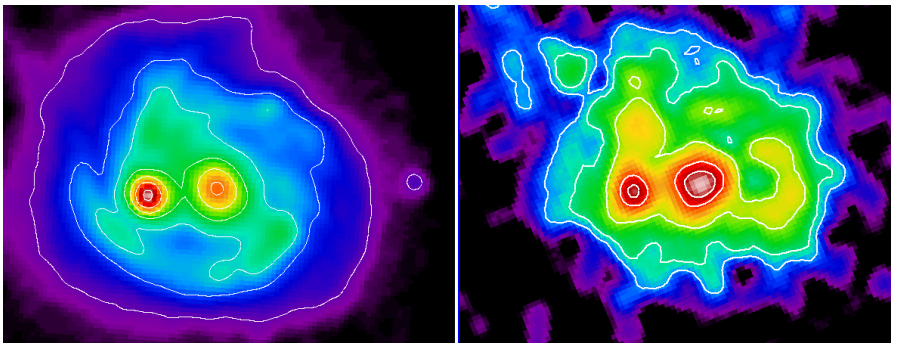

FIGURE 5.2: (Left) This is the SDSS B band optical image of MRK 739. (right) This is the UVIT 2.5 ksec image. The UVIT image shows extended UV emission which does not completely follow the optical emission.

tidal tails, rings and arcs. The high spatial resolution will allow us to resolve star-forming knots in the galactic disks and tidal tails.

(iii) SFR from Local regions: UV is one of the best tracers of star-formation. We will estimate the SFR in the disks and nuclear regions. We will also estimate star-formation in the tidal tails and compare the SFR from the different regions. This will directly examine the role of galaxy interaction in enhancing star-formation activity in galaxies.

(iv) Comparison with Optical/NIR images: We will use SDSS data to determine the optical counterpart of the UVIT images. To trace tidal structures, we will carry out HCT optical observations (spectroscopy or imaging). The SFR estimates obtained from optical/NIR will be compared and contrasted with SFR from UV. This will highlight the presence or absence of dust and trace extinction/reddening in these galaxies.

(v) Comparison with Multi-wavelength data: We will use archival X-ray and radio data to complement the observations. We plan to carry out followup high resolution radio observations (e.g. with the VLBA or high-frequency VLA) of the sample galaxies to confirm the nature of the nucleus.

5.3 Sample Selection

We used the sample of optically identified dual nuclei from Mezcua et al. (2014), to define a sample of mergers/merger remnants to observe with the UVIT. Their sample included 52 dual nuclei galaxy mergers where most of the sources have projected separations of $\leq$ 4kpc. As the UVIT has a spatial resolution of $\sim$1.5″, we selected galaxies which have a redshifts of z<0.1 so that the separation of the dual nuclei is large enough to be resolved with the UVIT. Then we checked that there is UV emission in the corresponding GALEX observations. Only sources with good UV detection from GALEX were selected. Galaxies which already have high resolution UV observations from the UVIS camera in HST were rejected. The sample included the following types of dual nuclei: 1) Two AGN known as dual AGN at separation of 10 kpc to 100pc. 2) One nucleus is an AGN and the other one is a star-forming nucleus. 3) Both are star-forming nuclei. We selected 17 galaxies for our sample from the larger sample of 52 galaxies. The sample includes two confirmed dual AGN MRK 739 and ESO 509-IG066 NED 02.

5.4 Current Results

So far, we have observed 15 galaxies with UVIT (table 5.1). We have obtained preliminary images of 6 galaxies. Figure 5.1 shows the UVIT images of the sample galaxies MRK 739 in comparison to GALEX images. However, we were able to complete all the UVIT objectives for one of our sample galaxies: MRK 212 with multi-wavelength data. The UVIT images of MRK 739 has also yielded interesting results. We first discuss the outcome of our UVIT observations of the galaxy MRK

TABLE 5.1: **UVIT observation details of sample galaxies:** Column 1: UVIT proposal ID; Column 2: Sample galaxy name; Column 3: Right Ascension, Column 4: Declination; Column 5: Redshift; Column 6: Accepted on-source time for observation; Column 7: Filter in NUV band; Column 8: Filter in FUV band. ** deep 15 ksec observation of MRK 212 which we will discuss in next section (5.5).

Proposal ID	Galaxy name	RA	DEC	Redshift	Exposure time(s)	NUV filter	FUV filter
A02-165	MRK 721	10:23:32.616	10:57:34.992	0.032092	2000	NUV-B13	Sapphire
A02-165	MRK 212	12:28:15.235	44:27:11.304	0.022893	1500	NUV-B13	Sapphire
A02-165	MRK 306	22:31:51.247	19:41:28.968	0.018696	1500	NUV-B13	Sapphire
A03-091	SDSS J143648.10+182037.6	14 36 48.084	18 20 37.210	0.04860	2500	NUV-B13	Sapphire
A03-091	ESO 509-IG 066 NED 02	13 34 40.770	-23 26 45.200	0.033223	2500	NUV-B13	Sapphire
A03-091	MRK 729	11 9 49.270	12 46 17.060	0.042616	2500	NUV-B13	Sapphire
A03-091	MRK 789	13 32 24.240	11 6 22.586	0.031454	2500	NUV-B13	Sapphire
A03-091	MRK 3758 (MRK 739)	11 36 29.100	21 35 47.004	0.029854	2500	NUV-B13	Sapphire
A03-091	NGC 3773	11 38 12.967	12 6 42.910	0.003276	2500	NUV-B13	Sapphire
A04-067**	MRK 212	12:28:15.235	44:27:11.304	0.022893	**15000**	Silica	CaF2
A04-085	SDSS J101920.83+490701.2	10 19 20.827	49 7 1.020	0.0540	5000	Silica	CaF2
A04-085	SDSS J102700.40+174901.0	10 27 0.401	17 49 0.900	0.0665	5000	Silica	CaF2
A05-082	SDSS J123351.61+195311.8	12 33 51.612	19 53 11.760	0.0737	5000	Silica	CaF2
A05-082	SDSS J125741.05+202347.8	12 57 41.050	20 23 47.796	0.0806	5000	Silica	CaF2
A05-082	SDSS J133638.35+203232.9	13 36 38.347	20 32 32.928	0.0726	5000	Silica	CaF2
A05-082	SDSS J142722.83+200549.4	14 27 22.834	20 5 49.344	0.0758	5000	Silica	CaF2

739 below. In the next section (5.5) we discuss results from our multi-wavelength study of the galaxy MRK 212.

Result of MRK 739: MRK 739 is a confirmed dual AGN (Koss et al. 2011). One of the nuclei is a Seyfert 1 type of AGN while other nuclei is Seyfert 2 AGN but it also hosts starburst activity. The nuclei are at a separation of 3 kpc. The optical spectra shows signature of outflows from one of the nuclei (Koss et al. 2011). The molecular gas profile is asymmetric (Koss et al. 2011). The UVIT images show the star forming regions around the nuclei of MRK 739 which does not follow the optical tidal arms (Figure 5.2). This star-formation can be due to positive AGN feedback. The conditions for positive feedback are (i) nuclei should have outflows (2) star forming regions should appear associated with outflows and (3) kinematics of stars around the AGN should indicate high velocities (Maiolino et al. 2017). We need optical spectroscopy at different position of MRK 739 to

investigate the velocities. With 2.5 ksec UVIT observations, we are able to detect UV emission surrounding the nuclei. However, we need much deeper observation to find the direct signature of AGN feedback related star-formation. We have realized this especially after our deep 15 ksec UVIT observation of MRK 212 yielded interesting results (which is discussed in the next section).

5.5 MRK 212: A Multi- wavelength study

We have done radio, optical and UV study of the dual nuclei galaxy merger MRK 212. MRK 212 is a double-pinwheel galaxy (UGC 07593 NED02). The companion galaxy is UGC 07593 NED01. Here, we call MRK 212 as source 1 and its companion as source 2. Source 1 has a redshift (z) of 0.022893 ± 0.000133 (luminosity distance D_L = 98.8 Mpc, scale= 0.459 kpc/arcsec)*. The source 2 has a redshift (z) of 0.022352 ± 0.000063 (luminosity distance D_L = 96.5 Mpc, scale= 0.449 kpc/arcsec). The SDSS† image (Figure 5.3) shows that the projected nuclear separation is 11.8 arcsec or ∼5.6 kpc. The two radio sources are resolved in the FIRST‡ image (Figure 5.3) but not in the NVSS§ image. Both sources are spiral galaxies of type Sb and Sbc. The SDSS image shows that the inner arms of each galaxy is nearly merged, while the outer arms appear to be unaffected (Figure 5.3). Mezcua et al. (2014) have carried out a photometric analysis of this system and obtained r-band magnitudes of 21.77 (luminosity $10^{40.63}$ erg/sec) and 22.86 ($10^{40.20}$ erg/sec) respectively, for source 1 and source 2 respectively. There is an SDSS optical spectrum of source 2 and it is identified as a star-forming galaxy.

*https://ned.ipac.caltech.edu/
†www.sdss.org
‡http://www.cv.nrao.edu/first/
§http://www.cv.nrao.edu/nvss/

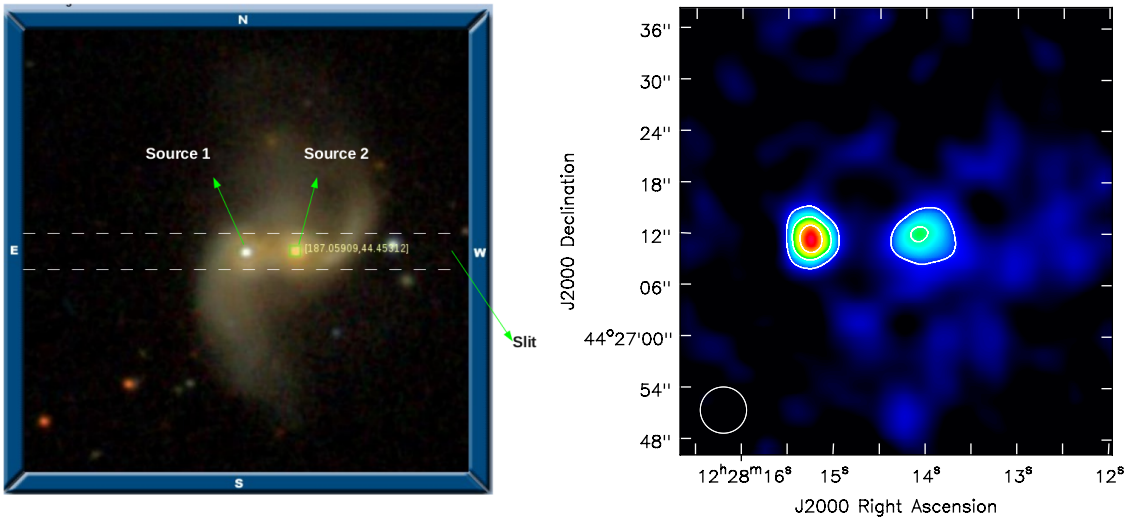

FIGURE 5.3: (left) The SDSS color composite image of MRK 212. Superimposed on the figure is the slit position of our HCT observation. The nucleus on the left is MRK 212 and is called source 1 and the companion is called source 2 throughout this paper. (right) This is the 1.4 GHz FIRST map of MRK 212 overlaid with contours in white.

5.5.1 Observations and Data Analysis

5.5.1.1 Radio Data

The FIRST image shows two nuclei. We searched for further VLA archival data, before we applied for new observations. There are two data sets available in the NRAO VLA archive: (i) MRK 212 was observed in the C-band (4.86 GHz) using the B-array on 14th July, 1986 (VLA/AM183) for ∼11 min along with the flux density calibrator 3C286 for 3 min. J1323+321 was observed for 2 min as a phase calibrator. It is single channel observation with a total bandwidth of 50 MHz. This data is in B1950 epoch. (ii) The X-band data is available. This observation was done on 16th Feb, 2004 (VLA/AB1122) at 8.46 GHz using the BC-array. The science target was observed for 4 min along with flux density calibrator, J1331+305 for 6 min and phase calibrator J1219+484 for 5 min. The total bandwidth was 50 MHz.

TABLE 5.2: **The Radio observation details:** Column 1: Frequency bands; Column 2: Central frequencies; Column 3: Array configuration; Column 4: On-source time; Column 5: Date of observation; Column 6: Observation ID.

Band	Central frequency	array	Resolution	Exposure time(s)	date of observation	observation ID
C-band	4.86	B	1.46″	12 min	14th July, 18986	VLA/AM183
X-band	8.46	BC	1.03″	4 min	16th Feb, 2004	VLA/AM1122
Ku-band	13.5	B	0.40″	12 min	8th Sept, 2017	VLA/17B-123
Ku-band	16.5	B	0.40″	13 min	8th Sept, 2017	VLA/17B-123
Band-5	1.46	-	2.0″	$\sim$ 4 hrs	5th Nov, 2018	GMRT/35-076

After obtaining the images from archival 4.86 and 8.46 GHz data, we observed MRK 212 on 17th Sep, 2019 (VLA/17-123) with VLA in the Ku-band in the B-array with centered frequencies 13.5 and 16.5 GHz. The observations were done with 17 spectral window (spw), each having 64 channels i,e a total bandwidth of 1.28 GHz. MRK 212 was observed for 8.30 min. The flux density calibrator 3C286 and the phase calibrator J1219+4829 were observed for 5 min and 3.30 min respectively. We have obtained uGMRT observation of MRK 212 on 4th Nov, 2018 with band 5 at 1.4 GHz. The uGMRT band 5 has total 2047 channels with a bandwidth of 400 MHz. The science target was observed for $\sim$4 hrs whereas the flux density calibrator, 3C286 and phase calibrator, J1219+4829 were observed for 20 min and 65 min respectively. We have used CASA and AIPS packages for VLA and GMRT data reduction and further image analysis (see Chapter 2). We have flagged the bad data and then calibrated the data using the phase and flux density calibrators. The task CLEAN in CASA was used to make the images after a satisfactory calibration (See details in chapter 3). We have also used VLA pipeline images (where available) for comparison and further analysis. The spectral index maps were made using the COMB task in AIPS and IMMATH task in CASA.

5.5.1.2 Optical Data

The observations were done using the 2-m HCT, Hanle, India (see Chapter 2). HFOSC, mounted on HCT was used for obtaining the optical spectrum. For the galaxy observations the slit $11' \times 1.92'$ was used in combination with grism 7. This has a dispersion of 1.46Å and covers the wavelength range of 3700-7200Å. The details of the observation is shown in Table 5.3. The slit was put in such a way that it covers both the nuclei. The wavelength calibrations was carried out using the ferrous argon arc lamp and the flux was calibrated using the standard stars (Oke 1990).

The data reduction was done using the software package IRAF. The pre-processing steps include trimming and bias subtraction. The tasks IMCOPY, ZEROCOBIME and IMARITH were used. The one dimensional spectrum was extracted, with the APALL task. This task include defining the aperture, the spectrum extraction, and tracing the spectrum along the dispersion axis. Each of the individual core nuclei were extracted by defining suitable apertures. The task APALL returns the background subtracted output spectrum that also contains the galactic spectrum with sky background, the background sky spectrum and the error spectrum. The calibrations lamps were extracted with reference to the respective target sources. The atomic emission lines in the calibration lamp spectra were identified and the pixel to wavelength mapping was done using the task IDENTIFY. The wavelength calibrated spectra was also calibrated for flux using the standard star spectra taken on the same night, with the task STANDARD. The resolution was determined with the skyline at 5577Å . The full width at half maximum (FWHM) was obtained at 5577Å is $\sim$ 8.5Åfor grism 7. Flux calibrated spectra were redshift corrected with task DOPCOR and corrected for reddening due to the Galaxy. The galactic spectra and error spectra were separated from the calibrated spectra, using task SCOPY.

TABLE 5.3: HCT optical observation details

galaxy	exposure time(s)	date of observation
Mrk 212	3600	2017-01-31
Feige 67	360	2017-01-31

5.5.2 X-ray Archival Data

A Chandra X-ray archival data set of MRK 212 is available in Chandra the archive. The observation was done with the Advance CCD imaging spectrometer (ACIS-I) on 10th April, 2000 (PI: Takahasi) to observe the X-ray source AX J1227.6+4421. MRK 212 is situated $7'$ away from the target source. The total integration time of observation is 5.65 ksec. The expected spatial resolution is $\sim 1''$.

5.5.2.1 UV Data

We have observed MRK 212 with the Ultra-violet imaging telescope (UVIT) (see chapter 2). The UVIT has a spatial resolution of $\sim 1.5''$, which is three times better resolution than GALEX ($\sim 5''$). MRK 212 was observed with UVIT in two cycles, the first observation in cycle A03 was for 1.5 ksec only but we were able to detect the two nuclei but we could not separate the AGN and nuclear star formation. Hence we requested deeper 15 ksec observations in the following cycle. Here, we present the 15 ksec UVIT observation of MRK 212 (A04-091). This observation was done with the FUV CaF2 (1481-1981 Å) and NUV-Silica (2418-3203 Å) filters. We have reduced the data using JUDE pipeline (Murthy et al. 2016, 2017). The L2 pipeline images that are released by *ASTROSAT* are also used in the analysis.

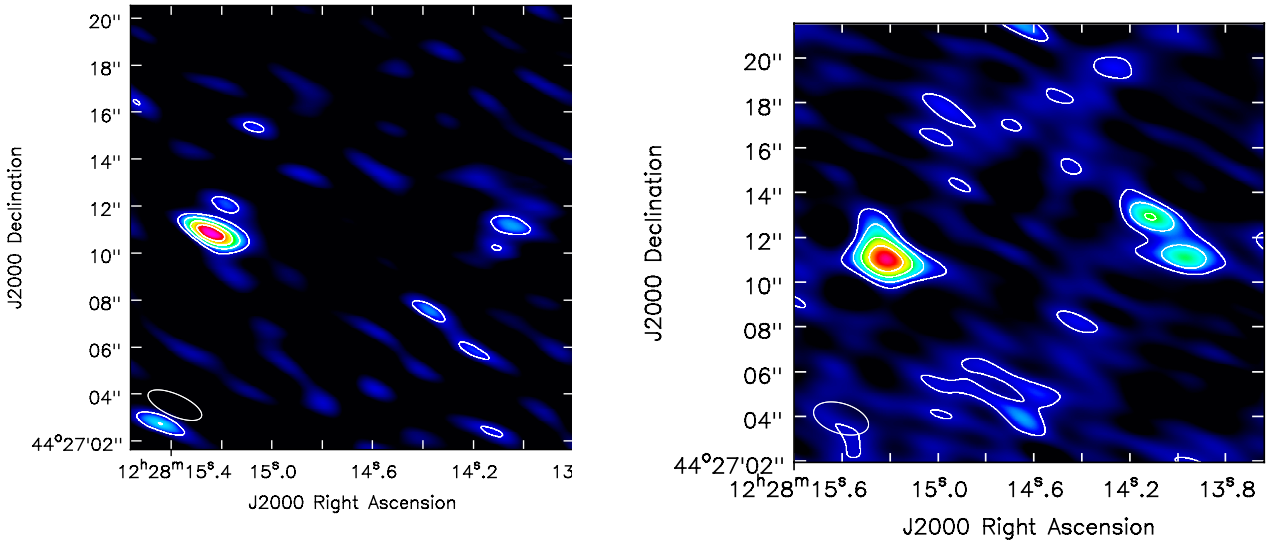

FIGURE 5.4: (left) The C-band, 4.84 GHz image. This image is from a radio 1986 observation. The signal to noise ratio is very low but both the sources are detected. (right) The X-band, 8.46 GHz image. Both the sources are detected. Source 2 shows two resolved radio structures (A, B, see Figure 5.5). The contour levels are 20, 40, 60 and 80 % of the peak flux density value.

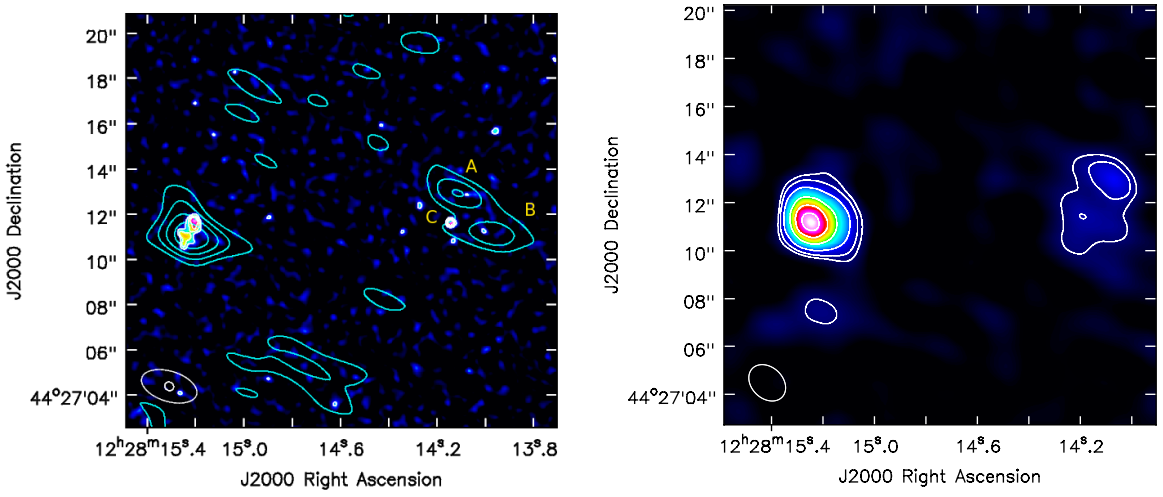

FIGURE 5.5: (left) The Ku-band 12-16 GHz image of MRK 212 with X-band contours overlaid. Source 1 shows a extended structure in SW-NE direction. Source 2 shows a compact structure (C). This coincides with optical centre but offset from two sided radio structure (A, B) in X-band image. (right) uGMRT L-band image with contours. Both the sources are detected in this 1.4 GHz image. Source 2 is resolved. The contours are 20, 40, 60, 80 % of the peak flux density.

5.5.3 Results

5.5.3.1 Radio Images

We have reduced the 4.84 GHz, 8.48 GHz, 12-18 GHz VLA data, and 1.4 GHz uGMRT data of MRK 212. As mentioned earlier, the FIRST image shows two radio sources and the source 2 has extended radio emission coincident with the tidal arm.

(i) The C-band (4.84 GHz) image (Figure 5.4) shows two radio sources at $\sim$ 6 kpc. However due to the limited amount of data, we could not obtain a better image. We have found the VLA pipeline image of the same dataset. This image has detected only source 1. The natural weighted flux density is comparable in both the images. However, we have made the Briggs weighted images which give a better flux density. The task IMREGRID in CASA was used to transform the image from B1950 to the J2000 co-ordinate system.

(ii) The X-band (8.46 GHz) image (Figure 5.4) shows two radio structures at a separation $\sim$ 6 kpc. The source 1 shows a single radio source with small extended structure in the North and South -West directions. The source 2 shows two sided extended structure of size $\sim$ 2 kpc. It has two distinct radio bright symmetric regions (A, B in Figure 5.5) in the North East (NE)-South West (SW) direction. However, the overlay of the X-band radio image with the optical image shows an offset in the position of the source 2 radio structures from the optical position. The two sided structure is $\sim 1''$ away from the optical core.

(iii) The Ku-band (15 GHz) image (Figure 5.5) has detected two sources. It shows an extended radio structure in source 1 and compact radio core (C) in source 2. This radio core (C) coincides with the optical centre and is at the middle of the

TABLE 5.4: **Radio Properties of MRK 212:** Column 1: Observation ID; Column 2: The observed frequency; Column 3: The beamsize: Major axis (θ_1), minor axis (θ_2) and position angle (PA); Column 4:The RMS noise; Column 5: Integrated flux density of source 1; Column 6: Integrated flux density of source 2

Observation ID	Frequency (GHz)	Beam ($\theta_1 \times \theta_2$, PA)	Image Noise in μJy	Source 1 Int Flux density (mJy)	Source 2 Int Flux density (mJy)
FIRST	1.4 GHz	$5.40'' \times 5.40''$, 0.0°	182	2.31	3.59
VLA/AM183	4.86	$2.46'' \times 0.93''$, 66.278°	130	0.97	0.76
VLA/AB1122	8.46	$2.53'' \times 1.36''$,72.73°	65	0.77	resolved
VLA/17B-123	12-16	$0.43'' \times 0.36''$, 52.65°	6	0.30	0.05
GMRT/35-076	1.4	$1.72'' \times 1.30''$, 46.26°	26.3	2.31	1.54

two sided structure (A, B) in the X-band image with a horizontal shift of $1''$. We could not detect the two sided structure (A,B) in the source 2. We have also made images at the two central frequencies (13.5 and 16.6 GHz) expecting to make the spectral index map of both the sources.

(iv) Figure (5.5) shows the total bandwidth uGMRT image. The uGMRT has a bandwidth of 400 MHz with $\sim$ 2000 channels where one can make the images with $\sim$ hundred channels at two edges and make the spectral index maps. We found that the initial 50 - 700 channels and the end 1400 - 1950 channels have good data. Hence, we have tried to make two separate images with these channels. The Briggs weighted image shows two radio sources. Source 1 has a compact radio structure but the source 2 has an extended structure similar to X-band images (Figure 5.5).

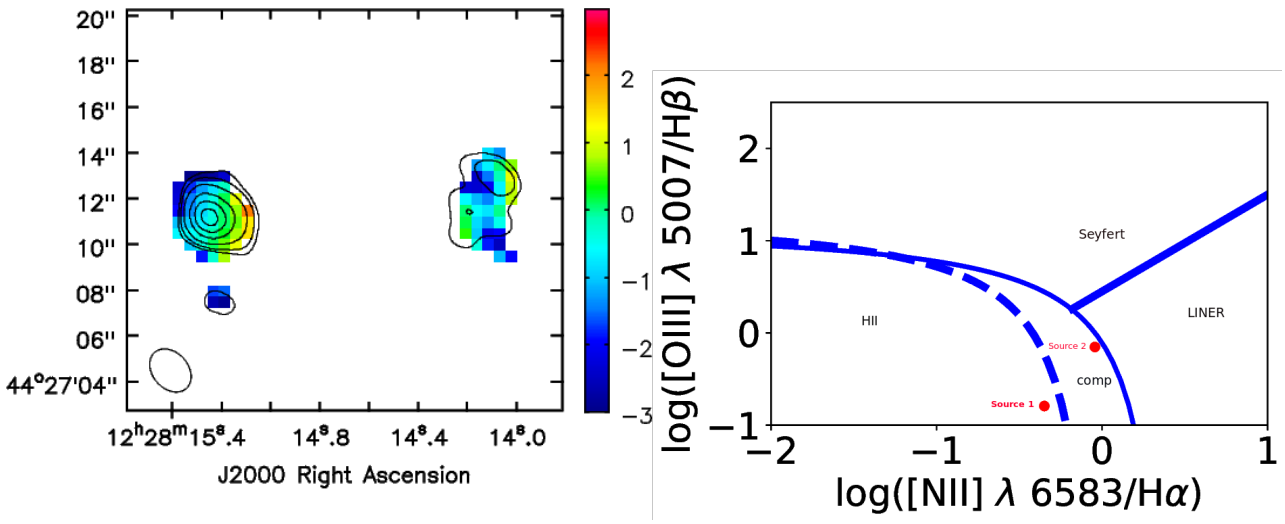

FIGURE 5.6: (left) The spectral index map from the 1.112 and 1.326 GHz images from uGMRT data. (right) BPT diagram. The red points are source 1 and source 2. Source 1 falls in SF region where source 2 falls in SF+ AGN region.

5.5.3.2 Spectral index (α)

We have made the Ku-band observation at two central frequencies (13.5 and 16.5 GHz) in order to make the spectral index map. However, due to missing flux in source 1, we could not obtain the spectral index map corresponding to source 1. Source 2 has a steep spectral index value i.e. $\alpha_{13.5}^{16.5} = -1.04 \pm 0.92$. This indicates the presence of unresolved jets.

Further, the spectral index values are calculated from the integrated flux densities using FIRST, C- and X-band images. This gives a spectral index value of source 1 as $-0.40 < \alpha < -0.65$. The spectral map (Figure 5.6) obtained from uGMRT images (1.112 and 1.366 GHz) also shows a flat spectral index ($\alpha = -0.56 \pm 0.47$) of source 1. Source 2 has unresolved structure at 1.4 GHz FIRST and 4.84 GHz C-band images. We have calculated the spectral index value using flux densities from these two images which turns out to be $\alpha_{1.48}^{4.86} = -1.3$ which is steep and indicates the presence of old electrons from an extended jet structure. The spectral index

map from the uGMRT images also show steep spectral index value (Figure 5.6).

5.5.3.3 Optical spectra

The optical spectra of the individual sources was obtained from HCT. The flux of the fitted emission lines are given in table 5.5. We have calculated the ratio of [NII]λ6583 to Hα and [OIII]λ5007 to Hβ for each of the sources. Then, these points are plotted in the Baldwin, Philips and Terlevich (BPT, Baldwin, Phillips & Terlevich (1981a)) diagram with the boundaries from Kewley et al. (2006). This is one of the best ways in which to distinguish between normal AGN (Seyfert and quasar), LINERs (discussed below) and normal HII regions. Source 1 falls on the Star-forming region on the plot and source 2 falls in the AGN+SF region.

5.5.3.4 X-ray

The spectral fitting is done using the SHERPA fitting tool. The source is fitted with a basic photon power-law and photo-electric absorption whose equivalent hydrogen column is determined from the Heasoft nH tool. The estimated integrated flux between energy range 0.3-7 keV is 3.4×10^{-14} erg s^{-1} cm^2 and the best fit photon index $\Gamma = 2.48^{+1.21}_{-0.99}$. We also measure count rates and determine strength of the hardness for each nucleus (tabulated in Table 5.6). The regions used for measuring count rates is marked in Figure 5.7. These regions enclose the Eastern and Western nucleus. The soft band rate for the Eastern nucleus is twice that of the Western nucleus and the hard band rate for the Western nucleus is a factor of 3 higher than the Eastern nucleus. This suggests that the Eastern nucleus has a softer spectrum while the Western nucleus has a harder spectrum. The hardness ratio is defined as HR = (H-S)/(H+S) where S and H are the soft (0.5-2 keV) and hard (2-7 keV) X-ray band net counts respectively. The HR for the Western

TABLE 5.5: **Result of best fitted optical lines:** column 1: Line name; column 2: Wavelength in Å; column 3: Flux in 10^{-17} erg cm^{-2} s^{-1}

line name	Wavelength (Å)	Flux (10^{-17} erg cm^{-2} s^{-1})
	Source 1	
Halpha+[NII]	6582.95 ±0.04	30.4765 ±0.256530
	6547.95± 0.0	10.3310±0.0
	6562.57 ± 0.0246	68.0408 ± 0.375600
[OIII]	5005.40 ±0.4226	3.02411± 0.457083
H_β	4861.41 ± 0.064	18.7349 ± 0.296102
[SII]	6715.60 ± 0.266	3.95626± 0.259195
	6731.30 ±0.147734	4.58670 ± 0.216194
	Source 2	
Halpha+[NII]	6583.39 ± 0.0646833	18.5148 ± 0.239452
	6548.39± 0.00000	6.27619 ± 0.000000
	6562.81± 0.0715671	20.4699 ± 0.291040
[OIII]	5006.56 ± 0.259333	4.52930 ± 0.450242
H_β	4862.18 ± 0.174557	6.43371 ± 0.294277
[SII]	6717.14 ± 0.643079	2.27528 ± 0.341627
	6730.57 ± 0.261565	4.45629 ± 0.325295

nucleus is higher compared to the Eastern nucleus indicative of heavy obscuration due to an increase in the local absorption column density in merging systems (Kocevski et al. 2015; Ricci et al. 2017). Because of a fewer counts, an additional intrinsic absorption component to the power-law fit resulted in poor statistics and the parameters could not be constrained.

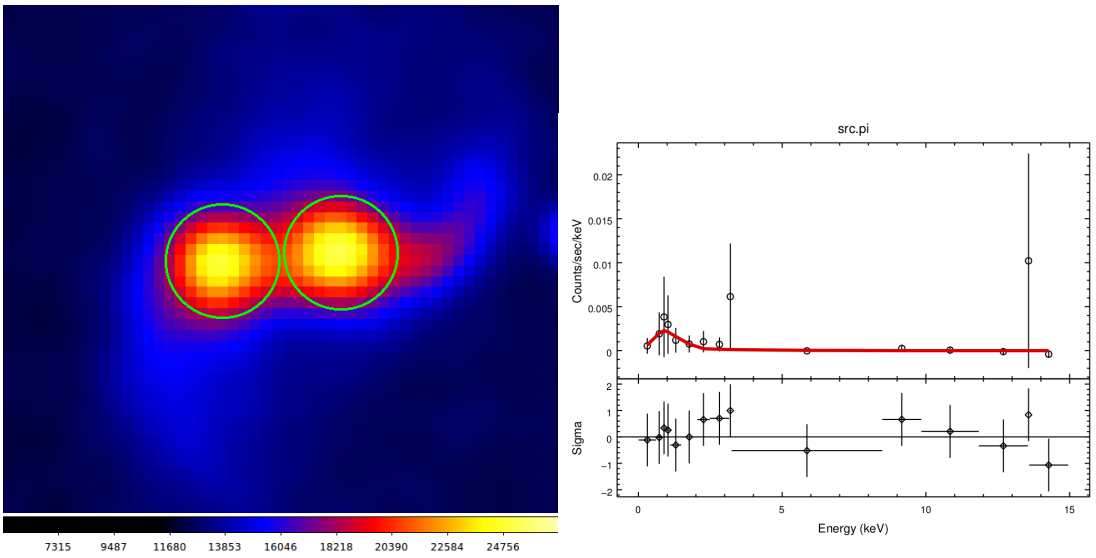

FIGURE 5.7: The optical DSS image of Mrk 212. The two regions marked in green are used to measure the hardness of each core using X-ray observations. The Chandra X-ray spectrum was extracted from the 15 arcsec region. The best fit absorbed power-law model is shown in red and the residual is also shown.

TABLE 5.6: Count rates for the soft band (0.5−2 keV) and hard band (2−7 keV) for regions defined in Figure 5.7

Region	Soft rate (S) (10^{-3} ct s^{-1})	Hard rate (H) (10^{-3} ct s^{-1})	Hardness Ratio (H-S)/(H+S))
East	1.61±0.54	0.36±0.25	-0.63±-0.23
West	0.72±0.36	1.26±0.45	0.27±0.28

.

5.5.3.5 UV

The GALEX image of MRK 212 shows two nuclei as well as the tidal arms. The high resolution UVIT image with exposure time 2.5 ksec could only resolve the UV emission from that lying in between the two galaxies. However, in the long exposure (15 ksec) image (Figure 5.8), we have detected emission from both galaxies, the tidal arms as well as the star-forming UV knots in the source 2. The two UV knots in source 2 are rsolved and they coincide with regions A, B in the 8.46 GHz image. We have visually selected the UV bright regions and calculated the SFR using Calzetti et al. (2007) following steps from Rahna et al. (2018). The

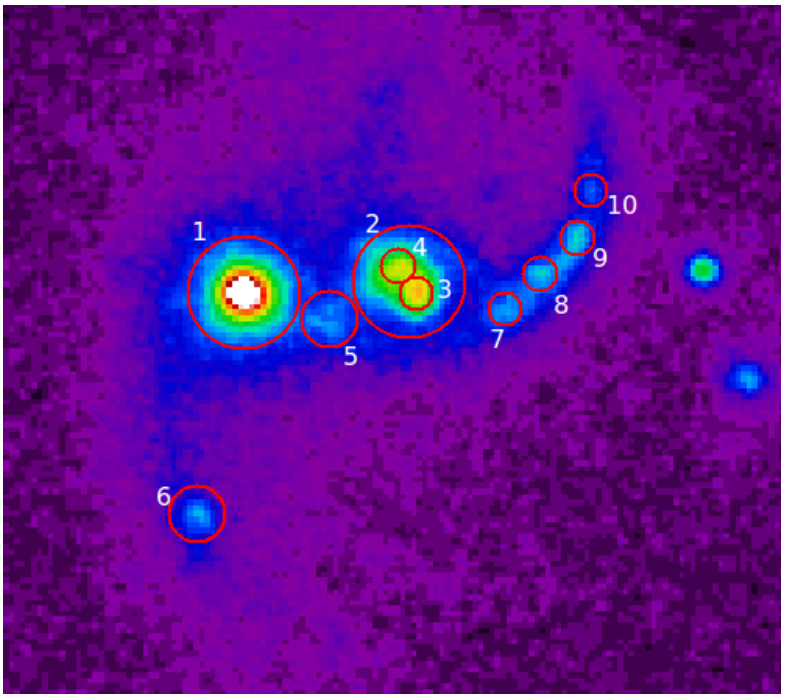

FIGURE 5.8: The NUV image of MRK 212 from UVIT observation. This deep 15 ksec image has resolved star-forming knots. Source 2 has two such bright UV knots (regions 3 and 4) which coincides with the X-band two sided structure (A, B). These circles are regions selected to calculate the SFR.

calculated SFR ranges from $3{\times}10^{-4}$ to $2.7{\times}10^{-3}$ $M_{\odot}$ yr^{-1} in NUV and $6{\times}10^{-4}$ to $2.9{\times}10^{-2}$ $M_{\odot}$ yr^{-1} in FUV. The average uncertainty in the SFR calculation is $<$ 5%. However, extinction corrections are not done yet.

5.5.4 Mass of the SMBHs:

The velocity dispersion of the nuclear stellar component ($\sigma_{\star}$) is used to calculate the mass of the SMBHs in source 2. The $\sigma_{\star}$ is obtained from the SDSS spectra. We could not calculate the $\sigma_{\star}$ values of the individual sources from our HCT observation because it has dispersion greater than 150 km/sec. Source 2 has a $\sigma_{\star}$ value of 127.58 km/sec. This gives an upper limit to the mass of the SMBHs as $(1.62 \pm 0.33) \times 10^{7} M_{\odot}$ (McConnell & Ma 2013).

TABLE 5.7: **SFR calculation from UVIT obs:** Column 1: Visually selected uv bright region number corresponding to Figure 5.8; Column 2: NUV count per second (CPS); Column 3: Corresponding NUV flux; Column 4: NUV luminosity; Column 5: Star-formation rate (SFR) from NUV luminosity; Column 6: FUV count per second (CPS); Column 7: Corresponding FUV flux; Column 8: FUV luminosity; Column 9: Star-formation rate (SFR) from FUV luminosity.

Region No	NUV CPS	$Flux_{NUV}$ (erg/s/cm^2/Å)	$Luminosity_{NUV}$ (erg/s)	SFR_{NUV} (10^{-3} $M_\odot$ yr^{-1})	FUV CPS	$Flux_{FUV}$ (erg/s/cm^2/Å)	$Luminosity_{FUV}$ (erg/s)	SFR_{FUV} (10^{-3} $M_\odot$ yr^{-1})
1	0.161	3.141e-17	2.822e+40	2.748	0.298	1.2526e-15	6.4534e+41	29.222
2	0.059	1.148e-17	1.032e+40	1.005	0.154	6.4735e-16	3.3350e+41	15.101
3	0.015	3.029e-18	2.721e+39	0.265	0.03019	1.2690e-16	6.5379e+40	2.960
4	0.011	2.178e-18	1.957e+39	0.190	0.02283	9.5968e-17	4.9440e+40	2.238
5	0.002	4.963e-19	4.459e+38	0.043	0.04962	2.0858e-16	1.0745e+41	4.865
6	0.004	9.112e-19	8.186e+38	0.079	0.01448	6.0868e-17	3.1357e+40	1.419
7	0.001	3.551e-19	3.190e+38	0.031	0.0065	2.7323e-17	1.4076e+40	0.637
8	0.006	1.318e-18	1.184e+39	0.115	0.01477	6.2087e-17	3.1985e+40	1.448
9	0.003	6.357e-19	5.710e+38	0.055	0.01245	5.2334e-17	2.6961e+40	1.220
10	0.002	5.121e-19	4.600e+38	0.044	0.006808	2.8618e-17	1.4743e+40	0.667

5.5.5 Star-formation rate from Radio and Hα

We have calculated the SFR from the Hα and the radio emission of the sources. These SFR along with UV SFR (section 5.5.3.5) can help us to determine the origin of the nuclei emission. These SFR are calculated for total emission of the each sources. We have obtained the H_α fluxes obtained from HCT spectra which is given in Table 5.5. The SFR relation Kennicutt (1998a) is:

$$SFR_{H\alpha}(M_\odot yr^{-1}) = 7.9 \times 10^{42} L_{[H\alpha]}(ergs^{-1})$$

The H_α SFR turns out to be 0.006 $M_\odot$ yr^{-1} and 0.001 $M_\odot$ yr^{-1} for source 1 and source 2 respectively.

We have followed the Condon (1992) relation to calculate the SFR from the radio flux density:

$$SFR_{Radio}(M_\odot yr^{-1}) = L(WHz^{-1})/5.3 \times 10^{21} \nu(GHz)^\alpha$$

We have used the radio flux density from the FIRST map at 1.4 GHz (Table 5.2), assuming $\alpha = -0.8$ to calculate the SFR as sources are unresolved in FIRST map. The SFR_{radio} are 6240 $M_\odot$ yr^{-1} and 10353 $M_\odot$ yr^{-1} for source 1 and source 2 respectively.

5.6 Discussion

5.6.1 MRK 212: Is it a DAGN system?

The SDSS optical and FIRST radio map shows that MRK 212 has two merging sources with optical and radio bright nuclei. However, this is not sufficient to confirm the AGN nature of these two sources. The available SDSS optical spectra of source 2 defines it as star forming galaxy. Here, we discuss the results that we have obtained from our multi-wavelength observations of MRK 212.

Source 1: The calculated spectral indices from the integrated flux densities are $\alpha_{4.86}^{1.43} = -0.68$, $\alpha_{8.46}^{1.43} = -0.61$ and $\alpha_{8.46}^{4.86} = -0.41$. Also, the spectral index map using two sets of channels from the uGMRT 1.4 GHz map gives $\alpha_{1.36}^{1.11} = -0.56 \pm 0.47$. These spectral index values are expected from an AGN. However, the optical spectrum does not put source 1 in the AGN region of the BPT diagram. Although the BPT diagram is an essential tool to confirm the presence of AGN, there are several recent studies that show that due to gas accretion during mergers, the AGN can be obscured in dust. Satyapal et al. (2017) have found that their mid-IR selected DAGN sample do not show AGN signatures in their optical spectra. Next, we have compared the SFR calculated from different tracers like, Hα, UV, and radio. The calculated SFR from the radio observations is $\sim$ 6000 $M_\odot$ yr^{-1} while the Hα, NUV and FUV SFRs are $\sim$0.006, 0.002, 0.029 $M_\odot$ yr^{-1} respectively. The excess amount of radio flux can come from an AGN. Hence, the spectral

index values from radio observations and the excess radio flux density supports the presence of an AGN in source 1.

Source 2: Source 2 is resolved in the X-band observations and show extended structure in the 1.4 GHz uGMRT observations. Although the C-band observations have very poor signal to noise ratio (SNR), we have calculated the spectral index value taking the integrated flux densities from the C-Band and 1.4 GHz FIRST images. This turns out to be $\alpha_{4.86}^{1.43} = -1.30$ which is steep. This kind of steep spectral index is found in AGN where jets are unresolved. Next, we discuss the resolved structure of source 2. The X-band image shows a two sided, symmetric radio bright structure with two regions (A,B in Figure 5.5) of size $\sim$ 2 kpc. Morphologically, this looks like a two sided core-jet structure where the core is not detected. At the same time, these can be star-forming regions as well. Furthermore, from the radio-optical overlay, we found that this radio structure does not coincide with the optical centre of source 2. The Ku-band image has detected a small compact radio structure (C in Figure 5.5) and it coincides with the optical centre. The calculated spectral index value for this structure is steep (< -1). The 1.4 GHz uGMRT observation has resolved the structure and it shows that the emission extends from the centre towards the upper radio bright region in the X-band image. The flux ratio of the emission lines from HCT observations puts source 2 in the AGN+SF region of the BPT diagram. Again, the calculated SFR from radio emission is $\sim$ 10000 while from Hα, NUV and FUV the SFRs are $\sim$ 0.001, 0.001, 0.015 $M_\odot$ yr^{-1} respectively. In a recent study, Hernández-Ibarra et al. (2016) have fitted the SDSS spectra of source 2, then calculated the flux ratios and put it on BPT diagram. They found it to be an AGN. Here, these evidences support an AGN classification for source 2. So, in next section we discuss whether this AGN has an extended two sided structure which is detected at 8.4 GHz in the X-band and at 1.4 GHz in the GMRT image.

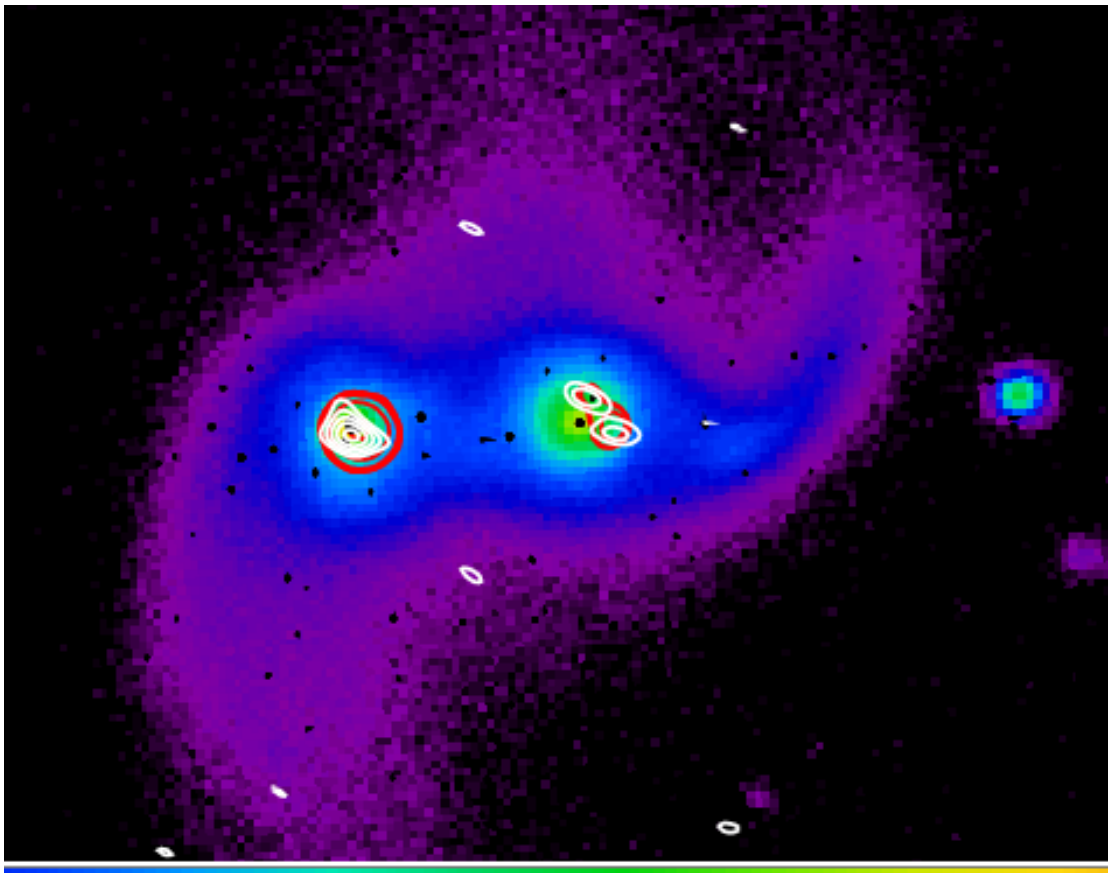

FIGURE 5.9: This is an optical image of MRK 212 with UV emission contours in red, 8.46 GHz contours in white and 15 GHz contours in black. The UV red contours on source 2 coincide with the radio 8.46 GHz white contours. This structure is $\sim 1''$ away from the optical centre where 15 GHz black contours are situated.

5.6.2 Does source 2 have a Core- jet structure?

The extended structure (A, B) at 8.48 GHz can be two star-forming nuclei, the two lobes of a core-jet AGN structure or a combination of both which is jet induced star-formations. As we have not detected a compact core and a two sided lobes in the same image, we can not define its morphologically to be a AGN core-jet structure. So we have used another method: we have checked the SFR of these two region from UV emission as well as from radio emission. Assuming a spectral index value of $\alpha = -0.7$, the calculated 1.4 GHz flux densities of A and B regions are 1.24 mJY and 1.29 mJy respectively. Hence, the calculated SFR from radio

flux densities are 3575 $M_\odot$ yr^{-1} and 3720 $M_\odot$ yr^{-1}. However, the UV SFR for these regions are $\sim 2{\times}10^{-3}$ and $\sim 2{\times}10^{-3}$. So, the UV emission from star formation alone cannot explain the existing radio emission. This supports that a radio jet is present in source 2. The jets are interacting with the ISM and producing the star-formation which gives rise to the UV emission. Further higher resolution and deep radio observations are needed to confirm this core jet structure.

5.6.3 Why are the lobes shifted from the core?

Two sided radio structures (A, B) are shifted from the core (C). If the system is a core-jet structure, then it has a C- shape, i.e the jets may have bent C-shaped structure. Such C-shaped jet structures are seen in large-scale jets like narrow-angle tails (NAT) in NGC 1265 (Owen, Burns & Rudnick 1978). NATs are generally found in galaxy clusters and can be explained as due to the motion of the jets in the cluster medium. However, C-shapes are not very common in small scale jets and we could not find any detections that are comparable to the size of the C-shaped radio emission in MRK 212.

5.6.4 Merger induced star-formation

Models of star-formation predict an increase of the star formation rate both in the disks, nuclei and even in the outer tidal tails (Duc et al. 2000). We have calculated the SFR using the UVIT data on MRK 212. The SFR of visually selected regions varies from 3^{-5} to 2.7×10^{-3} $M_\odot$ yr^{-1} in NUV and 6^{-4} to 29.2×10^{-2} $M_\odot$ yr^{-1} in FUV. Such of SFRs are seen in isolated galaxies also (Vaddi et al. 2016). However, the radio and UV emission coincide in A, B regions, which supports the jet-induced star-formations scenario. This is possibly one of the few direct evidences that the

AGN in galaxies can affect the nuclear star-formation through feedback processes (Silk 2005; Gaibler et al. 2012).

5.7 Summary

1. We have compiled a sample of 17 nearby dual nuclei galaxies to observe with UVIT. So far, we have obtained data for 15 sources. Most of the sources have 2 to 5 ksec observing time.

2. MRK 212 (source 1) is part of a galaxy pair where the companion (source 2) is at a projected separation of $\sim$11.8″ or $\sim$ 6 kpc. Both sources are detected in the FIRST 1.4 GHz radio image. The SDSS spectrum of source 2 shows that the nuclear emission is due to star-formation.

3. Archival 4.86 and 8.46 GHz images have detected both the sources. In the 8.46 GHz image one of the cores is resolved into a two sided symmetric structure (A, B). This structure is at a distance of 1″ away from the optical centre.

4. The 15 GHz VLA image reveals an extended structure for source 1 and a compact radio structure (C) in source 2. This coincides with the optical centre of source 2.

5. Our uGMRT 1.4 GHz observations have a detected compact core in source 1 while an extended structure (A, C) in source 2. The spectral index map from uGMRT data shows flat spectral index for source 1 and steep spectral index for source 2.

6. The spectral index from C-, X-band and 1.4 GHz FIRST maps also supports the flat spectral index value for source 1 and steep spectral index value for source 2.

7. The HCT spectra of the individual cores are plotted in the BPT diagram, where source 1 falls in the star-forming region and source 2 falls in the AGN+SF region.

8. The X-ray Chandra image reveals a soft spectrum for source 1 and harder spectrum for source 2.

9. Deep UVIT observation is able to resolve the star-forming knots in source 2 and in the tidal tails of MRK 212. The star-forming knot in source 2 coincide with the X-band two sided radio structure (A, B).

10. The star formation rate is calculated for the UV knots. The Hα emission and the radio fluxes are also used to calculate the SFR of the individual cores.

11. The flat spectral index values and higher SFRs from radio observations supports the AGN classification for source 1. The resolved structure, steep spectral index, hard spectrum and higher SFR from radio fluxes support the AGN classification of source 2.

12. The two sided structure in the X-band image along with the UV detection can be explained by the jet-ISM interaction which produces star formation.

13. If source 2 has a shifted core-jet structure then it can be a C-shaped source with bent jets which are common in large jets in galaxy clusters. This can be due to the motion of the jets in the galactic medium. We do not see enhancement in SFR due to merger but AGN driven SF is detected from the jet-ISM interaction

(A, B regions).

Chapter 6

Conclusions and Future Work

In this thesis, we have studied dual nuclei galaxies using radio and UV observations. Dual nuclei are the product of galaxy mergers. Dual nuclei systems include AGN pairs (dual AGN), AGN+ star-forming (SF) pair or SF+SF pair with separations < 10 kpc. In the first part of this thesis, we did a VLA radio study of a sample of double-peaked emission line galaxies. In the second part of the thesis we have observed a sample of dual nuclei galaxies with the UVIT. One of the UVIT targets, MRK 212 showed interesting radio continuum emission and extended star formation associated with the nuclei. Hence, we explored it with multi-wavelength observations and deep UVIT observations. The summary and conclusions of this thesis are discussed here. We also discuss a few future projects which are an outcome of this thesis.

6.1 Summary

We started with a DPAGN sample of 3030 galaxies. DPAGN can be due to dual or binary AGN, jet kinematics or rotating disks. We plotted the 3030 DPAGN galaxies in a ΔV vs σ plot along with confirmed DAGN, and non-confirmed DAGN candidates which had been observed using high-resolution radio observation. We selected 20 galaxies which have $\Delta V > 400$ km/sec with a redshift limit of z<0.1 and have radio detections in the FIRST map. We observed these 20 galaxies with the VLA at multiple-frequencies.

One of the targets in our DPAGN sample, 2MASX J12032061+1319316, showed two distinct radio hot spots on either side of the optical nucleus in our 6 and 15 GHz VLA images. Meanwhile, the VLA archival data at 8.5 and 11.5 GHz revealed extended radio jets associated with the two hot spots. The radio jets have an S-shaped helical structure extending out to a radius of $\sim 1.5''$ (1.74 kpc) on either side of a deconvolved core of size $\sim 0.1''$ (116 parsec).

The S-shaped radio structure could be another indirect signature of dual/binary AGN. However, a warped accretion disk can also give rise to the S- shaped structure. To investigate the S-shaped jet structure a helical jet model from Hjellming & Johnston (1981) was fitted. The best-fit jet advance speed is 0.023c and the precession timescale is $\sim 10^5$ yrs. The half opening angle is $\psi = 21^\circ \pm 2^\circ$ and the inclination angle for the radio jets is $i = 52^\circ \pm 5^\circ$. The equipartition theorem was used to calculate the magnetic field and the electron life time. The calculated minimum magnetic field value is 105 μG and the electron lifetime is $\sim 10^5$ years. This timescale matches the time for which the precessing jet was "on" in this Seyfert galaxy, providing support to the precession model.

We have calculated the separation of the binary system which can give the precession period of 10^5 years using Begelman, Blandford & Rees (1980b). This gives a

separation of $\sim$ 0.02 pc. Therefore, there could be a second SMBH at a separation of 0.02 pc in 2MASXJ1203.

Lu (1990) suggested that a tilted accretion disk can also produce jet precession. This model of a tilted accretion disk around a single AGN gives a relation between the precession period and the luminosity. We have used the period-luminosity relation where the absolute B-band magnitude of our target* is M_{abs} = -20.34 and the calculated precession period is $\sim 10^5 - 10^9$ yrs.

The remaining 19 sources from the sample were observed at 8.5 and 11.5 GHz with the VLA. Of these sources, three have dual radio sources that represent dual nuclei. These are SDSSJ100602.13+071130.9, SDSSJ135558.08+001530.6 and 2MASXJ16170895+2226279 with projected separations of the nuclei as 12, 8.2 and 5.6 kpc, respectively. All three galaxies are merger systems. The spectral index map of the sources and the SDSS spectra of their nuclear optical emission confirmed that J100602.13+071130.9 is a dual AGN system. The calculated radio power showed that the primary object is a radio-weak AGN. The secondary has resolved two sided jets in 8.5 and 11.5 GHz images. The second source SDSSJ135558.08+001530.6 has two steep spectrum cores. The radio power is low. This can be a dual AGN or an AGN-starforming nuclei pair. The third source 2MASXJ16170895+2226279 has two cores where the primary core has a steep spectrum which is because of jet contribution detected at 15 GHz. The second core has a flat spectral index. This also can be an AGN or star-forming nucleus.

SDSSJ110215.68+290725.2 shows a two sided core-jet structure of size $\sim$6 kpc. However, the FIRST map shows a large scale jet of size 132 kpc. The overlay of the two maps revealed a Z-shape structure.

*http://leda.univ-lyon1.fr/

The source 2MASXJ14454130+3341080 has a bright core and is extended out on one side to a radius of 1.14 kpc. Both the core and the extended structures have steep spectral indices. We cannot rule out a possible dual AGN classification for this source with the present data.

The SMBH masses, Eddington ratios and the star formation rates were calculated using the optical spectra and the radio emission (1.4 GHz). We found that the [O III] luminosity (L[O III]) is strongly correlated with the SFR(Hα).

The SDSS fibre has a size of $3''$. As the detected dual AGN is at a separation of $> 3''$, the DPAGN in our sample do not originate from the dual AGN in these systems. Jet-ISM interaction, outflows or NLR rotating disk give rise to the DPAGN in these galaxies.

High resolution radio observations alone cannot help us to determine the origin of the DPAGN in our sample galaxies. We deduce that most of the DPAGN arise from NLR-jet kinematics as we have not detected dual AGN in these systems. However, we can not rule out the possibilities of a faint second AGN or a nearby AGN which is below our resolution and sensitivity limits.

We studied a sample of dual nuclei galaxies in FUV and NUV emission with the UVIT. The sample consists of dual AGN, AGN+SF and SF+SF nuclei. However, in a few galaxies, the nature of the nuclei are not confirmed. In these UV studies, our main motivation was to resolve the UV emission from individual nuclei, disk and tidal arms, calculate the SFRs and confirm the nature of the nuclei with multi-wavelength observation. We have made a sample of 17 galaxies which show dual nuclei at separation <10 kpc and have redshifts $z < 0.1$. In this sample 15 galaxies have been observed with the UVIT, with typical exposure times time of 2 to 5 ksec.

We have showed that the UVIT observation of MRK 739, which is a confirmed dual AGN has extended UV bright regions which do not follow the optical tidal arms. The optical spectra shows signatures of outflows and the molecular gas spectra has asymmetric structure. The data suggests that there is AGN feedback in the galaxy. There is star-formation surrounding the nuclei as traced by the UV emission and it could be due to AGN feedback. However, our UVIT exposure time is only 2.5 ksec for MRK 739 and is not deep enough to obtain a clear understanding of the origin of the extended star formation and resolve the star-forming knots.

For MRK 212, we have deep observations of exposure time $\sim$ 15 ksec. This is a merging galaxy system with nuclei separations of 11.8$''$ or $\sim$6 kpc. The nature of the nuclei are uncertain from existing radio and SDSS data. We have done a multi-wavelength study to confirm the nature of the nuclei. The primary source (source 1) did not have an optical spectrum and the secondary source (source 2) has an SDSS spectrum which shows that the nucleus is star-forming in nature. The FIRST image showed two resolved sources. We have obtained archival 4.86, 8.46 GHz images of MRK 212. We then observed MRK 212 at 15 GHz with VLA and at 1.4 GHz with the uGMRT. All the radio images suggest a flat spectral index value for source 1. The source 2 has a two sided extended radio structure of size 2 kpc which is offset from optical centre (1kpc) and a compact radio structure at the centre of these two structures which coincides with the optical centre. The two sided structure is also resolved in the UVIT image. Using UVIT we have also resolved several star forming knots in the inner spiral arms. We have calculated the SFRs using UV, Hα and radio emission of both the cores. The SFR from radio emission is much higher than that from UV or Hα emission for both the sources.

6.2 Conclusions:

Conclusions from the study on 2MASX J12032061+1319316 : There are three kinds of mechanisms that can explain the S-shaped radio structure in J1203: (i) If it is due to a binary AGN then the separation between the two SMBHs is. 0.02 pc which we cannot be resolved with any present day telescope. (ii) A single AGN with a warped accretion disk can also give rise to it. (iii) There can be a dual SMBH system and the secondary SMBH has passed the primary SMBH in the past; this could have induced the precession in the jet of the primary SMBH. However, the secondary SMBH may not have sufficient radio flux density to be detected in our observations. Future high resolution multi-wavelength (radio, X-ray, optical, NIR) observations are required to put the limits on the third possibility.

Conclusions from the radio study of 19 DPAGN: (i) SDSSJ100602.13+071130.9 is a dual AGN system but the double-peaks in the optical spectrum do not originate from dual AGN. (ii) The Z-structure in J1102 can be due to precession of the radio jets caused by a dual/binary AGN system or a tilted accretion disk associated with a single AGN like J1203. (iii) We find that DPAGN in low resolution optical spectra such as SDSS spectra, are not good indicators of dual/binary AGN. Instead, closely interacting galaxies and merger remnants are good candidates for detecting dual/binary AGN.

Conclusions from the study of MRK 212: From radio and UV observations of MRK 212 we have confirmed that the merger system MRK 212 is a dual AGN (nuclei separation of 6 kpc). The source 2 has a core-jet structure, and a core as well as two lobes are detected. We have detected direct evidence of jet-ISM induced star-formation using UV observations. The regions in the tidal arms do not show enhanced SFRs.

6.3 Future Work

In this section we briefly describe ongoing projects and future plans.

(i) We plan to do Chandra X-ray observations of J1203 to rule out one of the three origins for jet precession in this DPAGN galaxy. Thus, if there is a second AGN which is a few arcseconds away from the primary but radio quiet, we may be able to detect it with X-ray observations.

(ii) We have confirmed the presence of dual AGN in one of our DPAGN galaxies - J1006. However, the double-peaks in the optical spectrum do not originate from the dual radio cores as the separation is more than $3''$. We plan to do long slit optical observations to find out the origin of the DPAGN. This approach is similar to the study of Müller-Sánchez et al. (2015a) who have done simultaneous radio and long-slit spectroscopy to find out the origin of the DPAGN in their sample. We want to do this study for all of our sample galaxies.

(iii) We plan to explore J1006 with multi-wavelength observations in order to understand this merger system. This is similar to Shangguan et al. (2016), who have done Chandra and HST observations of four confirmed dual AGN to understand the effect of dual AGN on the galaxy.

(iv) A sensitive high resolution observation of J1102 can resolve the direction of the jets. We have found that there is already a GMRT observation of this source. We have plan to explore this in a collaborative work. A jet precession model will be fitted to the observations to calculate the expected separation of binary/dual AGN (if present).

(v) J1445 shows an extended structure though it is not resolved. This can be single AGN with core-jet structure or a dual AGN. We plan to obtain high-resolution

observation of J1445 from VLA to resolve the structure.

(vi) J1600 has a large scale 1 Mpc jet in NVSS map. The FIRST image shows the directional change in jet propagation. We want to observe this galaxy with uGMRT 1.4 GHz to explore whether it is double-double radio source or X-shaped radio galaxy.

(vii) Until now we have explored one of our UVIT sample galaxy MRK 212 with multi-wavelength data. We have confirmed the dual AGN as well as found the jet-ISM induced star-formation in the secondary source. We have UVIT data of 14 more galaxies. We need explore the data and if needed apply tor deeper observations.

(viii) We have observed a galaxy system which shows signature of large scale interaction in its GMRT image. We have observed this source with VLA to confirmed the host galaxies of the jet pair. This is a collaborative work.

Bibliography

Amblard A., Riguccini L., Temi P., Im S., Fanelli M., Serra P., 2014, *Astrophys. J.*, 783, 135

An T., Baan W. A., 2012, *Astrophys. J.*, 760, 77

An T., Mohan P., Frey S., 2018, Radio Science, 53, 1211

Antonucci R., 1993, *Ann. Rev. Astron. Astrophys.*, 31, 473

Baldwin J. A., Phillips M. M., Terlevich R., 1981a, *Pub. Astron. Soc. Pac.*, 93, 5

Baldwin J. A., Phillips M. M., Terlevich R., 1981b, *Pub. Astron. Soc. Pac.*, 93, 5

Barnes J. E., Hernquist L., 1992, *Ann. Rev. Astron. Astrophys.*, 30, 705

Barway S., Saha K., Vaghmare K., Kembhavi A. K., 2016, *Mon. Not. Roy. Astron. Soc.*, 463, L41

Becker R. H., White R. L., Edwards A. L., 1991, *Astrophys. J. Suppl.*, 75, 1

Becker R. H., White R. L., Helfand D. J., 1994, in Astronomical Society of the Pacific Conference Series, Vol. 61, Astronomical Data Analysis Software and Systems III, Crabtree D. R., Hanisch R. J., Barnes J., eds., p. 165

Begelman M. C., 1985, in Astrophysics of Active Galaxies and Quasi-Stellar Objects, Miller J. S., ed., pp. 411–452

Begelman M. C., Blandford R. D., Rees M. J., 1980a, *Nature*, 287, 307

Begelman M. C., Blandford R. D., Rees M. J., 1980b, *Nature*, 287, 307

Bell E. F., McIntosh D. H., Katz N., Weinberg M. D., 2003, *Astrophys. J. Suppl.*, 149, 289

Benson A. J., Bower R. G., Frenk C. S., Lacey C. G., Baugh C. M., Cole S., 2003, *Astrophys. J.*, 599, 38

Berczik P., Merritt D., Spurzem R., Bischof H.-P., 2006, *Astrophys. J. Lett.*, 642, L21

Bianchi S., Chiaberge M., Piconcelli E., Guainazzi M., Matt G., 2008, *Mon. Not. Roy. Astron. Soc.*, 386, 105

Binney J., Tremaine S., 2008, Galactic Dynamics: Second Edition. Princeton University Press

Blandford R. D., 1985, in Numerical Astrophysics, Centrella J. M., Leblanc J. M., Bowers R. L., eds., p. 6

Blandford R. D., Payne D. G., 1982, *Mon. Not. Roy. Astron. Soc.*, 199, 883

Blandford R. D., Znajek R. L., 1977, *Mon. Not. Roy. Astron. Soc.*, 179, 433

Blecha L., Loeb A., Narayan R., 2013, *Mon. Not. Roy. Astron. Soc.*, 429, 2594

Blundell K. M., Bowler M. G., 2004, *Astrophys. J. Lett.*, 616, L159

Boroson T. A., Lauer T. R., 2009, *Nature*, 458, 53

Bournaud F., 2010, in Astronomical Society of the Pacific Conference Series, Vol. 423, Galaxy Wars: Stellar Populations and Star Formation in Interacting Galaxies, Smith B., Higdon J., Higdon S., Bastian N., eds., p. 177

Burbidge G. R., 1959, *Astrophys. J.*, 129, 849

Burke-Spolaor S., Brazier A., Chatterjee S., Comerford J., Cordes J., Lazio T. J. W., Liu X., Shen Y., 2014, arXiv e-prints

Calzetti D. et al., 2007, *Astrophys. J.*, 666, 870

Capetti A., Zamfir S., Rossi P., Bodo G., Zanni C., Massaglia S., 2002, *Astron. Astrophys.*, 394, 39

Cappellari M., Emsellem E., 2004, *Pub. Astron. Soc. Pac.*, 116, 138

Carilli C. L., Perley R. A., Dreher J. W., Leahy J. P., 1991, *Astrophys. J.*, 383, 554

Cheung C. C., Springmann A., 2007, in Astronomical Society of the Pacific Conference Series, Vol. 373, The Central Engine of Active Galactic Nuclei, Ho L. C., Wang J.-W., eds., p. 259

Clemens M. S., Scaife A., Vega O., Bressan A., 2010, *Mon. Not. Roy. Astron. Soc.*, 405, 887

Collier J. D. et al., 2018, *Mon. Not. Roy. Astron. Soc.*, 477, 578

Colpi M., 2014, *Space Sci. Rev.*, 183, 189

Comerford J. M., Gerke B. F., Stern D., Cooper M. C., Weiner B. J., Newman J. A., Madsen K., Barrows R. S., 2012a, *Astrophys. J.*, 753, 42

Comerford J. M., Gerke B. F., Stern D., Cooper M. C., Weiner B. J., Newman J. A., Madsen K., Barrows R. S., 2012b, *Astrophys. J.*, 753, 42

Comerford J. M., Pooley D., Barrows R. S., Greene J. E., Zakamska N. L., Madejski G. M., Cooper M. C., 2015a, *Astrophys. J.*, 806, 219

Comerford J. M., Pooley D., Barrows R. S., Greene J. E., Zakamska N. L., Madejski G. M., Cooper M. C., 2015b, *Astrophys. J.*, 806, 219

Comerford J. M., Pooley D., Gerke B. F., Madejski G. M., 2011, *Astrophys. J. Lett.*, 737, L19

Condon J. J., 1992, *Ann. Rev. Astron. Astrophys.*, 30, 575

Condon J. J., Cotton W. D., Greisen E. W., Yin Q. F., Perley R. A., Taylor G. B., Broderick J. J., 1998, *Astron. J.*, 115, 1693

Conselice C. J., 2006, *Astrophys. J.*, 638, 686

Cox T. J., Loeb A., 2008, *Mon. Not. Roy. Astron. Soc.*, 386, 461

Crenshaw D. M., Kraemer S. B., 2000, *Astrophys. J. Lett.*, 532, L101

Crenshaw D. M., Schmitt H. R., Kraemer S. B., Mushotzky R. F., Dunn J. P., 2010, *Astrophys. J.*, 708, 419

Das M., Rubinur K., Kharb P., Varghese A., Navyasree K., James A., 2017, ArXiv e-prints

Das M., Vogel S. N., Verdoes Kleijn G. A., O'Dea C. P., Baum S. A., 2005, *Astrophys. J.*, 629, 757

Deane R. P. et al., 2014, *Nature*, 511, 57

Dennett-Thorpe J., Bridle A. H., Laing R. A., Scheuer P. A. G., 1999, *Mon. Not. Roy. Astron. Soc.*, 304, 271

Di Matteo T., Springel V., Hernquist L., 2005a, *Nature*, 433, 604

Di Matteo T., Springel V., Hernquist L., 2005b, *Nature*, 433, 604

Dotti M., Merloni A., Montuori C., 2015, *Mon. Not. Roy. Astron. Soc.*, 448, 3603

Douglas J. N., Bash F. N., Bozyan F. A., Torrence G. W., Wolfe C., 1996, *Astron. J.*, 111, 1945

Drake A. J. et al., 2009, *Astrophys. J.*, 696, 870

Duc P.-A., Brinks E., Springel V., Pichardo B., Weilbacher P., Mirabel I. F., 2000, *Astron. J.*, 120, 1238

Dugan Z., Bryan S., Gaibler V., Silk J., Haas M., 2014, *Astrophys. J.*, 796, 113

Ekers R. D., Fanti R., Lari C., Parma P., 1978, *Nature*, 276, 588

eLISA Consortium et al., 2013, ArXiv e-prints

Eracleous M., Halpern J. P., 2003, *Astrophys. J.*, 599, 886

Evans I. N. et al., 2010, *Astrophys. J. Suppl.*, 189, 37

Fabbiano G., Wang J., Elvis M., Risaliti G., 2011, *Nature*, 477, 431

Fanaroff B. L., Riley J. M., 1974, *Mon. Not. Roy. Astron. Soc.*, 167, 31P

Fanti C., Fanti R., Dallacasa D., Schilizzi R. T., Spencer R. E., Stanghellini C., 1995, *Astron. Astrophys.*, 302, 317

Fathi K., Allen M., Boch T., Hatziminaoglou E., Peletier R. F., 2010, *Mon. Not. Roy. Astron. Soc.*, 406, 1595

Fu H., Myers A. D., Djorgovski S. G., Yan L., Wrobel J. M., Stockton A., 2015a, *Astrophys. J.*, 799, 72

Fu H., Stockton A., 2009, *Astrophys. J.*, 696, 1693

Fu H., Wrobel J. M., Myers A. D., Djorgovski S. G., Yan L., 2015b, *Astrophys. J. Lett.*, 815, L6

Fu H., Yan L., Myers A. D., Stockton A., Djorgovski S. G., Aldering G., Rich J. A., 2012, *Astrophys. J.*, 745, 67

Fu H. et al., 2011a, *Astrophys. J. Lett.*, 740, L44

Fu H. et al., 2011b, *Astrophys. J. Lett.*, 740, L44

Gabányi K. É., An T., Frey S., Komossa S., Paragi Z., Hong X.-Y., Shen Z.-Q., 2016, *Astrophys. J.*, 826, 106

Gaibler V., Khochfar S., Krause M., Silk J., 2012, *Mon. Not. Roy. Astron. Soc.*, 425, 438

Gaskell C. M., 1983, in Liege International Astrophysical Colloquia, Vol. 24, Liege International Astrophysical Colloquia, Swings J.-P., ed., pp. 473–477

Ge J.-Q., Hu C., Wang J.-M., Bai J.-M., Zhang S., 2012, *Astrophys. J. Suppl.*, 201, 31

Gelderman R., Whittle M., 1994, *Astrophys. J. Suppl.*, 91, 491

Gergely L. Á., Biermann P. L., 2009, *Astrophys. J.*, 697, 1621

Gerhard O. E., 1993, *Mon. Not. Roy. Astron. Soc.*, 265, 213

Gillone M., Capetti A., Rossi P., 2016, *Astron. Astrophys.*, 587, A25

Gopal-Krishna, Biermann P. L., Wiita P. J., 2003, *Astrophys. J. Lett.*, 594, L103

Graham M. J. et al., 2015, *Nature*, 518, 74

Greene J. E., Ho L. C., 2005, *Astrophys. J.*, 627, 721

Greene J. E., Ho L. C., 2006, *Astrophys. J. Lett.*, 641, L21

Hardcastle M. J., Birkinshaw M., Worrall D. M., 2001, *Mon. Not. Roy. Astron. Soc.*, 326, 1499

Harris D. E., Krawczynski H., 2006, *Ann. Rev. Astron. Astrophys.*, 44, 463

Heckman T. M., Kauffmann G., Brinchmann J., Charlot S., Tremonti C., White S. D. M., 2004, *Astrophys. J.*, 613, 109

Heckman T. M., Miley G. K., van Breugel W. J. M., Butcher H. R., 1981, *Astrophys. J.*, 247, 403

Hernández-Ibarra F. J., Krongold Y., Dultzin D., del Olmo A., Perea J., González J., Mendoza-Castrejón S., Bitsakis T., 2016, *Mon. Not. Roy. Astron. Soc.*, 459, 291

Hjellming R. M., Johnston K. J., 1981, *Astrophys. J. Lett.*, 246, L141

Ho L. C., 2008, *Ann. Rev. Astron. Astrophys.*, 46, 475

Hodges-Kluck E. J., Reynolds C. S., 2012, *Astrophys. J.*, 746, 167

Hodges-Kluck E. J., Reynolds C. S., Miller M. C., Cheung C. C., 2010, *Astrophys. J. Lett.*, 717, L37

Högbom J. A., 1974, *Astron. Astrophys. Suppl.*, 15, 417

Holley-Bockelmann K., Khan F. M., 2015, *Astrophys. J.*, 810, 139

Hopkins A. M. et al., 2003, *Astrophys. J.*, 599, 971

Hopkins P. F., Cox T. J., Kereš D., Hernquist L., 2008, *Astrophys. J. Suppl.*, 175, 390

Hota A., Lim J., Ohyama Y., Saikia D. J., Dihn-v-Trung, Croston J. H., 2009, in Astronomical Society of the Pacific Conference Series, Vol. 407, The Low-Frequency Radio Universe, Saikia D. J., Green D. A., Gupta Y., Venturi T., eds., p. 104

Hudson D. S., Reiprich T. H., Clarke T. E., Sarazin C. L., 2006, *Astron. Astrophys.*, 453, 433

Hutchings J. B., Price R., Gower A. C., 1988, *Astrophys. J.*, 329, 122

Ishibashi W., Fabian A. C., 2012, *Mon. Not. Roy. Astron. Soc.*, 427, 2998

Jennison R. C., Das Gupta M. K., 1953, *Nature*, 172, 996

Junkkarinen V., Shields G. A., Beaver E. A., Burbidge E. M., Cohen R. D., Hamann F., Lyons R. W., 2001, *Astrophys. J. Lett.*, 549, L155

Karl S. J., Naab T., Johansson P. H., Kotarba H., Boily C. M., Renaud F., Theis C., 2010, *Astrophys. J. Lett.*, 715, L88

Kaviraj S., Peirani S., Khochfar S., Silk J., Kay S., 2009, *Mon. Not. Roy. Astron. Soc.*, 394, 1713

Kellermann K. I., Sramek R., Schmidt M., Shaffer D. B., Green R., 1989, *Astron. J.*, 98, 1195

Kennicutt, Jr. R. C., 1998a, *Ann. Rev. Astron. Astrophys.*, 36, 189

Kennicutt, Jr. R. C., 1998b, *Astrophys. J.*, 498, 541

Kewley L. J., Groves B., Kauffmann G., Heckman T., 2006, *Mon. Not. Roy. Astron. Soc.*, 372, 961

Khan F. M., Just A., Merritt D., 2011, *Astrophys. J.*, 732, 89

Kharb P., Das M., Paragi Z., Subramanian S., Chitta L. P., 2015a, *Astrophys. J.*, 799, 161

Kharb P., Das M., Paragi Z., Subramanian S., Chitta L. P., 2015b, *Astrophys. J.*, 799, 161

Kharb P., Lal D. V., Merritt D., 2017, Nature Astronomy, 1, 727

Kharb P., O'Dea C. P., Baum S. A., Colbert E. J. M., Xu C., 2006, *Astrophys. J.*, 652, 177

Kharb P., O'Dea C. P., Baum S. A., Daly R. A., Mory M. P., Donahue M., Guerra E. J., 2008, *Astrophys. J. Suppl.*, 174, 74

Kharb P., Srivastava S., Singh V., Gallimore J. F., Ishwara-Chandra C. H., Hota A., 2016, ArXiv e-prints

Kharb P., Subramanian S., Vaddi S., Das M., Paragi Z., 2017, *Astrophys. J.*, 846, 12

Kharb P., Vaddi S., Sebastian B., Subramanian S., Das M., Paragi Z., 2019, *Astrophys. J.*

King A., 2005, *Astrophys. J. Lett.*, 635, L121

Kocevski D. D. et al., 2015, *Astrophys. J.*, 814, 104

Komossa S., 2006, *Memorie della Societ Astronomica Italiana*, 77, 733

Komossa S., Baker J. G., Liu F. K., 2016, IAU Focus Meeting, 29, 292

Komossa S., Burwitz V., Hasinger G., Predehl P., Kaastra J. S., Ikebe Y., 2003a, *Astrophys. J. Lett.*, 582, L15

Komossa S., Burwitz V., Hasinger G., Predehl P., Kaastra J. S., Ikebe Y., 2003b, *Astrophys. J. Lett.*, 582, L15

Koss M. et al., 2011, *Astrophys. J. Lett.*, 735, L42

Koss M., Mushotzky R., Treister E., Veilleux S., Vasudevan R., Trippe M., 2012a, *Astrophys. J. Lett.*, 746, L22

Koss M., Mushotzky R., Treister E., Veilleux S., Vasudevan R., Trippe M., 2012b, *Astrophys. J. Lett.*, 746, L22

Koss M. J. et al., 2016, *Astrophys. J. Lett.*, 824, L4

Kraft R. P., Forman W. R., Jones C., Murray S. S., Hardcastle M. J., Worrall D. M., 2002, *Astrophys. J.*, 569, 54

Kulier A., Ostriker J. P., Natarajan P., Lackner C. N., Cen R., 2015, *Astrophys. J.*, 799, 178

Kumar A. et al., 2012, in *Proc. SPIE*, Vol. 8443, Space Telescopes and Instrumentation 2012: Ultraviolet to Gamma Ray, p. 84431N

Laing R. A., Peacock J. A., 1980, *Mon. Not. Roy. Astron. Soc.*, 190, 903

Leahy J. P., Williams A. G., 1984a, *Mon. Not. Roy. Astron. Soc.*, 210, 929

Leahy J. P., Williams A. G., 1984b, *Mon. Not. Roy. Astron. Soc.*, 210, 929

Lehto H. J., Valtonen M. J., 1996, *Astrophys. J.*, 460, 207

Lin L. et al., 2008, *Astrophys. J.*, 681, 232

Liu T. et al., 2015, *Astrophys. J. Lett.*, 803, L16

Liu X., Civano F., Shen Y., Green P., Greene J. E., Strauss M. A., 2013a, *Astrophys. J.*, 762, 110

Liu X., Civano F., Shen Y., Green P., Greene J. E., Strauss M. A., 2013b, *Astrophys. J.*, 762, 110

Liu X., Greene J. E., Shen Y., Strauss M. A., 2010, *Astrophys. J. Lett.*, 715, L30

Liu X., Lazio T. J. W., Shen Y., Strauss M. A., 2017, ArXiv e-prints

Liu X., Lazio T. J. W., Shen Y., Strauss M. A., 2018, *Astrophys. J.*, 854, 169

Livio M., Pringle J. E., 1997, *Astrophys. J.*, 486, 835

Lotz J. M., Jonsson P., Cox T. J., Primack J. R., 2008, *Mon. Not. Roy. Astron. Soc.*, 391, 1137

Lu J. F., 1990, *Astron. Astrophys.*, 229, 424

Maiolino R. et al., 2017, *Nature*, 544, 202

Makarov D., Prugniel P., Terekhova N., Courtois H., Vauglin I., 2014, *Astron. Astrophys.*, 570, A13

Manchester R. N. et al., 2013, *Publications of the Astronomical Society of Australia*, 30, e017

Mao M. Y., Sharp R., Saikia D. J., Norris R. P., Johnston-Hollitt M., Middelberg E., Lovell J. E. J., 2010, *Mon. Not. Roy. Astron. Soc.*, 406, 2578

Mayer L., Kazantzidis S., Madau P., Colpi M., Quinn T., Wadsley J., 2007, Science, 316, 1874

McConnell N. J., Ma C.-P., 2013, *Astrophys. J.*, 764, 184

McGurk R. C., Max C. E., Medling A. M., Shields G. A., Comerford J. M., 2015, *Astrophys. J.*, 811, 14

McGurk R. C., Max C. E., Rosario D. J., Shields G. A., Smith K. L., Wright S. A., 2011, *Astrophys. J. Lett.*, 738, L2

McMullin J. P., Waters B., Schiebel D., Young W., Golap K., 2007, in Astronomical Society of the Pacific Conference Series, Vol. 376, Astronomical Data Analysis Software and Systems XVI, Shaw R. A., Hill F., Bell D. J., eds., p. 127

Menou K., Haiman Z., Narayanan V. K., 2001, *Astrophys. J.*, 558, 535

Merritt D., 2013, Dynamics and Evolution of Galactic Nuclei

Merritt D., Ekers R. D., 2002, Science, 297, 1310

Merritt D., Milosavljević M., 2005a, Living Reviews in Relativity, 8

Merritt D., Milosavljević M., 2005b, Living Reviews in Relativity, 8

Mezcua M., Lobanov A. P., Chavushyan V. H., León-Tavares J., 2011, *Astron. Astrophys.*, 527, A38

Mezcua M., Lobanov A. P., Mediavilla E., Karouzos M., 2014, *Astrophys. J.*, 784, 16

Mihos J. C., Hernquist L., 1994, *Astrophys. J. Lett.*, 431, L9

Milosavljević M., Merritt D., 2001, *Astrophys. J.*, 563, 34

Müller-Sánchez F., Comerford J. M., Nevin R., Barrows R. S., Cooper M. C., Greene J. E., 2015a, *Astrophys. J.*, 813, 103

Müller-Sánchez F., Comerford J. M., Nevin R., Barrows R. S., Cooper M. C., Greene J. E., 2015b, *Astrophys. J.*, 813, 103

Müller-Sánchez F., Prieto M. A., Hicks E. K. S., Vives-Arias H., Davies R. I., Malkan M., Tacconi L. J., Genzel R., 2011, *Astrophys. J.*, 739, 69

Murgia M., 2003, *Publications of the Astronomical Society of Australia*, 20, 19

Murgia M., Parma P., de Ruiter H. R., Bondi M., Ekers R. D., Fanti R., Fomalont E. B., 2001, *Astron. Astrophys.*, 380, 102

Murthy J., Rahna P. T., Safonova M., Sutaria F., Gudennavar S. B., Bubbly S. G., 2016, JUDE: An Utraviolet Imaging Telescope pipeline. Astrophysics Source Code Library

Murthy J., Rahna P. T., Sutaria F., Safonova M., Gudennavar S. B., Bubbly S. G., 2017, Astronomy and Computing, 20, 120

Myers S. T., Spangler S. R., 1985, *Astrophys. J.*, 291, 52

Nagar N. M., Wilson A. S., Falcke H., Veilleux S., Maiolino R., 2003, *Astron. Astrophys.*, 409, 115

Nagar N. M., Wilson A. S., Mulchaey J. S., Gallimore J. F., 1999, *Astrophys. J. Suppl.*, 120, 209

Natarajan P., Pringle J. E., 1998a, *Astrophys. J. Lett.*, 506, L97

Natarajan P., Pringle J. E., 1998b, *Astrophys. J. Lett.*, 506, L97

Negroponte J., White S. D. M., 1983, *Mon. Not. Roy. Astron. Soc.*, 205, 1009

Netzer H., 2006, in Lecture Notes in Physics, Berlin Springer Verlag, Vol. 693, Physics of Active Galactic Nuclei at all Scales, Alloin D., ed., p. 1

Noel-Storr J., Baum S. A., Verdoes Kleijn G., van der Marel R. P., O'Dea C. P., de Zeeuw P. T., Carollo C. M., 2003, *Astrophys. J. Suppl.*, 148, 419

O'Dea C. P., 1998, *Pub. Astron. Soc. Pac.*, 110, 493

O'Dea C. P., Owen F. N., 1987, *Astrophys. J.*, 316, 95

Oke J. B., 1990, *Astron. J.*, 99, 1621

Owen F. N., Burns J. O., Rudnick L., 1978, *Astrophys. J. Lett.*, 226, L119

Owen F. N., O'Dea C. P., Inoue M., Eilek J. A., 1985, *Astrophys. J. Lett.*, 294, L85

Pacholczyk A. G., 1970, Radio astrophysics. Nonthermal processes in galactic and extragalactic sources

Parma P., Ekers R. D., Fanti R., 1985, *Astron. Astrophys. Suppl.*, 59, 511

Peck A. B., Taylor G. B., 2001, *Astrophys. J. Lett.*, 554, L147

Peng C. Y., Ho L. C., Impey C. D., Rix H.-W., 2002, *Astron. J.*, 124, 266

Peng C. Y., Ho L. C., Impey C. D., Rix H.-W., 2010, *Astron. J.*, 139, 2097

Perley R. A., Chandler C. J., Butler B. J., Wrobel J. M., 2011, *Astrophys. J. Lett.*, 739, L1

Peterson B. M., 1997, An Introduction to Active Galactic Nuclei

Pier E. A., Krolik J. H., 1993, *Astrophys. J.*, 418, 673

Pringle J. E., 1996, *Mon. Not. Roy. Astron. Soc.*, 281, 357

Pringle J. E., 1997, *Mon. Not. Roy. Astron. Soc.*, 292, 136

Rahna P. T., Das M., Murthy J., Gudennavar S. B., Bubbly S. G., 2018, *Mon. Not. Roy. Astron. Soc.*, 481, 1212

Readhead A. C. S., Taylor G. B., Xu W., Pearson T. J., Wilkinson P. N., Polatidis A. G., 1996, *Astrophys. J.*, 460, 612

Rees M. J., 1978, *Nature*, 275, 516

Rees M. J., 1984, *Ann. Rev. Astron. Astrophys.*, 22, 471

Ricci C. et al., 2017, *Mon. Not. Roy. Astron. Soc.*, 468, 1273

Roberts D. H., Saripalli L., Wang K. X., Sathyanarayana Rao M., Subrahmanyan R., KleinStern C. C., Morii-Sciolla C. Y., Simpson L., 2018, *Astrophys. J.*, 852, 47

Robson I., 1996, Active galactic nuclei

Rodriguez C., Taylor G. B., Zavala R. T., Peck A. B., Pollack L. K., Romani R. W., 2006a, *Astrophys. J.*, 646, 49

Rodriguez C., Taylor G. B., Zavala R. T., Peck A. B., Pollack L. K., Romani R. W., 2006b, *Astrophys. J.*, 646, 49

Romero G. E., Chajet L., Abraham Z., Fan J. H., 2000, *Astron. Astrophys.*, 360, 57

Roos N., Kaastra J. S., Hummel C. A., 1993, *Astrophys. J.*, 409, 130

Rosario D. J., Shields G. A., Taylor G. B., Salviander S., Smith K. L., 2010, *Astrophys. J.*, 716, 131

Rottmann H., 2001, PhD thesis, Thesis (Ph.D.) – University Bonn, 2001, 180 pages

Roškar R., Fiacconi D., Mayer L., Kazantzidis S., Quinn T. R., Wadsley J., 2015, *Mon. Not. Roy. Astron. Soc.*, 449, 494

Rubinur K., Das M., Kharb P., 2018, Journal of Astrophysics and Astronomy, 39, 8

Rubinur K., Das M., Kharb P., 2019, *Mon. Not. Roy. Astron. Soc.*, 484, 4933

Rubinur K., Das M., Kharb P., Honey M., 2017, *Mon. Not. Roy. Astron. Soc.*, 465, 4772

Salpeter E. E., 1955, *Astrophys. J.*, 121, 161

Sanders D. B., Soifer B. T., Elias J. H., Neugebauer G., Matthews K., 1988, *Astrophys. J. Lett.*, 328, L35

Sarazin C. L., Begelman M. C., Hatchett S. P., 1980, *Astrophys. J. Lett.*, 238, L129

Sargent A., Scoville N., 1991, *Astrophys. J. Lett.*, 366, L1

Sargent W. L. W., 1972a, *Astrophys. J.*, 173, 7

Sargent W. L. W., 1972b, *Astrophys. J.*, 173, 7

Satyapal S., Ellison S. L., McAlpine W., Hickox R. C., Patton D. R., Mendel J. T., 2014, *Mon. Not. Roy. Astron. Soc.*, 441, 1297

Satyapal S. et al., 2017, *Astrophys. J.*, 848, 126

Schmidt M., Green R. F., 1983, *Astrophys. J.*, 269, 352

Sebastian B., Lal D. V., Pramesh Rao A., 2017, *Astron. J.*, 154, 169

Shakura N. I., Sunyaev R. A., 1976, *Mon. Not. Roy. Astron. Soc.*, 175, 613

Shangguan J., Liu X., Ho L. C., Shen Y., Peng C. Y., Greene J. E., Strauss M. A., 2016, *Astrophys. J.*, 823, 50

Shen Y., Liu X., Greene J. E., Strauss M. A., 2011, *Astrophys. J.*, 735, 48

Silk J., 2005, *Mon. Not. Roy. Astron. Soc.*, 364, 1337

Silk J., 2013, *Astrophys. J.*, 772, 112

Sillanpaa A., Haarala S., Valtonen M. J., Sundelius B., Byrd G. G., 1988, *Astrophys. J.*, 325, 628

Singh V., Ishwara-Chandra C. H., Wadadekar Y., Beelen A., Kharb P., 2015, *Mon. Not. Roy. Astron. Soc.*, 446, 599

Smith K. L., Shields G. A., Bonning E. W., McMullen C. C., Rosario D. J., Salviander S., 2010, *Astrophys. J.*, 716, 866

Springel V., 2005, *Mon. Not. Roy. Astron. Soc.*, 364, 1105

Steenbrugge K. C., Blundell K. M., 2008, *Mon. Not. Roy. Astron. Soc.*, 388, 1457

Stockton A., Canalizo G., Fu H., Keel W., 2007, *Astrophys. J.*, 659, 195

Swarup G., Ananthakrishnan S., Kapahi V. K., Rao A. P., Subrahmanya C. R., Kulkarni V. K., 1991, Current Science, Vol. 60, NO.2/JAN25, P. 95, 1991, 60, 95

Terni de Gregory B., Feretti L., Giovannini G., Govoni F., Murgia M., Perley R. A., Vacca V., 2017, *Astron. Astrophys.*, 608, A58

Thompson A. R., Clark B. G., Wade C. M., Napier P. J., 1980, *Astrophys. J. Suppl.*, 44, 151

Tingay S. J., Wayth R. B., 2011a, *Astron. J.*, 141, 174

Tingay S. J., Wayth R. B., 2011b, *Astron. J.*, 141, 174

Toomre A., 1977, in Evolution of Galaxies and Stellar Populations, Tinsley B. M., Larson D. Campbell R. B. G., eds., p. 401

Toomre A., Toomre J., 1972, *Astrophys. J.*, 178, 623

Ulvestad J. S., 2003, in Astronomical Society of the Pacific Conference Series, Vol. 300, Radio Astronomy at the Fringe, Zensus J. A., Cohen M. H., Ros E., eds., p. 97

Urry C. M., Padovani P., 1995, *Pub. Astron. Soc. Pac.*, 107, 803

Vaddi S., O'Dea C. P., Baum S. A., Whitmore S., Ahmed R., Pierce K., Leary S., 2016, *Astrophys. J.*, 818, 182

Valtaoja E., Teräsranta H., Tornikoski M., Sillanpää A., Aller M. F., Aller H. D., Hughes P. A., 2000, *Astrophys. J.*, 531, 744

Valtonen M. J., Ciprini S., Lehto H. J., 2012, *Mon. Not. Roy. Astron. Soc.*, 427, 77

Valtonen M. J. et al., 2016, *Astrophys. J. Lett.*, 819, L37

van der Laan H., Perola G. C., 1969, *Astron. Astrophys.*, 3, 468

Van Wassenhove S., Volonteri M., Mayer L., Dotti M., Bellovary J., Callegari S., 2012, *Astrophys. J. Lett.*, 748, L7

Veilleux S., 1991, *Astrophys. J. Suppl.*, 75, 357

Villata M., Raiteri C. M., 1999, *Astron. Astrophys.*, 347, 30

Wang J.-M., Chen Y.-M., Hu C., Mao W.-M., Zhang S., Bian W.-H., 2009, *Astrophys. J. Lett.*, 705, L76

Wegg C., Gerhard O., Portail M., 2015, *Mon. Not. Roy. Astron. Soc.*, 450, 4050

White R. L., Becker R. H., 1992, *Astrophys. J. Suppl.*, 79, 331

Wilkinson P. N., Polatidis A. G., Readhead A. C. S., Xu W., Pearson T. J., 1994, *Astrophys. J. Lett.*, 432, L87

Wirth A., Smarr L., Gallagher J. S., 1982, *Astron. J.*, 87, 602

Worrall D. M., Birkinshaw M., Hardcastle M. J., 2003, *Mon. Not. Roy. Astron. Soc.*, 343, L73

Xu D., Komossa S., 2009, *Astrophys. J. Lett.*, 705, L20

Yu Q., 2002, *Mon. Not. Roy. Astron. Soc.*, 331, 935

Yun M. S., Reddy N. A., Condon J. J., 2001, *Astrophys. J.*, 554, 803

Zhou H., Wang T., Zhang X., Dong X., Li C., 2004, *Astrophys. J. Lett.*, 604, L33

Zier C., Biermann P. L., 2002, *Astron. Astrophys.*, 396, 91

Zwicky F., 1956, Ergebnisse der exakten Naturwissenschaften, 29, 344